

for such a detector, a shortage of ^3He is noticeable. The operating principle in general is that the incoming neutrons are converted through one of the reactions above into charged particles like a proton. Then those can ionise the gas of the proportional detector. With a high voltage between the anode and cathode the electrons, which were freed by the incoming charged particles, can then ionise further gas atoms. This way a significant amplification can be achieved [11].

2.2 Small-angle scattering

The small-angle scattering technique was originally introduced for X-rays. Since the discovery of neutrons their role as a probe particle became increasingly important and therefore small-angle scattering devices with neutrons are rather popular [12].

Small-angle scattering in general means that a probe with wave vector \vec{k} is scattered at a sample under a small angle θ , the scattering angle. This is equivalent to a small scattering vector \vec{Q} , which in turn means that the outgoing beam \vec{k}' goes almost in the same direction as the incoming \vec{k} [13]. This is illustrated in figure 2.

The theory of small-angle-neutron scattering is basically the same as for X-ray. The relation of the already mentioned scattering vector and the in/outgoing beam can be written as

$$\vec{Q} = \vec{k}' - \vec{k}. \quad (4)$$

Squaring equation (4) leads to

$$|\vec{Q}|^2 = |\vec{k}' - \vec{k}|^2 = \vec{k}^2 - 2\vec{k}\vec{k}' + \vec{k}'^2. \quad (5)$$

Since it can be assumed that the neutrons scatter elastically with the atoms of the sample ($|\vec{k}'| = |\vec{k}|$) equation (5) can be simplified:

$$|\vec{Q}|^2 = 2k^2(1 - \cos(\theta)) = 4k^2 \sin^2\left(\frac{\theta}{2}\right) \quad (6)$$

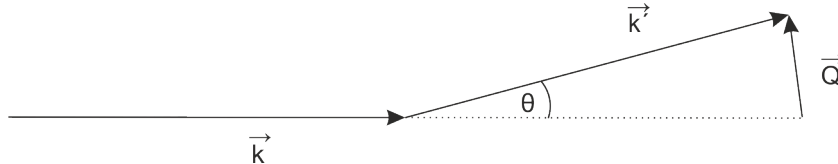


Figure 2: Schematic of small-angle scattering.

For (ultra) small-angle neutron scattering it can be assumed $\theta \ll 1$ which is perfectly applicable in the USANS case for all scattering angles. This leads to

$$Q \approx k\theta \quad (7)$$

For thermal neutrons $k \approx 1\text{\AA}^{-1}$ and therefore $Q \ll 1\text{\AA}^{-1}$. The resolution is given as the reciprocal of Q and therefore $A \gg 1\text{\AA}$ [14]. Ultra-small-angle neutron scattering is used for examining dislocations, grain boundary and other defects in solids. Furthermore macromolecules are also often probed with neutrons. The reason why neutrons are often favoured as probes is that they interact in two ways with the samples. On the one hand via scattering with the nuclei and on the other hand via magnetic scattering with the unpaired shell electrons [15].

For (ultra) small-angle X-ray scattering two different theoretical descriptions were dominating in the early 20th century: the theory from Rayleigh-Gans and the theory from Nardroff. The first one describes only diffraction while the last one is focused solely on refraction. Several papers which were based on experimental results disproved one or the other theory. It was not before 1946 as Van de Hulst showed that both of those theories were different limits of the same problem. The difference is in the phase change ρ of the neutron wave. If $\rho \ll 1$, the theory of diffraction is correct, and for $\rho \gg 1$, the theory of refraction is valid. The reason for the contradicting experiment results lie in the different choice of the sample size [16].

2.2.1 Diffraction

If ρ of the neutron wave is small, the partial waves can interfere. Therefore the widening of the neutron beam can be explained via diffraction.

The incident particles can be described as a plane wave moving towards to the sample. They are diffracted by the potential of the sample and now described by a spherical wave. The part of the incoming plane wave which is not getting scattered remains a plane wave. For further mathematical consideration the definition of the scattering amplitude $f(\vec{k}, \vec{k}') = f(\theta, \phi)$ is necessary. It describes the anisotropy of the outgoing spherical wave relative to the incoming plane wave [12], [15].

The differential cross section $\sigma(\theta, \phi)$ is the key quantity for describing scattering phenomena. It indicates the number dn of the scattered particles per unit

time in the differential solid angle $d\Omega$ normalised by the incoming particle flow j_i . $\sigma(\theta, \phi)$ has the dimension of an area and is given in barns $b = 10^{-28} \text{ m}^2$.

$$dn = j_i \sigma(\theta, \phi) d\Omega \quad (8)$$

The total cross section is then given as the integral of $\sigma(\theta, \phi)$ over the solid angle:

$$\sigma_{tot} = \int \sigma(\theta, \phi) d\Omega \quad (9)$$

In the following it will be assumed that at distances r far away from the target the incoming wave is free of interaction and can be described as superposition of plane waves. This means the incoming wave is in form of $e^{i\vec{k}\vec{r}}$. Although the wave function gets quite complicated near the scattering potential, for distances far away from the potential it can be described as a spherical wave with the same energy as the incoming wave [15].

$$\Psi(\vec{r}) \xrightarrow{r \rightarrow \infty} A \left[e^{i\vec{k}\vec{r}} + f(\theta, \phi) \frac{e^{ikr}}{r} \right] \quad (10)$$

The first part of equation (10) considers that part of the incoming wave might not be scattered and therefore remains a plane wave. The cross section can be calculated with the incoming particle current which in general is given as:

$$\vec{j}(\vec{r}) = \frac{1}{m} \text{Re} \left[\Psi^*(\vec{r}) \frac{\hbar}{i} \vec{\nabla} \Psi(\vec{r}) \right] \quad (11)$$

For the incoming plane wave this simplifies to

$$|j_i(\vec{r})| = |A|^2 \frac{\hbar k}{m}. \quad (12)$$

For the scattered wave it is a bit more complicated. Using the gradient in spherical coordinates

$$(\vec{\nabla})_r = \frac{\partial}{\partial r} \quad (13a)$$

$$(\vec{\nabla})_\theta = \frac{1}{r} \frac{\partial}{\partial \theta} \quad (13b)$$

$$(\vec{\nabla})_\phi = \frac{1}{r \sin(\theta)} \frac{\partial}{\partial \phi} \quad (13c)$$

the current can be calculated:

$$(\vec{j}_s)_r = |A|^2 \frac{\hbar k}{m} \frac{1}{r^2} |f(\theta, \phi)|^2 \quad (14a)$$

$$(\vec{j}_s)_\theta = |A|^2 \frac{\hbar}{m} \frac{1}{r^3} \text{Re} \left[\frac{1}{i} f^*(\theta, \phi) \frac{\partial}{\partial \theta} f(\theta, \phi) \right] \quad (14b)$$

$$(\vec{j}_s)_\phi = |A|^2 \frac{\hbar}{m} \frac{1}{r^3 \sin(\theta)} \text{Re} \left[\frac{1}{i} f^*(\theta, \phi) \frac{\partial}{\partial \phi} f(\theta, \phi) \right] \quad (14c)$$

Now it can be seen that for large r the radial term is dominant and the other two can be neglected. With this the number of scattered particles dn in the differential solid angle $d\Omega$ can be given:

$$dn = (j_s)_r r^2 d\Omega. \quad (15)$$

The differential cross section can be calculated by plugging (12) in (8) and equalizing the resulting equation with (15):

$$\sigma(\theta, \phi) = |f(\theta, \phi)|^2 \quad (16)$$

It is important to note that equation (16) is only valid outside of the initial direction of propagation. The reason for this is that only part of the incoming wave is being scattered. Therefore in the initial direction of propagation an interference takes place which complicates matters [15].

2.2.2 Born series

For calculating stationary scattering states the time-independent Schrödinger equation is used:

$$\left[-\frac{\hbar^2}{2m} \Delta + V(\vec{r}) \right] \Psi(\vec{r}) = E \Psi(\vec{r}) \quad (17)$$

One method of solving this differential equation is by using Green's function $G(\vec{r})$ of the operator $(\Delta + k^2)$

$$[\Delta + k^2] G(\vec{r} - \vec{r}') = \delta^{(3)}(\vec{r} - \vec{r}'). \quad (18)$$

For this, equation (17) must be rewritten

$$[\Delta + k^2] \Psi(\vec{r}) = U(\vec{r}) \Psi(\vec{r}) \quad (19)$$

with $k^2 = \frac{2mE}{\hbar^2}$ and $U(\vec{r}) = \frac{2m}{\hbar^2} V(\vec{r})$.

The wave function $\Psi(\vec{r})$ can now be determined

$$\Psi(\vec{r}) = \Psi_0(\vec{r}) + \int G(\vec{r} - \vec{r}') U(\vec{r}') \Psi(\vec{r}') d^3 r' \quad (20)$$

where $\Psi_0(\vec{r})$ is the solution of the homogeneous differential equation $[\Delta + k^2] \Psi(\vec{r}) = 0$

$$\Psi_0(\vec{r}) = e^{i\vec{k}\vec{r}}. \quad (21)$$

Equation (20) is the Lippmann–Schwinger equation in form of an integral [17]. Considering the solution of equation (18)

$$G_{\pm}(\vec{r} - \vec{r}') = -\frac{1}{4\pi} \frac{e^{\pm ik|\vec{r} - \vec{r}'|}}{|\vec{r} - \vec{r}'|} \quad (22)$$

and (21), one can write (20) as

$$\Psi(\vec{r}) = e^{i\vec{k}\vec{r}} - \frac{1}{4\pi} \int \frac{e^{ik|\vec{r} - \vec{r}'|}}{|\vec{r} - \vec{r}'|} U(\vec{r}') \Psi(\vec{r}') d^3 r' \quad (23)$$

where $G_+(\vec{r} - \vec{r}')$ was used. For further approximation it is necessary to look at the Taylor expansion of $|\vec{r} - \vec{r}'|$. For distances far away from the potential this can be written as

$$|\vec{r} - \vec{r}'| = \sqrt{r^2 - 2\vec{r}\vec{r}' - r'^2} \approx |\vec{r}| - \frac{\vec{r}\vec{r}'}{r} + O\left(\frac{1}{r}\right). \quad (24)$$

This can be used to simplify (23)

$$\Psi(\vec{r}) = e^{i\vec{k}\vec{r}} - \frac{1}{4\pi} \frac{e^{ikr}}{r} \int e^{-i\vec{k}'\vec{r}'} U(\vec{r}') \Psi(\vec{r}') d^3 r'. \quad (25)$$

with $\vec{k}' = k \frac{\vec{r}}{r}$.

Comparing (25) to (10) the scattering amplitude can be determined

$$f(\theta, \phi) = -\frac{1}{4\pi} \int e^{-i\vec{k}'\vec{r}'} U(\vec{r}') \Psi(\vec{r}') d^3 r'. \quad (26)$$

Going back to (20) one sees that this is an iterative equation which can be solved by substituting $\vec{r} \rightarrow \vec{r}'$ and $\vec{r}' \rightarrow \vec{r}''$. Plugging it back in equation (20) yields

$$\begin{aligned} \Psi(\vec{r}) &= e^{i\vec{k}\vec{r}} + \int G(\vec{r} - \vec{r}') U(\vec{r}') e^{i\vec{k}\vec{r}'} d^3 r' + \\ &+ \int \int G(\vec{r} - \vec{r}') U(\vec{r}') G(\vec{r}' - \vec{r}'') U(\vec{r}'') \Psi(\vec{r}'') d^3 r' d^3 r''. \end{aligned} \quad (27)$$

This can be repeated infinitely and this series is known as Born series [18]. Within the first Born approximation the last term of (27) can be neglected which means that only single scattering is considered

$$\Psi(\vec{r}) = e^{i\vec{k}\vec{r}} + \int G(\vec{r} - \vec{r}')U(\vec{r}')e^{i\vec{k}\vec{r}'}d^3r'. \quad (28)$$

Now the expression of the scattering amplitude (26) can be solved

$$\begin{aligned} f(\theta, \phi) &= -\frac{1}{4\pi} \int e^{-i(\vec{k}' - \vec{k})\vec{r}'} U(\vec{r}') d^3r' \\ &= -\frac{m}{2\pi\hbar^2} \int e^{-i\vec{q}\vec{r}'} V(\vec{r}') d^3r'. \end{aligned} \quad (29)$$

Then, according to equation (16) the differential cross section $\sigma(\theta, \phi)$ is given by the square of the absolute value of the Fourier transformed potential $V(\vec{r})$

$$\sigma(\theta, \phi) = \frac{m^2}{4\pi^2\hbar^4} \left| \int e^{-i\vec{q}\vec{r}'} V(\vec{r}') d^3r' \right|^2. \quad (30)$$

2.2.3 Neutron scattering

So far the theory is universally valid for several probes. The main difference between neutrons and photons is the scattering at the samples. Neutrons in particular interact with the nuclei via the strong force, and with the unpaired shell electrons via the electromagnetic force and their magnetic dipole moment. Because of their rest mass they can also interact with the gravitational force. Furthermore they are unstable and decay because of the weak interaction. The strong interaction between neutrons and the nuclei of the sample acts in all scattering events of neutrons from atoms and can be described with help of the Fermi pseudopotential [19]

$$V(\vec{r}) = \frac{2\pi\hbar^2}{m} b\delta(r). \quad (31)$$

b is the scattering length with the dimension of a length and the product kb is in first order the phase difference of the incoming plane wave compared to the outgoing scattered spherical wave. Because the range of the nuclear potential is in the order of 10^{-15} m and the wavelength of thermal neutrons is in the order of 10^{-10} m the use of the δ -potential as a contact interaction is valid. Since

neutrons do not scatter at one but many scattering centres simultaneously, a mean phase difference can be used which in turn gives a coherent scattering length b_c [15]. The scattering at a macroscopic sample can then be described by the following potential

$$V(\vec{r}) = \frac{2\pi\hbar^2}{m} \sum_j b_j \delta(\vec{r} - \vec{r}_j). \quad (32)$$

Given equation (32) the differential cross section (30) can be calculated

$$\begin{aligned} \sigma(\theta, \phi) &= \frac{d\sigma}{d\Omega}(\vec{q}) = \frac{m^2}{4\pi^2\hbar^4} \left| \int e^{-i\vec{q}\vec{r}'} V(\vec{r}') d^3r' \right|^2 \\ &= \left| \int \sum_j b_j \delta(\vec{r}' - \vec{r}_j) e^{-i\vec{q}\vec{r}'} d^3r' \right|^2 \\ &= \left| \sum_j b_j e^{-i\vec{q}\vec{r}_j} \right|^2. \end{aligned} \quad (33)$$

The sum in equation (33) extends over all atoms. But the aim of (ultra) small-angle neutron scattering is the examination of macroscopic objects and not of individual atoms. Therefore, the scattering length b_j of each atom is replaced by the averaged scattering length density $\rho(r) = N(r)b_c$. Here, the averaging is taken over the macroscopic volume $v(\vec{r})$. With

$$\left\langle \sum_j b_j \delta(\vec{r} - \vec{r}_j) \right\rangle_{v(\vec{r})} = N(\vec{r})b_c(\vec{r}) = \rho(\vec{r}) \quad (34)$$

the macroscopic differential cross section can be written as

$$\frac{d\sigma}{d\Omega}(q) = \left| \int_V \rho(\vec{r}) e^{-i\vec{q}\vec{r}} d^3r \right|^2. \quad (35)$$

Equation (35) is fundamental for (ultra) small-angle neutron scattering. It indicates that the macroscopic differential cross section is proportional to the squared absolute value of the Fourier transformed scattering length density $\rho(\vec{r})$. One can write $\rho(\vec{r}) = N(\vec{r})b_c(\vec{r})$ as

$$\rho(\vec{r}) = \langle \rho \rangle + M(\vec{r}) \quad (36)$$

where the first term describes the scattering length density of a homogeneous, structureless part of the sample and $M(\vec{r})$ the scattering length density of the

sample in contrast to the homogeneous part. Therefore the sample can be described as a superposition of a structureless matrix $M(\vec{r}) = 0$ and inhomogeneities $M(\vec{r}) \neq 0$. $M(\vec{r})$ is the scattering length density contrast which is one of the most important parameter to describe (ultra) small-angle neutron scattering. This is because the larger $M(\vec{r})$, the higher the visibility of inhomogeneities [14].

2.2.4 Two-phase system

Further simplification of the differential cross section can be achieved by the two phase model. Here, a homogeneous scattering length density for the matrix $\rho_M = N_M b_{cM}$ is assumed. Equation (35) can then be written as

$$\frac{d\sigma}{d\Omega}(q) = \left| \int_V \rho_M(\vec{r}) e^{-i\vec{q}\vec{r}} d^3r + \int_{V-V_M} (\rho_s(\vec{r}) - \rho_M(\vec{r})) e^{-i\vec{q}\vec{r}} d^3r \right|^2 \quad (37)$$

with V as the volume of the sample and V_M the volume of the matrix [12], [20]. This can also be written as

$$\begin{aligned} \frac{d\sigma}{d\Omega}(q) &= (N_M b_{cM})^2 \left| \int_V e^{-i\vec{q}\vec{r}} d^3r \right|^2 \\ &+ 2(N_M b_{cM})(N_S b_{cS} - N_M b_{cM}) \operatorname{Re} \left[\int_V e^{-i\vec{q}\vec{r}} d^3r \int_{V-V_M} e^{-i\vec{q}\vec{r}'} d^3r' \right] \\ &+ (N_S b_{cS} - N_M b_{cM})^2 \left| \int_{V-V_M} e^{-i\vec{q}\vec{r}} d^3r \right|^2. \end{aligned} \quad (38)$$

For a macroscopic object $qr \gg 1$ is valid and the first two terms approaches a delta function $\delta(q)$ [14]. Therefore no scattering occurs and only the last term of equation 38 has to be considered and is simplified to

$$\begin{aligned} \frac{d\sigma}{d\Omega}(q) &= (N_S b_{cS} - N_M b_{cM})^2 \left| \int_{V-V_M} e^{-i\vec{q}\vec{r}} d^3r \right|^2 \\ &= (\Delta\rho)^2 \left| \int_V s(\vec{r}) e^{-i\vec{q}\vec{r}} d^3r \right|^2. \end{aligned} \quad (39)$$

$\Delta\rho$ is the scattering length density difference between matrix and scattered sample, the scattering contrast introduced in section 2.2.3, $s(\vec{r})$ is the shape function which describes the geometrical form of the scatterer. The integral is the form factor of the sample $F(\vec{q})$ and will be calculated for some geometries in the next chapter.

2.2.5 Simple form factors

Spherical particles

For spherical particles the scattering length density is isotropic and therefore only dependent on the radius r [21]

$$\Delta\rho(\vec{r}) = \Delta\rho(r). \quad (40)$$

Therefore the differential cross section is given as

$$\frac{d\sigma}{d\Omega}(q) = \left| \int \Delta\rho(r) e^{-i\vec{q}\vec{r}} d^3r \right|^2 = \left| \int \Delta\rho(r) r^2 \int e^{-i\vec{q}\vec{r}} d\Omega dr \right|^2. \quad (41)$$

The last integral can be written as followed:

$$\int e^{-i\vec{q}\vec{r}} d\Omega = \int_0^{2\pi} \int_0^\pi e^{-i\vec{q}\vec{r}} \sin(\theta) d\theta d\phi = \int_0^{2\pi} \int_0^\pi e^{-iqr\cos(\theta)} \sin(\theta) d\theta d\phi, \quad (42)$$

by substituting $\cos(\theta) = u$ equation (42) can then be solved

$$\int_0^{2\pi} \int_{-1}^1 e^{-iqr u} du d\phi = 2\pi \left(\frac{e^{-iqr} - e^{iqr}}{-iqr} \right) = \frac{4\pi}{qr} \sin(qr). \quad (43)$$

With the help of the inverse Fourier transform of $F(q) = \int F(r) \sin(qr) dr$,

$$F(r) = \frac{2}{\pi} \int F(q) \sin(qr) dq \quad (44)$$

the scattering length density can be written as

$$\Delta\rho(r) = \frac{1}{2\pi^2 r} \int \frac{d\sigma}{d\Omega}(q) q \sin(qr) dq. \quad (45)$$

This means that with the knowledge of the differential cross section the scattering length density can be calculated.

Furthermore, an unknown differential cross section can be obtained straight forward for a constant scattering length density $\Delta\rho(r) = \Delta\rho$,

$$\begin{aligned} \frac{d\sigma}{d\Omega}(q) &= \left| \frac{4\pi\Delta\rho}{q} \int r \sin(qr) dr \right|^2 = \left| \frac{4\pi\Delta\rho}{q} \left| \frac{\sin(qr) - qr \cos(qr)}{q^2} \right|_0^R \right|^2 \\ &= \left| 4\pi\Delta\rho \frac{\sin(qR) - qR \cos(qR)}{q^3} \right|^2 = (\Delta\rho)^2 V^2 \left[3 \frac{\sin(qR) - qR \cos(qR)}{q^3 R^3} \right]^2 \end{aligned} \quad (46)$$

$V = \frac{4\pi R^3}{3}$ is the volume and R the radius of the spherical particle.

The differential cross section behaves like the form factor which can be seen in figure 3. It shows a sequence of minima and maxima which is characteristic for this form factor. Different sizes will change the relative intensity as well as the position of these minima and maxima [12].

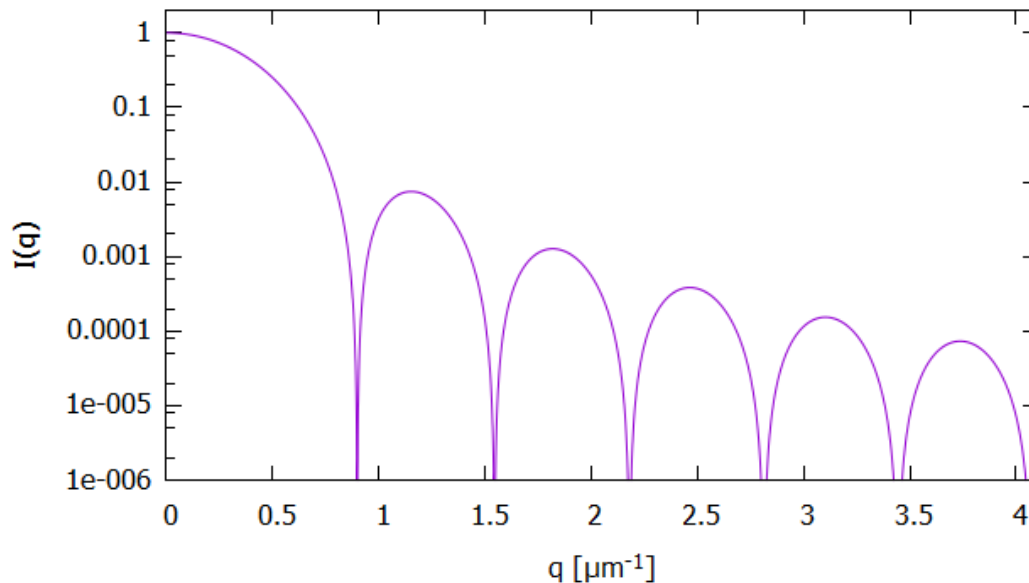


Figure 3: Form factor for a spherical sample with a radius of 5 μm .

Cylindrical particles

Another important geometry to consider is the one of a cylindrical particle. Under the assumption of a constant radius R_c as well as a length L far larger than R_c ($L \rightarrow \infty$), the scattering function $I_c(q)$ can be split into products for random orientation [22]. The differential cross section

$$\frac{d\sigma}{d\Omega}(q) = \frac{L\pi}{q} I_c(q) \quad (47)$$

is invalid for small angles since equation (47) diverges for $q \rightarrow 0$. While this does not matter for most small-angle scattering devices because they can not measure so close to the forward direction, for a double crystal spectrometer this has to be considered. Therefore equation (47) is not valid for this case. The

scattering function $I_c(q)$ for a cylindrical particle with an infinite length is

$$I_c(q) = \left[A \frac{J_1(qR_c)}{qR_c} \right]^2 \quad (48)$$

with $J_1(qR_c)$ as the first order spherical Bessel function. $I_c(q)$ exhibits several minima and maxima similar to equation (46).

Plate-like particles

The last special case which is considered in this thesis are plate-like particles with a constant thickness T and an area A with dimensions large compared to T . In a limiting case this goes to infinity ($A \rightarrow \infty$). Just like for an cylindrical particle, for random orientation the scattering function $I_p(q)$ can be split into products [22]. For small angles the differential cross section

$$\frac{d\sigma}{d\Omega}(q) = \frac{2\pi A}{q^2} I_p(q) \quad (49)$$

diverges again and the same is valid as for a cylindrical particle. The scattering function for a plate-like particle

$$I_p(q) = \left[T \frac{\sin(qT/2)}{qT/2} \right]^2 \quad (50)$$

also shows alternating minima and maxima similar to a cylindrical particle.

Guinier radius

It can be shown that for small scattering vectors with $qR \ll 1$ the square of the form factor can be written as

$$|F(q)|^2 \approx 1 - \frac{1}{3} R_g^2 q^2 \approx e^{-\frac{1}{3} R_g^2 q^2} \quad (51)$$

regardless of the particle's geometry [23]. R_g^2 is the radius of gyration and defined as [24]

$$R_g^2 = \frac{\int s(r) r^2 d^3r}{\int s(r) d^3r} = \frac{1}{V_p} \int_{V_p} r^2 d^3r. \quad (52)$$

Since $F(0) = 1$ the differential cross section can be written as

$$\frac{d\sigma}{d\Omega}(q) = \frac{d\sigma}{d\Omega}(0) e^{-\frac{1}{3} R_g^2 q^2} \quad (53)$$

which then leads to the Guinier law [25]

$$I(\vec{q}) = I(0)e^{-\frac{1}{3}R_g^2q^2}. \quad (54)$$

Although $F(q)$ is not directly dependent on the particle's geometry, R_g is:

$$\begin{aligned} Sphere : R_g &= \sqrt{\frac{3}{5}}R \\ Cylinder : R_{g_c} &= \frac{1}{\sqrt{2}}R \\ Plate : R_{g_p} &= \frac{1}{\sqrt{12}}T \end{aligned} \quad (55)$$

Porod law

In contrast to the Guinier approximation for small scattering vectors, the Porod law can be used for $qr \gg 1$ [26]. Generally the Porod approximation $I(q) \propto \frac{C_p}{q^4}$ is valid for any geometry. But since in equation (47) and (49) the factors $\frac{1}{q}$ and respectively $\frac{1}{q^2}$ are already included, the scattering curves I_c and I_t can be modified:

$$\begin{aligned} Sphere : I(q) &\propto \frac{C_p}{q^4} \\ Cylinder : I_c(q) &\propto \frac{C_p}{q^3} \\ Plate : I_p(q) &\propto \frac{C_p}{q^2}. \end{aligned} \quad (56)$$

In conclusion it is important to note that with help of the Guinier approximation, the size of the scattering sample can be obtained. While the Porod approximation delivers the geometry of the sample [12], [20].

3 Dynamical neutron diffraction

To calculate the rocking curve of an ideal crystal the kinematic theory of diffraction is not sufficient. It only takes the interaction of the system with the incident wave into consideration while neglecting the interaction of the waves inside the crystal. Therefore the dynamical diffraction theory has to be used [27].

For this the Schrödinger equation needs to be solved for neutrons inside the crystal,

$$\left\{ \frac{-\hbar^2}{2m} \Delta + V(\vec{r}) \right\} \Psi(\vec{r}) = E \Psi(\vec{r}) \quad (57)$$

with the following ansatz:

$$\begin{aligned} \Psi(\vec{r}) &= e^{i\vec{K}\vec{r}} u(\vec{r}) \\ u(\vec{r}) &= \sum_{\vec{H}} u(\vec{H}) e^{i\vec{H}\vec{r}}. \end{aligned} \quad (58)$$

$V(\vec{r})$ is the potential, \vec{r} the position vector and \vec{H} a reciprocal lattice vector.

As already mentioned neutrons mainly interact with the nuclei which can be described by the Fermi pseudo potential [19]

$$V(\vec{r}) = \frac{2\pi\hbar^2 b_c}{m} \sum_j \delta(\vec{r} - \vec{r}_j). \quad (59)$$

b_c is the coherent scattering length and \vec{r}_j the position vector of atom j in the lattice. The Fermi pseudo potential can also be expressed in a Fourier series

$$V(\vec{r}) = \sum_{\vec{H}} V(\vec{H}) e^{i\vec{H}\vec{r}} \quad (60)$$

which shows the lattice periodicity. With equation (58) and (60) as well as the Schrödinger equation (57) one gets the fundamental equation of dynamical diffraction

$$\left[\frac{\hbar^2}{2m} \left| \vec{K} + \vec{H} \right|^2 - E \right] u(\vec{H}) = - \sum_{\vec{H}'} V(\vec{H} - \vec{H}') u(\vec{H}'). \quad (61)$$

\vec{k} is the wave vector in vacuum, \vec{K} the wave vector in the crystal, $E = \frac{\hbar^2 k^2}{2m}$ the energy of the neutrons and $V(\vec{H} - \vec{H}')$ the component for the reciprocal lattice vector $\vec{H} - \vec{H}'$. Equation (61) is a homogeneous differential equation which only

has a non trivial solution for certain values of \vec{K} . Since the energy E is about five orders of magnitudes larger than V several approximations can be done.

It is important to note that only if

$$\vec{Q} = \vec{k}' - \vec{k} \approx \vec{H} \quad (62)$$

is valid the observed intensity is significant. The Laue equation (62) is the vector form of the Bragg equation [28]

$$n\lambda = 2d \sin\theta. \quad (63)$$

3.1 Two-beam approximation

In the following a two-beam approximation is assumed. This means that only the zero vector $\vec{0}$ and one reciprocal lattice vector \vec{H} is close to the Ewald sphere. It can be shown that with increasing distance the intensity of the beams goes quickly to zero. This is the reason why this approximation describes crystal interferences quite well. [27].

Under the assumption that the difference of the wave vector inside the crystal compared to outside the crystal is small, the following equations are valid:

$$\begin{aligned} |\vec{K}| &= k(1 + \epsilon) \\ |\vec{K} + \vec{H}| &= k(1 + \epsilon_H) \end{aligned} \quad (64)$$

with ϵ and ϵ_H as excitation errors.

With the conditions for continuity it can be shown that ϵ and ϵ_H depend on each other. This can be seen with

$$|\vec{K} + \vec{H}|^2 = K^2 + H^2 + 2\vec{K}\vec{H} \quad (65)$$

and equation (64),

$$k^2(1 + 2\epsilon_H) = k^2(1 + 2\epsilon) + H^2 + 2\vec{K}\vec{H}. \quad (66)$$

For solving equation (61), equation (64) is needed again which leads to

$$\begin{aligned} \left(2\epsilon + \frac{V(0)}{E}\right) u(\vec{0}) + \frac{V(-H)}{E} u(\vec{H}) &= 0 \\ \frac{V(H)}{E} u(\vec{0}) + \left(2\epsilon_H + \frac{V(0)}{E}\right) u(\vec{H}) &= 0. \end{aligned} \quad (67)$$

After several steps one gets the wave function in forwards direction

$$\Psi_0(\vec{r}) = e^{i\vec{k}\vec{r}} \left[u_1(\vec{0}) e^{\frac{ik\epsilon_1 \vec{n}\vec{r}}{\cos(\gamma)}} + u_2(\vec{0}) e^{\frac{ik\epsilon_2 \vec{n}\vec{r}}{\cos(\gamma)}} \right] \quad (68)$$

as well as in direction of the lattice vector (\vec{H})

$$\Psi_H(\vec{r}) = e^{i(\vec{K}+\vec{H})\vec{r}} \left[u_1(\vec{H}) e^{\frac{ik\epsilon_1 \vec{n}\vec{r}}{\cos(\gamma)}} + u_2(\vec{H}) e^{\frac{ik\epsilon_2 \vec{n}\vec{r}}{\cos(\gamma)}} \right]. \quad (69)$$

where \vec{n} is the surface normal, γ the angle between \vec{k} and \vec{n} and $\epsilon_{1,2}$ solutions for the excitation errors [27].

3.2 Bragg diffraction

In this section it is assumed that an incoming neutron beam will interact with a non-absorbing parallel perfect crystal plate which forms part of a double crystal spectrometer. The incident neutron beam can be described as a plane wave

$$\Psi_i = u_0 e^{i\vec{k}\vec{r}}. \quad (70)$$

Part of this wave will go through the plate without diffraction, while the other part will be diffracted as can be seen in figure 4.

There are two boundary conditions for Bragg diffraction. The first one, which is also valid for Laue diffraction, is the continuity condition of the incoming plane wave and the outgoing one in the forward direction ($\vec{n}\vec{r} = 0$) which leads to

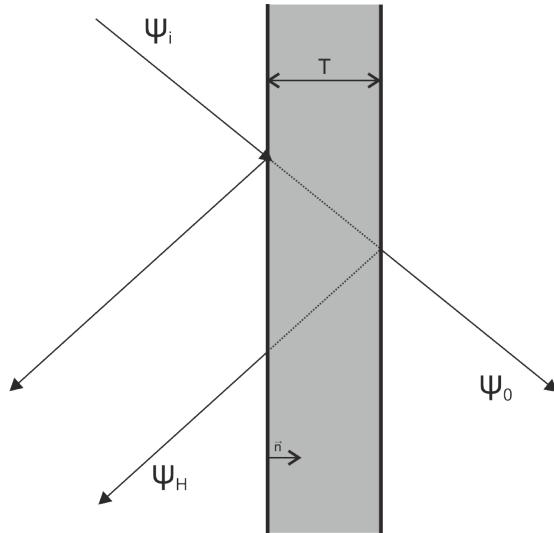


Figure 4: Sketch of the beam path for Bragg diffraction.

$$u_1(\vec{0}) + u_2(\vec{0}) = u_0. \quad (71)$$

The second condition, which is a special case for Bragg diffraction, postulates that there is no diffracted outgoing beam on the backside of the plate ($\vec{n}\vec{r} = T$). The diffracted part is on the front side just like the incident beam. This leads to

$$u_1(\vec{H})e^{\frac{ik\epsilon_1 T}{\cos(\gamma)}} + u_2(\vec{H})e^{\frac{ik\epsilon_2 T}{\cos(\gamma)}} = 0. \quad (72)$$

With both boundary conditions as well as equation (68) and (69), the intensity ratio of diffracted to incident beam $\frac{I_H}{I_i}$, also known as the reflection probability, is

$$\frac{I_H}{I_i} = \left| \frac{\psi_{H(0)}}{\psi_i} \right|^2 = \frac{1}{y^2 + (y^2 - 1) \cot^2 \left(A \sqrt{y^2 - 1} \right)}. \quad (73)$$

Here the generalised angle y is given as

$$y = \frac{(b-1)\frac{V(0)}{E} + \alpha b}{2\sqrt{|b|} \left| \frac{V(\vec{H})}{E} \right|} \quad (74)$$

with $b = \frac{\cos(\gamma)}{\cos(\gamma_H)}$, γ_H the angle between \vec{k}' and \vec{n} , $\alpha = 2(\theta_B - \theta)\sin(2\theta_B)$, and A as

$$A = \frac{k}{2} \frac{1}{\sqrt{|\cos(\gamma)\cos(\gamma_H)|}} \frac{V(\vec{H})}{E} T. \quad (75)$$

For $|y| > 1$ the intensity I_H shows strong oscillations coming from the term $\cot^2 \left(A \sqrt{y^2 - 1} \right)$. On the other hand for $|y| < 1$ the intensity ratio approaches one ($\frac{I_H}{I_i} = 1$) which means total reflection. This can be seen in figure 5. It is important to note that the larger A is, and therefore the thicker the crystal, the closer the oscillations are. At some point they are so close that they can not be distinguished experimentally. The intensity ratio can then be written as

$$\frac{I_H}{I_i} = R(y) = \begin{cases} 1, & |y| \leq 1 \\ 1 - \sqrt{1 - \frac{1}{y^2}}, & |y| > 1. \end{cases} \quad (76)$$

For a sufficiently thick crystal the intensity ratio can be seen in figure 5.

The range of total reflection $1 > y > -1$ can be given in units of angle $\Delta\theta$ as follows:

$$\Delta\theta = \frac{b_c N \lambda^2 |F|}{4\pi \sin(2\theta_B)} \sqrt{\left| \frac{\cos(\gamma_H)}{\cos(\gamma)} \right|} e^{-(B/4d^2)} \quad (77)$$

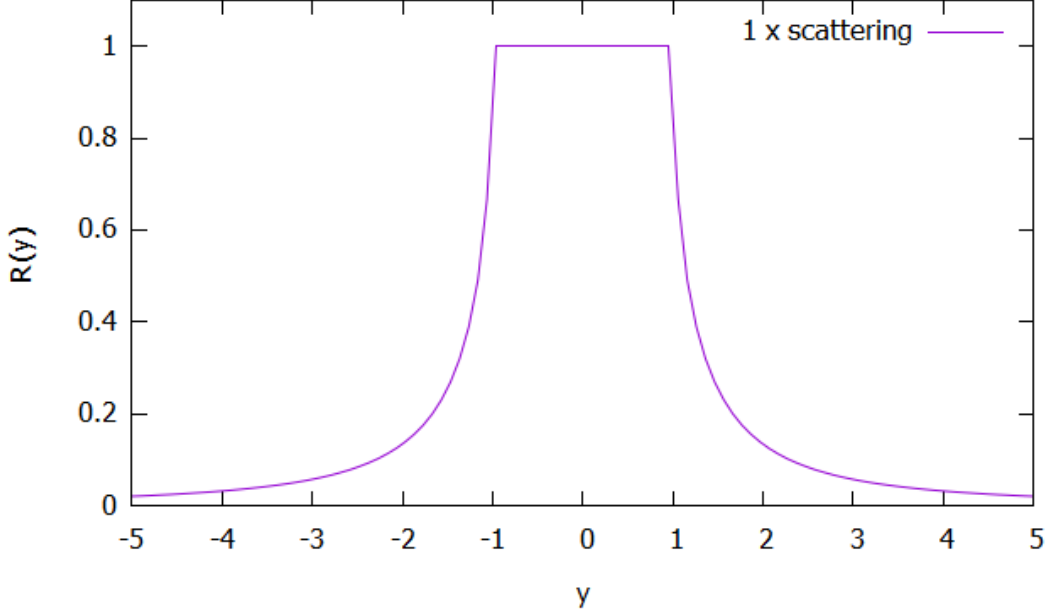


Figure 5: Intensity ratio for simple scattering at a crystal with sufficient thickness.

with F as the structure factor, N the number of atoms and $e^{-(B/4d^2)}$ the Debye-Waller factor. The parameters for the Si crystal of the USANS device in Vienna are as followed: $a = 5.431 \text{ \AA}$, $N = 4.995 \times 10^{28} \text{ m}^{-3}$ [7], $b_c = 4.151 \text{ fm}$ [29], $\lambda = 1.76 \text{ \AA}$, $B = 0.46 \text{ \AA}^2$, $F = 4 + 4i$ and $2\theta_B = 90^\circ$. With this equation (77) becomes

$$\Delta\theta = 2.685 \mu\text{rad} \quad (78)$$

As can be seen in figure 5 the function's tail only decreases slowly. This behaviour may pose a serious difficulty in the observation of scattering with scattering angles close to the region of total reflection. One solution to this problem is by using not one but multiple reflections m at the crystal. The crystal is then realised as a so-called channel-cut crystal which allows for multiple reflections across the channel. The higher m the steeper the function becomes since the intensity ratio is exponentiated with m [30], [1]

$$R_m(y) = (R(y))^m. \quad (79)$$

Here $R_m(y)$ is the crystal reflection function and m the number of reflections. Now the reflection curve for a crystal with sufficient thickness (76) can be written as

$$R(y) = \frac{I_H}{I_i} = \begin{cases} 1, & |y| \leq 1 \\ \left(1 - \sqrt{1 - \frac{1}{y^2}}\right)^m, & |y| > 1. \end{cases} \quad (80)$$

This is plotted in figure 6 and one can see that even with $m = 3$ a big improvement compared to simple scattering is given.

In ultra-small-angle neutron scattering not one but two crystals are used. At each of them multiple reflection occurs. The first crystal, the monochromator, is held fixed while the second, the analyser, is rotated. The total intensity at a certain position of the analyser is then given as the convolution of the reflection curve of each crystal

$$I(\Delta) = \int (R(y))^n (R(y + \Delta))^m dy \quad (81)$$

with $I(\Delta)$ as the rocking curve, Δ the reduced angle parameter for the angular difference of the two crystal positions, n the number of reflections in the monochromator and m the number of reflections in the analyser crystal [12].

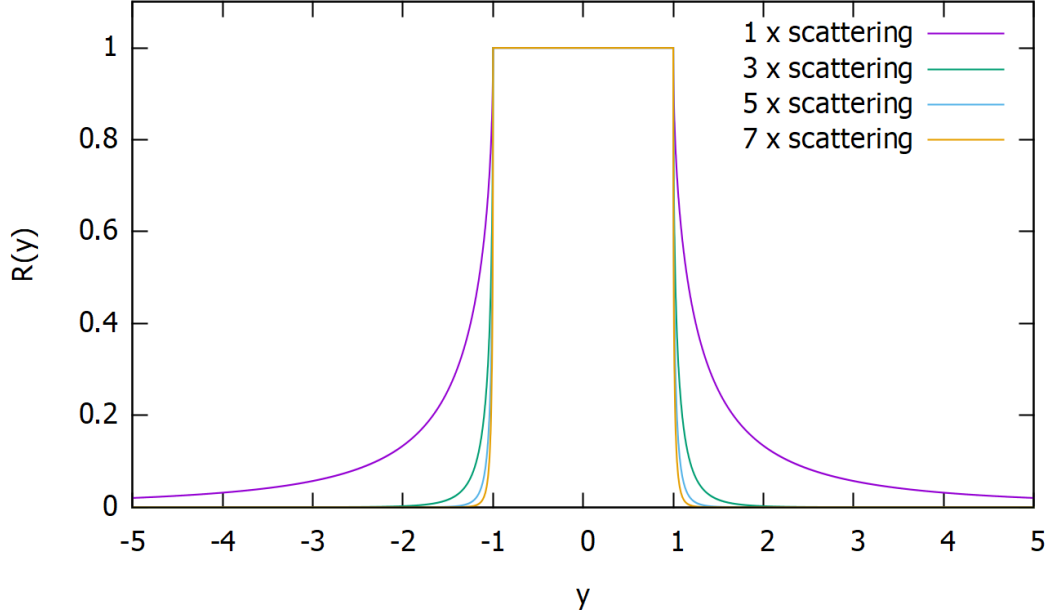


Figure 6: Reflectivity at multiple reflections from a crystal with $m = 3, 5$ and 7 compared to simple scattering. The larger m the closer it gets to a rectangular function.

As can be seen in figure 7 the more often the neutron beam is reflected at each crystal the steeper the curve gets. Ideally for an infinite number of reflections the curve is a triangle function. But in the real world more reflections means larger crystals, more difficult alignment and less intensity. So there has to be compromises. As figure 7 shows the 3×3 reflection is already pretty close to a triangle function. Therefore the USANS device in Vienna, which was used in this thesis, uses three reflections in each crystal ($m = n = 3$) [12].

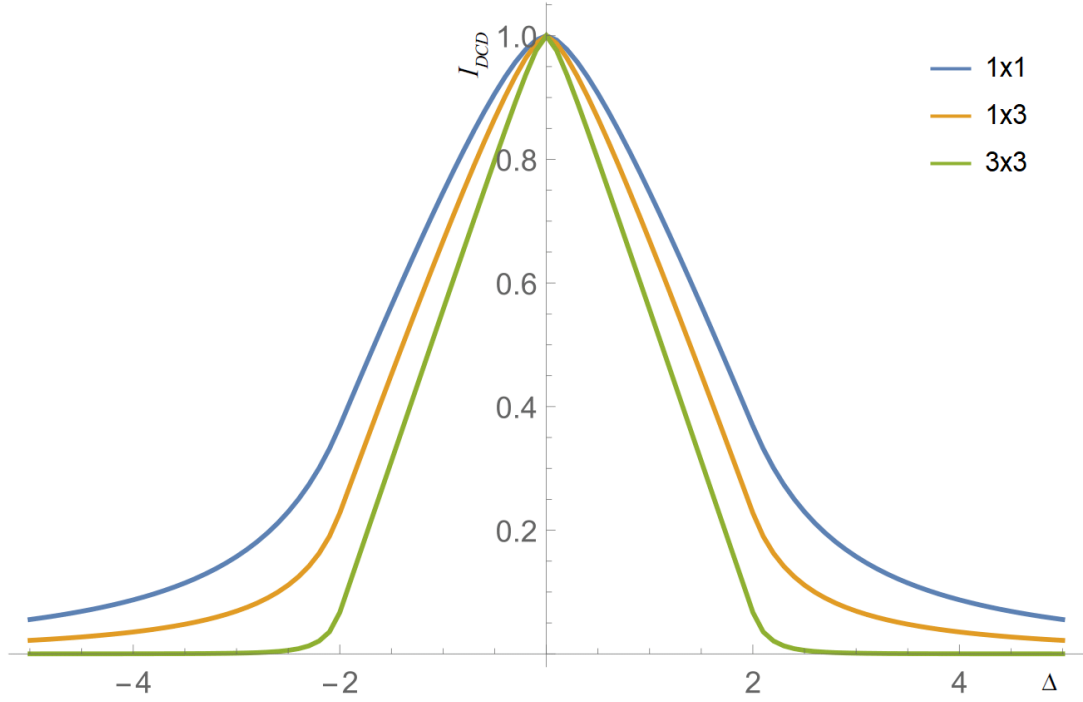


Figure 7: Comparison of theoretical convolution curves with multiple reflections. Each curve is normalised to 1 at $\Delta=0$. The neutrons are reflected once at each crystal (blue), once at one crystal and three times at the other (red), and three times at each crystal (green).

4 USANS in Vienna

The neutron source for the USANS instrument is the TRIGA Mark II reactor which is located in the Viennese Prater.

4.1 TRIGA-reactor

This master's thesis has been conducted at the TRIGA Mark-II reactor of the Atominstitut. TRIGA stands for: Training, Research, Isotope Production, General Atomic. It is purely used as a research reactor for neutron extraction and is a swimming-pool type. This means that the fuel elements as well as the control rods are immersed in an open pool of water.

The reactor was installed during the years 1959 through 1962. It can output 250 kW of thermal power continuously and up to about 250 MW in pulsed operation. In continuous mode the maximum neutron flux density is approximately $10^{13} \text{ cm}^{-2}\text{s}^{-1}$ in the core centre which can go up to $10^{16} \text{ cm}^{-2}\text{s}^{-1}$ in pulsed mode. The fuel elements consist of 8 wt% uranium, 91 wt% zirconium and 1 wt% hydrogen. Most of the neutron moderation is done in the fuel elements itself and not by the surrounding water. As a result the moderation gets worse the higher the core temperature gets and fewer nuclei are split. This has the advantage that the reactor can regulate itself and therefore a pulsed operation is possible. For the duration of this thesis the reactor was only running in continuous mode.

The reactor is controlled by three control rods. Each of them consist of boron carbide which is an excellent absorber material. If they are fully inserted into the reactor core the rods absorb most of the neutrons which are continuously emitted from a start-up source (Sb-Be photo-neutron source). Therefore the reactor remains sub-critical. Two of the control rods are controlled with an electric motor and the other one pneumatic. In just 1/10 of a second the three control rods can be dropped back into the reactor core and shut it down [31]. The TRIGA II reactor has a total of four beamlines as can be seen in the cross section in figure 8. The USANS facility is positioned at beamline C.

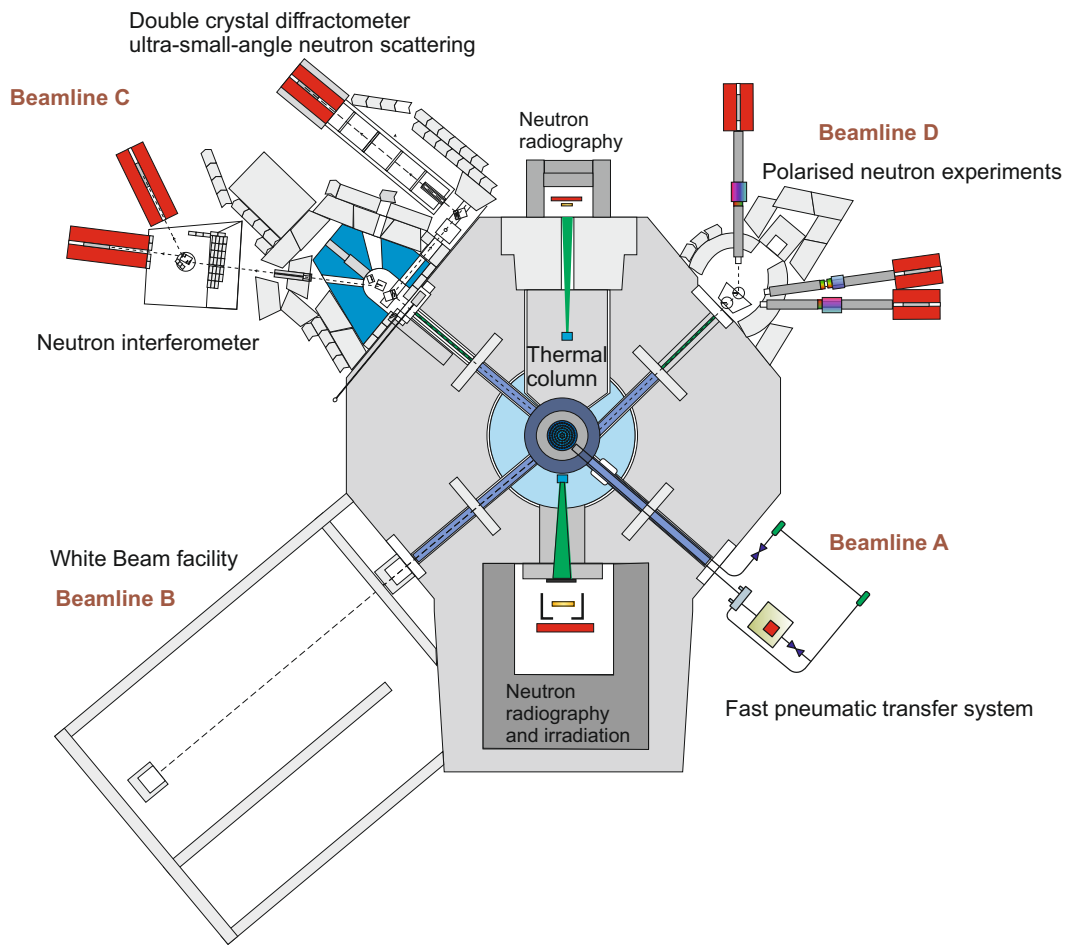


Figure 8: The cross section of the TRIGA Mark II reactor in Vienna. The USANS facility is located at beamline C (top left side) [32].

4.2 Setup

The USANS setup of the Atominstitut can be seen in figure 9.

It is a double crystal diffractometer which uses two perfect channel-cut Silicon crystals. The incoming beam is diffracted at the monochromator crystal, going through the sample and to the analyser crystal. On each crystal a triple bounce occurs. This setup is known as a Bonse-Hart camera since it was first introduced for X-rays by Bonse and Hart [1].

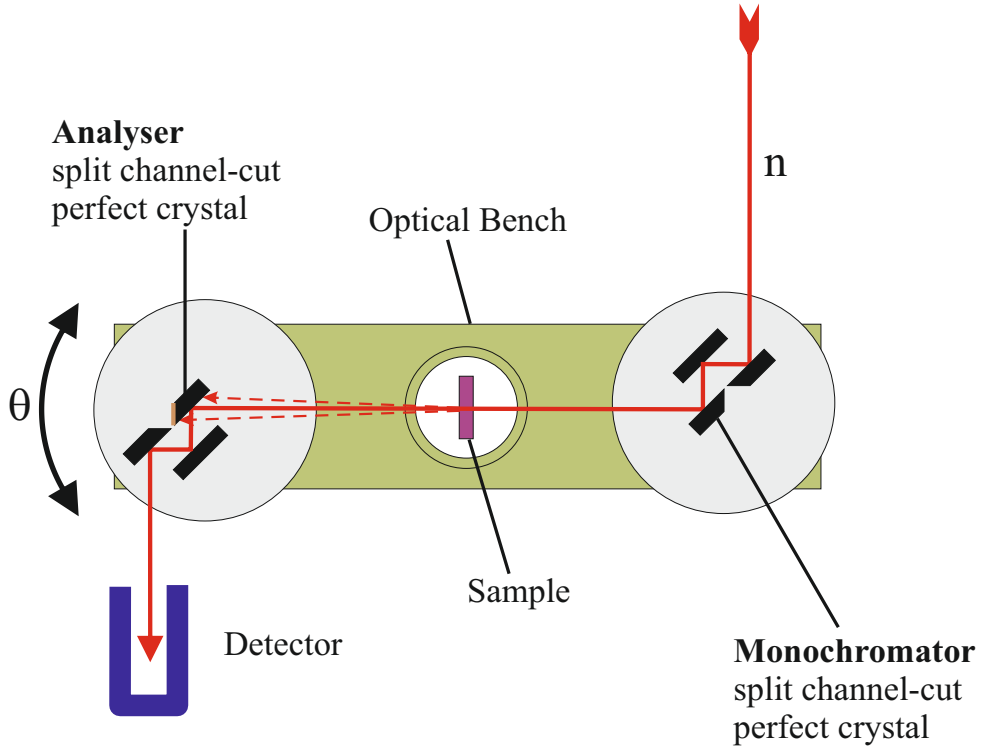


Figure 9: Sketch of the Bonse-Hart camera on the optical bench with triple-bounce monochromator and analyser crystal [32].

4.2.1 Neutron beam

As already mentioned in the previous section, the neutron beam is diffracted three times at each crystal. For a better signal-to-noise ratio the longer crystal plates have cuts in them where cadmium is placed as can be seen in figure 10. This makes sure that no neutrons may propagate parallel to the surfaces through

the crystal plates. This configuration was invented by M. Agamalian et al. in the late 1990ies [33].

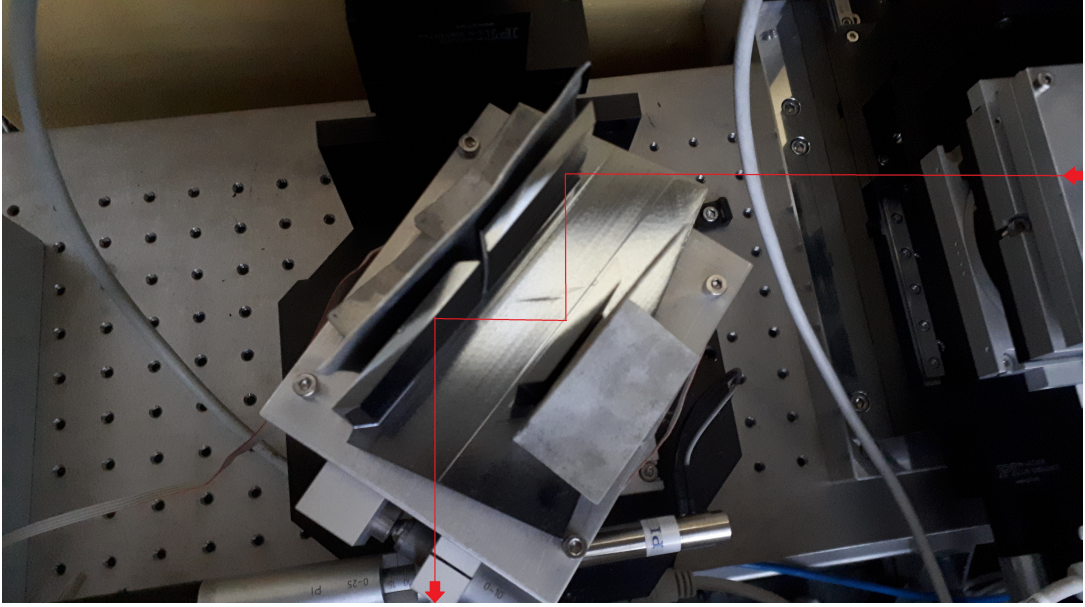


Figure 10: This picture shows the analyser crystal with several pieces of cadmium shielding. The neutron beam comes from the right side and is reflected three times. After that it continues to the bottom of the image where the BF_3 detector is placed.

The neutron beam leaving the reactor tank has a Maxwell-Boltzmann wavelength distribution. Then the monochromator crystal selects a small wavelength band around a particular central wavelength and reflects it towards the analyser crystal. The angle between the neutron beam and the monochromator is close to $\theta_B = 45^\circ$ and the used lattice plane of the silicon crystal is (331) [34]. With the Bragg equation [28]

$$n\lambda = 2d \sin\theta \quad (82)$$

the wavelength λ can be calculated. d stands for the lattice spacing, θ the scattering angle and n is a positive integer. An illustrative sketch of the Bragg reflection can be seen in figure 11. For obtaining the wavelength λ , the interplanar spacing d is needed first. Since the Silicon crystal has a cubic structure d can be determined as

$$d_{hkl} = \frac{a}{\sqrt{h^2 + k^2 + l^2}} \quad (83)$$

with the Miller indices h , k and l , and a the lattice constant. In our case and with $a = 5.431 \text{ \AA}$ [7] this becomes

$$d_{331} = \frac{a}{\sqrt{3^2 + 3^2 + 1}} = 1.246 \text{ \AA}. \quad (84)$$

The wavelength λ is then given as

$$\lambda = 2d_{331} \sin(45^\circ) = 1.76 \text{ \AA}. \quad (85)$$

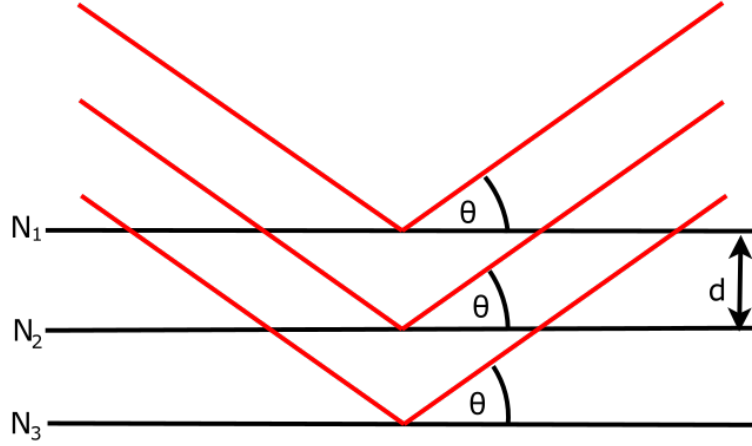


Figure 11: Sketch of the Bragg reflection of neutrons a specific set of lattice planes. d stands for the distance between the lattice planes also known as interplanar spacing. For Bragg reflection to take place, the partial waves have to interfere constructively.

4.2.2 Detector

The monochromator crystal is outside of the reactor but shielded by a concrete wall. The sample as well as the analyser and detector are outside of that shielding. A small hole in the concrete shielding is needed that the thermal neutrons can move from the monochromator crystal to the sample where they are scattered to the analyser crystal. The analyser crystal can be tilted and rotated. Only if the rotation angle is right, so that analyser and monochromator are essentially parallel, a signal can be detected by the Boron Trifluoride (BF_3) neutron detector. While the sample holder and analyser crystal are on a vibration isolated optical bench, the detector is on a separate aluminium frame. The cylindrical detector itself is 360 mm long and has a diameter of 50 mm.

Furthermore it is enclosed in a paraffin cylinder which is 800 mm long and the diameter is 410 mm. In front of this enclosure a collimator is placed as well. The applied voltage at the BF_3 detector is 2.6 kV. The signal of this detector goes to an analog ratemeter which converts the detected neutrons as a clicking noise. Furthermore, part of the outgoing detector signal is converted into an digital one and is analysed by a LabVIEW program. Additionally to this detector a neutron monitor is also installed between the sample holder and the monochromator. The monitor is operated with 800 V. It is a ^3He detector with a length of 80.5 mm and the diameter is 10 mm. The reasons for this additional detector are to see if neutrons are coming from the monochromator at all and to normalise the intensity measured at the BF_3 detector. This is important because the total neutron intensity outputted by the reactor fluctuates.

4.2.3 Measurement

For a typical measurement a sample must be placed on the sample holder first. During the measurement process the monochromator and the sample stand still while the analyser crystal rotates stepwise. In a first run we change the analyser angle with a rather large step size with a short measuring time for each point. This is just to find the position of the neutron peak. This process normally takes a couple minutes and the found peak position is then used for the real measurement. This can take up to several hours. It is basically the same as the fast one with the difference that the starting point is set to the position where the neutron peak was found before. Furthermore the step size is reduced and the measuring time increased. The exact parameters are chosen in order to optimise counting statistics. The LabVIEW program called "Peaksuche_2017" allows to set different measurement parameters for different ranges. The parameters are the piezo range, the step size as well as the measurement time per point for each area. This way a different acquisition time per measuring point outside of the neutron peak compared to the peak centre is possible and allows to obtain a better statistical signal of the background while still providing a reasonable total measurement time. During this whole process the neutron beam intensity is plotted as a function of the rotation angle and can be analysed afterwards. The underlying theory for this can be seen in section 3. To determine the rotation angle a high-resolution angle measurement device of the RON series from

Heidenhain is used. This is placed beneath the analyser crystal and connected to its rotation axis, therefore a change of the rotation angle of the crystal is measured.

4.2.4 Movement of analyser

The rotation table where the analyser crystal is mounted onto can be rotated either with the help of a DC-actuator or a piezo actuator. For the actual measurement the piezo actuator is used since it has a higher accuracy. Furthermore no backlash compensation is necessary compared to the DC motor. The units of the motor movement are given in counts and the unit of the piezo crystal is μm . The analyser is placed on a "Tangent-Arm Rotation Stage" of the series M-036 from Physik Instrumente. It has a rotation to linear input ratio of $15 \frac{\mu\text{rad}}{\mu\text{m}}$. This means if the piezo is changed by $1 \mu\text{m}$ the analyser rotates $15 \mu\text{rad}$. For the DC-motor the counts have to be converted into a change of length. The parameter for this is given in table 2.

Series	$[\frac{\text{positions}}{\text{rev}}]$	Gear ratio	$[\frac{\text{mm}}{\text{rev}}]$	Range [mm]	$[\frac{\text{counts}}{\text{rev}}]$
M-227-25	2048	69.12:1	0.5	25	141 558

Table 2: Different parameters of the DC motor responsible for rotating the analyser crystal.

While the DC motor is not used for the actual measurement it still has its uses. It has a wider range of operation compared to the piezo actuator. The piezo can only be operated in the range of $0 \mu\text{m}$ to $45 \mu\text{m}$ while the DC-motor has a design range of 7 077 888 counts. The range in μrad as well as the transmission factor, which gives the amount of $\mu\text{m} \setminus \text{counts}$ needed to rotate the analyser crystal for $1 \mu\text{rad}$, is given in table 3.

	transmission factor	relative range [μrad]
Piezo	$0.06 \mu\text{m} \hat{=} 1 \mu\text{rad}$	675
DC-motor	$18.9 \text{ cts} \hat{=} 1 \mu\text{rad}$	360 000

Table 3: Comparison of the conversion factor as well as the range of the piezo actuator and DC-motor.

With the much wider range the DC-motor has its own application outside of a measurement. If for example the neutron peak is at a piezo position outside or at the edge of the piezo range, the DC-actuator is used. It can rotate the analyser such that the neutron peak position is now in the centre of the piezo actuator's range. Then the piezo can be used again for the actual measurement.

The analyser can also be tilted with the help of a DC-motor and a tilt stage. The transmission ratio is $65 \frac{\mu m}{\mu rad}$. The DC-actuator is the same as in table 2 which leads to a transmission factor of $4.356 \frac{cts}{\mu rad}$.

The analyser crystal can not only be rotated but also moved horizontally and vertically. To achieve this it is placed on a linear translation stage of the series M-403 which is moved with the help of DC-motors. The same is true for the sample holder. The unit of the DC-actuators are again given in counts which can be converted to millimetres. The conversion factor as well as the range is given in table 4 and additional parameters can be found in table 5.

	Range [mm]	Range [cts]	Transmission factor
M-403.6DG	150	8 533 332	$56\,888.8 \text{ cts} \hat{=} 1 \text{ mm}$
M-403.4DG	100	5 688 888	
M-403.2DG	50	2 844 444	

Table 4: Linear translation stages for analyser and sample holder. They only differ in the range.

Series	$[\frac{positions}{rev}]$	Gear ratio	$[\frac{mm}{rev}]$	$[\frac{counts}{mm}]$
M-403	2000	2304:81	1	56888.9

Table 5: Additional parameters of the linear translation stage M-403.

4.2.5 Analysis of data points and fitting procedure

The obtained data of an USANS measurement are analysed with the program IGOR by WaveMetrics. There the measured intensity is plotted as a function of the measured rotation angle and a corresponding function is fitted. In an ideal case, with an infinite number of reflection, the intensity behaves like a triangular function. This is motivated by the fact that the convolution of two rectangular

functions, as it is the case with the monochromator and analyser crystal, is a triangular function. This was already discussed in section 3. However, in reality only three reflections occur at each crystal which results in a tail as can be seen in figure 20. Therefore the fitting function has to be adapted. In our case the fitting function $R(\theta)$ is a triangle function combined with a Gaussian curve [3]

$$R(\theta) = A_t \Lambda \left(\frac{\theta - \theta_i}{\tau} \right) + A_0 \mathcal{N}(\theta_i, \sigma_0^2) \quad (86)$$

where Λ is the triangular function centred at θ_i with width τ and amplitude A_t and $\mathcal{N}(\theta_i, \sigma_0^2)$ is a Gaussian centred at θ_i with width σ_0 and amplitude A_0 .

5 Measurements and results

In this section every change of the instrument as well as the corresponding measurement results are given and discussed in chronological order. It is divided into six major subsections. In the first one, the original setup was examined and a PC migration took place. Essentially the setup stayed the same hence the name "Original setup" (5.1). The goal of the next section (5.2) was the characterisation of the neutron beam size as well as the intensity distribution. For this some basic improvements and re-installations were done, such as adding a neutron monitor (5.2.2) and measuring the peak intensity at different tilt angles ρ (5.2.5). Furthermore, the first lattice measurements (5.2.7) took place and the background intensity (5.2.8) was examined. In the next subsection called "Improved setup" (5.3) the detector setup was reconfigured. The goal was to increase the measured neutron intensity by moving the shielding barrel of the detector. The collimator was mounted on the paraffin wax barrel in which the detector is positioned. After that the detector position had to be "re-aligned". Furthermore the analyser crystal was moved for the first time in years and a problem with the detector connection was observed. It partially emitted a wrong signal. So it had to be investigated. After that a planned power cut occurred which reset some of the instrument components. Therefore, in the next subsection (5.4) some measurements which were already done were repeated, such as further adjustment of the analyser and detector position. The next subsection is called "Monochromator" (5.5) because the monochromator shielding was opened for the first time in years. This was originally done to install a temperature sensor to further investigate the temperature dependence of the setup. But furthermore a cadmium plate was removed which yielded a different neutron intensity of the monitor. In the last section (5.6) the results of the newly installed temperature sensor were analysed. There a clear dependence of the measured rotation angle and the temperature is observable.

5.1 Original setup

As already mentioned before, the aim of this master's thesis was the characterisation as well as testing the ultra-small-angle neutron scattering facility. The logical approach to this topic was examining the original setup and conducting

several basic measurements with the USANS instrument. First, this was done to acquaint oneself to the facility, second, to see how well everything worked before making any changes. So several measurements, which were already introduced in section 4.2.3, were done at different tilt angles to identify the position with the highest peak intensity. It is important to note that these measurements were done with a low measuring time per point compared to the measurements which were conducted at a later time. After the maximum intensity was found and the reactor was out of order for a few days the PC migration could begin. The old system (PC with Windows XP) was replaced by a newer one (PC with Windows 8).

5.1.1 PC migration

As already mentioned in section 4.2.3 a measurement is conducted by rotating the analyser crystal with the help of a piezo-actuator. DC-actuators are also included in the instrument and are used to move the sample as well as the analyser crystal. Last but not least the signal of the neutron detectors and the angle measurement device RON have to be processed as well. All of this is done with LabVIEW programs which were installed on a PC with Windows XP as operating system. For communication between the hardware instruments and the LabVIEW software, several additional hardware components are needed.

The IK 220 is an evaluation electronic PCI card which is the interface between the angle measurement device RON and the PC. It was installed on the motherboard of the old PC and had to be removed for migrating to the new PC.

An MXI-Express card is the host controller between the PC and the PXI-1033 chassis. In the chassis several motion control modules, responsible for communication between the DC-actuators and the host controller, are installed. For migrating to the new PC with the newer operating system Windows 8, the MXI-Express card had to be re-installed to the new system.

The E-816 computer interface and command interpreter submodule for piezo controller had to be re-installed to the new PC. It is in turn connected to the PI-E665XR piezo amplifier and allows moving the piezo actuator with the help of LabVIEW programs.

After the communication cards were installed in the new system, the required drivers were downloaded and installed. Additionally two rails were attached at

the new PC to mount it on a server rig. This lead to more space on the workstation while still allowing easy access to the PC if something had to be changed in the future. Then the LabVIEW programs for controlling the instrument were moved to the new system.

Although all the drivers were up to date and the LabVIEW programs did run, a problem occurred. The piezo actuator did not move properly and therefore no measurement could be done. It was probably a problem with the different LabVIEW versions. On the old system LabVIEW 8.6 was installed, while the new one had the more recent version LabVIEW 2016. After a long search the solution was to change the time delay for communication in the programs “Piezo_move.vi” and “Piezo_move2.vi”. They were set to only 1 ms which seemed to work on the old system but not on the new one. Changing it to 100 ms did the trick and everything worked fine again.

5.1.2 New System

On the old system the relative tilt angle ρ was set to 8700 counts but because of the power cut during the PC migration, this value was automatically set as a new reference point. Therefore it read 0 counts although the physical angle position did not change. To see if an actual physical tilting occurred during the change of setup, a quick measurement at different tilt angles ρ was conducted. The maximum neutron intensity was found at $\rho = -600$ counts, which corresponds to $\rho = 0.008^\circ$.

5.2 Characterisation of the neutron beam -size and intensity distribution

The goal of this section is characterising the neutron beam, its size as well as the intensity distribution. Experimentally this can be done by scanning the neutron beam with the help of boron-carbide containing rubber mat screen with a square hole. They are placed in such a way that only part of the neutron beam reaches the analyser crystal and is therefore detected and analysed. By moving this screen the neutron intensity can be analysed at different positions and also the overall beam size can be approximated. For this a sample holder was installed between the analyser and monochromator crystal. In the holder

such a boron-carbide screen with a square hole of 1 cm^2 ($10\text{ mm}\times 10\text{ mm}$) was mounted. The screen can be seen in figure 12.

The sample holder can be moved horizontally and vertically via a DC-actuator. For moving, the program MAX (Measurement and Automation Explorer) from National Instrument was used since the moving was not implemented in any LabVIEW program yet. However this changed in the upcoming months since Markus Demel, who did a project thesis [35], wrote such program. Similar to the tilt angle, the moving was given in counts. The transmission factor is given in table 4. In this case M-403.6DG is responsible for horizontal movement and M-403.4DG for vertical movement. The sample holder was moved in 10 mm steps. A negative horizontal movement meant moving away from the reactor while a negative vertical movement meant upwards. Five measurements were done each with a different horizontal position but no neutron peak was detected. For checking purpose the sample holder was removed and new peak searches with different tilt angles were done. Since still no neutron peak was found the detector was removed and re-installed. Afterwards it seemed to work again. This was the first indication of a problem with the neutron detector. The problems continued in section 5.3.5.

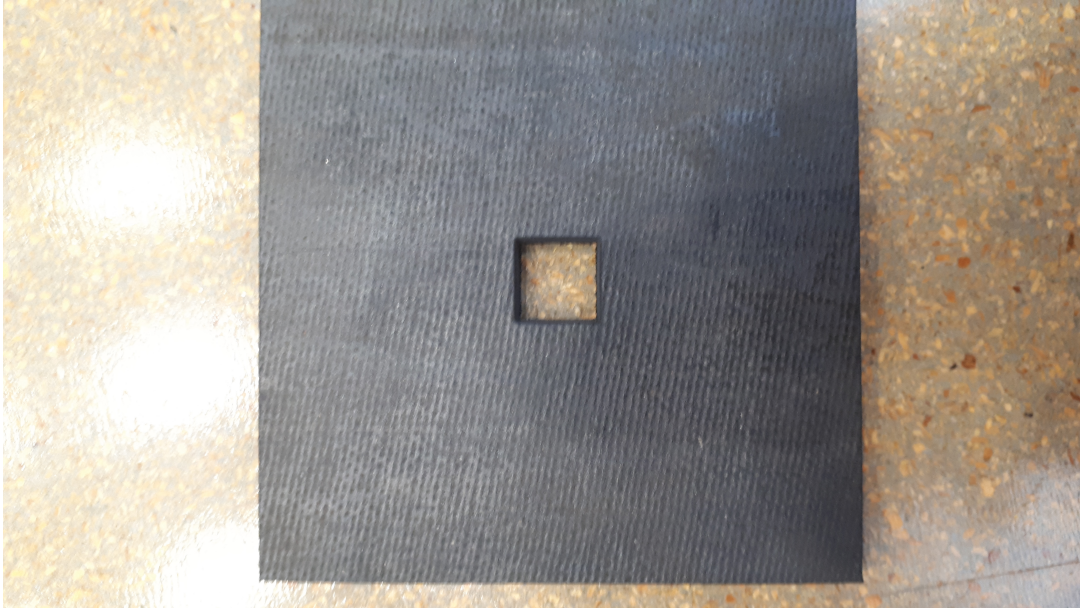


Figure 12: Here the $10\text{ mm}\times 10\text{ mm}$ screen can be seen.

5.2.1 Screens

It is important to state the difficulty of finding and characterising the neutron beam. It can only be done by moving a screen and conducting a measurement at each position. In theory it should be possible to move the analyser crystal in peak position after which the screen gets moved. But the stability of the USANS instrument disallows this approach. Therefore, the analyser crystal had to be rotated each time the screen position changed.

After the re-installation of the detector a quick measurement was done and the tilt angle with the maximum neutron peak was used for the following measurements. The same screen was used as before and the sample holder was moved. The horizontal starting point with 327 089 counts as well as the vertically point with $-700\,022$ counts were labelled as reference points for the sake of convenience. The vertically position was then fixed while the screen was moved horizontally from -30 mm to 20 mm relative to the starting point. Each 10 mm step a quick measurement was done. After that it was moved back to the starting point and the vertical axis was moved. This time only two measurements were done at the position 10 mm and -10 mm. The problem was that the sample holder had reached its vertical limit at -10 mm but was still beneath the neutron beam. To fix this, a 35 mm thick plate was installed underneath the sample holder and its motors. Now the measurements were repeated with the same screen and the neutron beam finally passed through. Just like before the vertical position was fixed while the horizontal one was moved in 10 mm steps. The horizontal position (Y) with the highest neutron flux was then held while the vertical position (Z) was scanned in 10 mm steps. The rocking curve at the position with the highest intensity can be seen in figure 13.

The next day it seemed the crystal tilted. Therefore several quick measurements were done to find the new tilt angle with the highest neutron flux. The new position was at $\rho = 350$ counts compared to the old one at $\rho = -600$ counts which corresponds to 0.012° . This already indicated that the whole setup is very sensitive and especially the installation of a heavy plate on the optical bench can tilt the analyser crystal by accident. Though it is important to note that the measurement time of both measurements were only 10 seconds which can result in a high statistical error as the size of the error bars in figure 13 indicates.

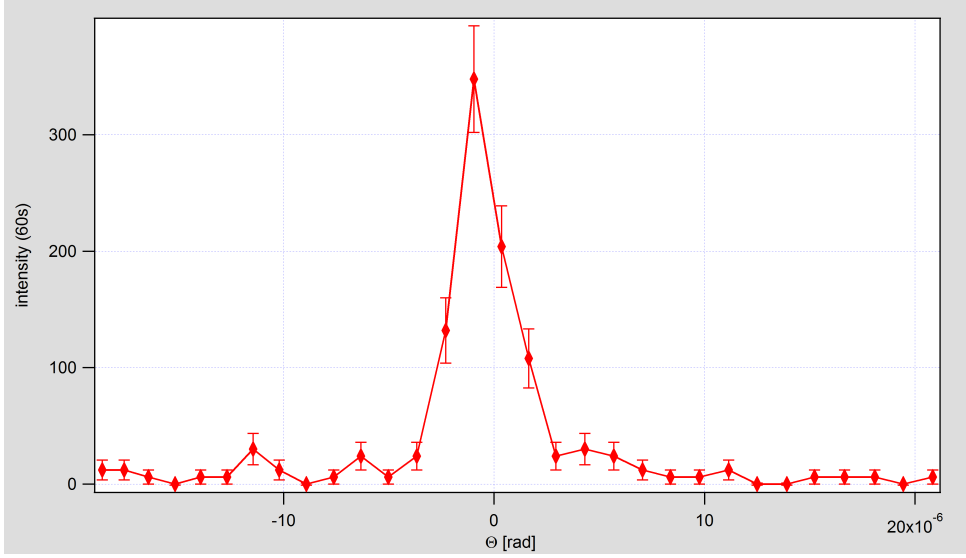


Figure 13: Rocking curve with the 10 mm \times 10 mm screen at position Y=0 mm and Z=0 mm.

5.2.2 Neutron monitor

The monitor is very essential for the whole setup since it is used as a reference point for the incoming neutron flux. It can detect a change of the total neutron flux independent of the analyser crystal position. This means that for example a decreasing power output of the reactor, as it would be the case with neutron poisoning, can be detected. Furthermore the lower neutron flux can be compensated by scaling the measured neutron counts of the detector to that of the monitor.

But first the monitor had to be calibrated. This was done by placing it near a Pu-Be laboratory neutron source and measuring a pulse height spectrum overnight. Afterwards the spectrum was analysed and a lower neutron detection threshold was set accordingly. This threshold has the purpose that only events with large pulse heights, which are more likely to be neutrons, give rise to a logical signal which is transmitted to the counting electronics and interpreted as a neutron event there. A heavy aluminium plate on which later the neutron monitor was installed, was mounted between the sample holder and the monochromator.

Also the vertical position of the monitor plays an important role. It must not only be installed inside of the neutron beam but also at a position where

it interferes as little as possible with the part of the beam which goes through the samples. Otherwise it could reduce the amount of neutrons significantly or induce a scattering pattern independent of the sample. It was then connected to a preamplifier which in turn was connected to an oscilloscope and the PC. The receiving signal was distorted and it could only be resolved by adding a $50\ \Omega$ terminating resistor. Although it was already calibrated with the Pu-Be laboratory neutron source, the pulse height spectrum was measured once again but this time with the reactor as the neutron source. This is important because on the one side, the neutron spectrum does not only differ compared to the laboratory neutron source. The Pu-Be neutron source emits fast and thermal neutrons while the neutron beam of the USANS instrument consists almost solely of thermal neutrons. On the other side, the background distribution is different as well. The gain of the preamplifier was then adjusted to obtain a better signal which in turn was used to determine the threshold. The pulse height spectrum can be seen in figure 15. The threshold was set so that all events above channel 420 are counted. The voltage of this can be calculated as follows. The monitor delivers an amplified analogue signal with a peak voltage below 1 V. The input range 0 V to 1 V is split into 2048 channels. This means that the voltage of channel 420 is $\frac{420}{2048}\text{ V} = 0.205\text{ V}$ at which the threshold was set.

After the monitor was calibrated, several quick measurements were done. Again it seemed that the tilt angle ρ changed by 700 counts or 0.09° . This was probably due to the heavy plate which was installed before. As soon as the monitor was calibrated it was installed between the sample holder and the monochromator. This setup can be seen in figure 14.

5.2.3 Measurements

With the improved hardware, especially the possibility to normalise the neutron beam with the newly calibrated monitor, several measurements from before were repeated. At first the same screen as before was used and several measurements at different positions were done followed by measurements with a larger screen of 4 cm^2 ($20\text{ mm} \times 20\text{ mm}$). A good comparison between these measurement results is not possible since the measurement time for each point was too low for the given neutron intensity.



Figure 14: Installation of the incoming neutron monitor. The monitor is on the right side attached to a red cable. The sample holder with a screen is in the middle and on the left side the analyser can be seen.

Therefore, for the next measurement an even larger $25 \text{ mm} \times 25 \text{ mm}$ screen and a $30 \text{ mm} \times 30 \text{ mm}$ one was used. Furthermore each screen was measured at the same position and the peak intensity of each screen is given in table 6 and 7.

Screen \ Y [mm]	-20	-10	0	10	20
25 mm \times 25 mm	396	1164	1530	1116	354
30 mm \times 30 mm	678	1428	2220	1668	630

Table 6: Peak intensity in cts/min at different horizontal (Y) positions of two different screens

This way a good comparison between the screens is possible. The results already indicate that the size of the neutron beam is larger than 6.25 cm^2 but the intensity with the 9 cm^2 screen seems to be close to its maximum.

In the next step a measurement at the origin point for each screen was done. The goal was to further investigate the dependence of the neutron flux on the area of the screen. For this the 6.25 cm^2 ($25 \text{ mm} \times 25 \text{ mm}$) screen was also measured. In figure 16 the measuring points as well as the corresponding fit,

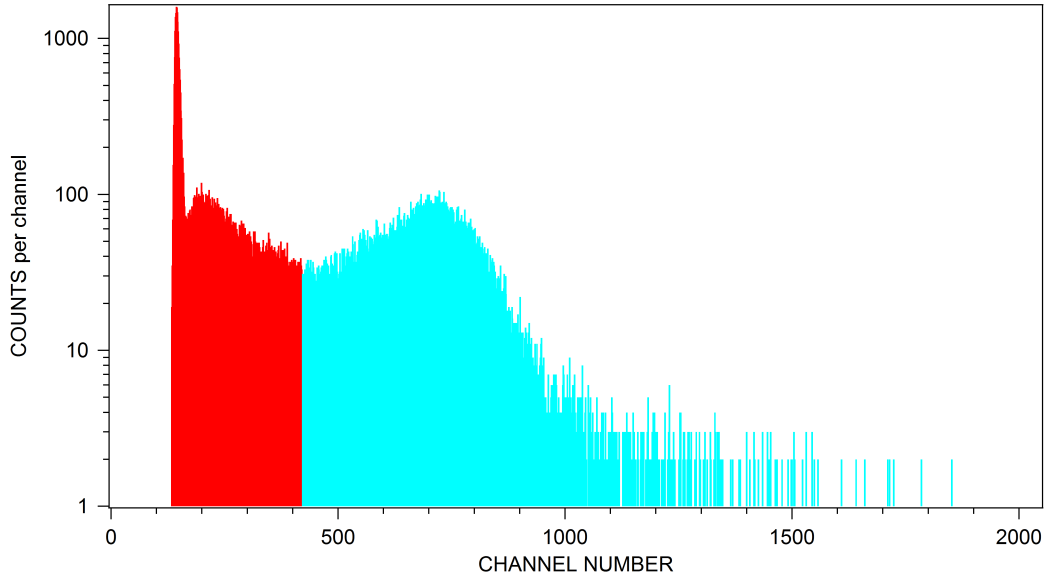


Figure 15: This figure shows the the pulse height spectrum of the monitor obtained at the USANS beam line after the monochromator. The neutron events start already at channel 150 but because of the high background events they can not be distinguished. Therefore the threshold at which events are counted as neutrons is set to channel 420 and are coloured in cyan.

Screen \ Z [mm]	-20	-10	0	10	20
25 mm \times 25 mm	342	1116	1530	1074	330
30 mm \times 30 mm	522	1266	2220	1332	396

Table 7: Peak intensity in cts/min at different vertical (Z) positions of two different screens

which was already discussed in section 4.2.5, for each of these screens are given. The fitted peak intensity for these screens as well as the intensity per area are also given in table 8. It can be seen that although the intensity increased with the screen size, the intensity per area decreased. This indicated that the neutron beam is inhomogeneous.

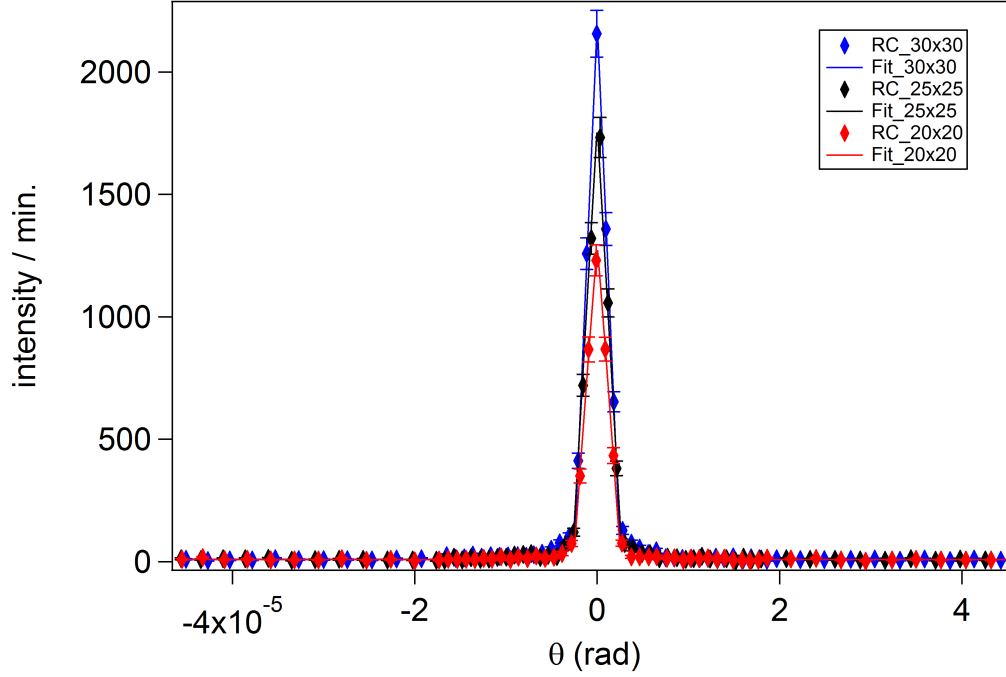


Figure 16: The rocking curves as well as the corresponding fit for the different screen sizes. Each of these peak measurements were done at the same position $Y = 0$ mm, $Z = 0$ mm and $\rho = 1150$ cts.

Screen	Peak intensity [cts /min]	Background [cts /min]	Screen area [cm ²]	Intensity per area [cts/(cm ² min)]
20x20	1284(50)	8.36(50)	4	321.0(125)
25x25	1773(51)	8.90(57)	6.25	283.7(82)
30x30	2195(70)	9.49(57)	9	243.9(78)

Table 8: The peak intensity as well as the intensity per area and other parameter for three different screen sizes.

5.2.4 Detector position

In this subsection the question occurred if the maximum intensity or the ratio of peak intensity to background intensity could be increased. The higher the intensity is the quicker a measurement can be completed. Therefore, more measurements can be done at one day. A low background intensity can also result in a shorter measurement time at large scattering angles. Furthermore,

smaller scattering signals of the sample can be discriminated from the background intensity. One possible way to increase the peak intensity is moving the detector closer to the analyser crystal. Though this might also lead to a higher background intensity. Moving it further away from the analyser decreases the peak intensity but also the background intensity. To see if there is an optimal detector position it was moved relative to the analyser crystal to four different positions. At each one a measurement was done which was then analysed with the program IGOR, which was already mentioned in section 4.2.5. In figure 17 the four different measurements as well as the corresponding fits are given. It clearly shows that the assumption from before, the closer the detector and analyser crystal are the higher the intensity becomes, is valid. Though as already mentioned, the background intensity plays also an important role. Therefore the peak intensity as well as the background and the ratio of these two parameters are given in table 9. The higher the ratio is the better. Hence, the detector was moved back to its original position at 67 cm from the analyser.

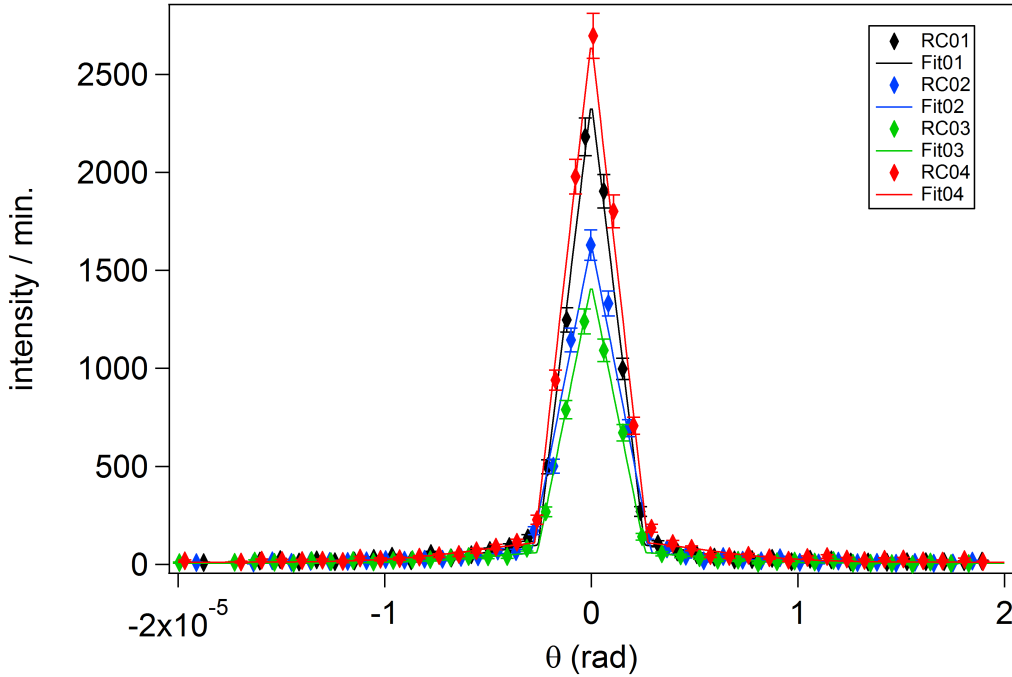


Figure 17: The rocking curves as well as the corresponding fit for the different detector positions. Each of these peak measurements were done at the same position $Y = 0$ mm, $Z = 0$ mm and $\rho = 1150$ cts. The fitting results as well as the distance to the analyser crystal are given in table 9.

Name	Distance from analyser [cm]	Peak intensity [cts /min]	Background [cts /min]	Ratio of peak to background
RC04	35.4	2670(70)	10.99(66)	243(21)
RC01	67.0	2358(65)	9.27(58)	254(23)
RC02	124.9	1628(23)	8.31(57)	196(16)
RC03	168.7	1424(45)	5.73(47)	249(28)

Table 9: The different detector positions as well as the peak intensity, background and ratio of these two parameters.

5.2.5 Angle measurement

It was observed that on most measurements the peak position, as determined by our RON angle encoder, changed. Sometimes the rotation angle θ only changed slightly but sometimes it jumped by a few μm piezo positions from one day to another. To investigate its cause an angle measurement was done. For this the analyser crystal was moved into the peak position, such that a high count rate of neutrons could be observed. Then the measurement started and was left alone for several days. During the measurement the piezo position and the RON position were obtained every minute. For this measurement a total of 5000 points were recorded. Since a movement of the RON position was observable another measurement was started - this time with 2000 measuring points. During this measurement the DC motor was also disconnected to make sure that this was not the cause for an unintentional movement. Since it was a mechanical disconnection a jump of the RON position occurred during the measurement. In figure 18 and 19 two angle measurements are plotted over the time. Since it was assumed that the angle changes because of the temperature, the ambient temperature in the reactor hall is also plotted in these figures. It can clearly be seen that there is a correlation between the change of angle and change of temperature. Both seem to show the same periodic properties of increasing and decreasing. The increase always starts at the morning when the reactor hall is heated by the rising sun and it decreases in the evening. The temperature information was taken from a weather station inside the hall near to the experiment.

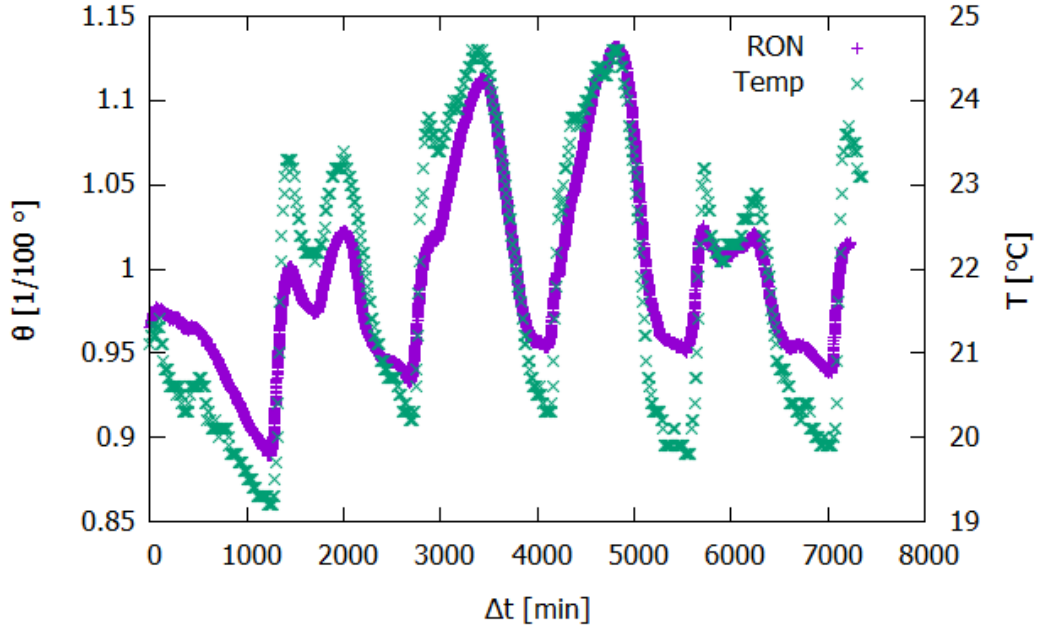


Figure 18: Rotation angle θ (purple) as well as temperature (cyan) plotted over time. This measurement was taken from the 27th of April to the 2nd of May 2018.

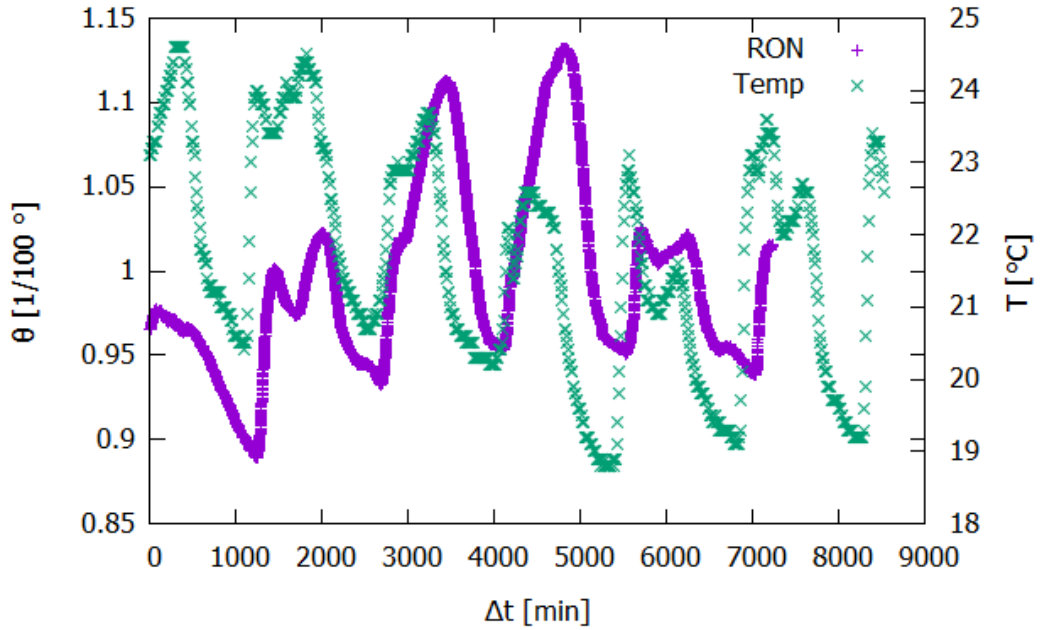


Figure 19: Rotation angle θ (purple) as well as temperature (cyan) plotted over time. This measurement was taken from the 2nd of May to the 8th of May 2018. The DC actuator for analyser crystal rotation was disconnected from its power supply to exclude possible unintentional effects.

5.2.6 Rocking curve with tilting

As already mentioned before, the analyser crystal can not only be rotated but also tilted. Until now in this work only quick measurements were done at different tilt angles to find the one with the highest intensity. So the next step was doing a series of longer measurements at different tilt angles ρ to see how exactly the intensity and the width of the rocking curve changes. First the starting point for ρ was set near the maximum intensity. It was then changed in one direction so that the peak intensity increased until it went over the tip and started to decrease. This was continued until the peak intensity was significantly lower compared to the starting point. The full width half maximum (FWHM) increased drastically. Also the larger the FWHM is the larger the peak measurement ranges have to be and together with the reduced intensity the longer each measurement takes.

All these measurements took place over several days. To take an accidental tilting of the setup into account, which would change the neutron intensity, the last measurement of each day was repeated in the morning of the next day. Also important to mention is that during two measurement days the reactor had to decrease its power output by 10% which in turn decreased the neutron flux. Both days a measurement was conducted and the change of power was observable due to the monitor. Though, as already mentioned in section 5.2.2, with the help of the monitor the measured neutron intensity by the BF_3 detector can be normalised to the counts of the ^3He one. This means that a slight change of neutron intensity can be compensated and there was no need to repeat the whole measurement. In total 25 measurements with 22 different tilt angles were made. Two of these results are given in figure 20. The rocking curve at $\rho = 1950$ counts had the highest peak intensity of this measurement series while the peak intensity at $\rho = 6150$ counts, a difference of 0.055° , was on the lower end.

For an overview the peak intensity as well as FWHM for each of these 22 measurements are plotted over the tilt angle in figure 21. It can clearly be seen that with a decreasing peak intensity the FWHM increases.

5.2.7 Lattice measurement

In this section further characterisation of the neutron beam took place. Especially the wavelength but also the diffraction angle were of interest. Therefore,

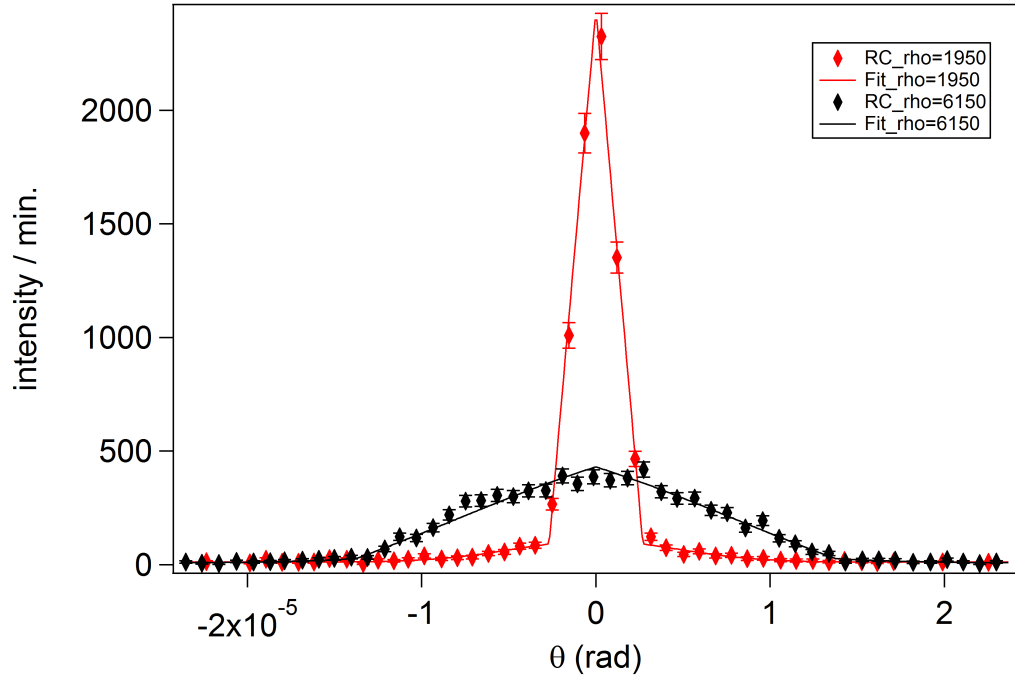


Figure 20: The rocking curve at $\rho = 1950$ counts (red) and at $\rho = 6150$ counts (black), a difference of 0.055° , are given.

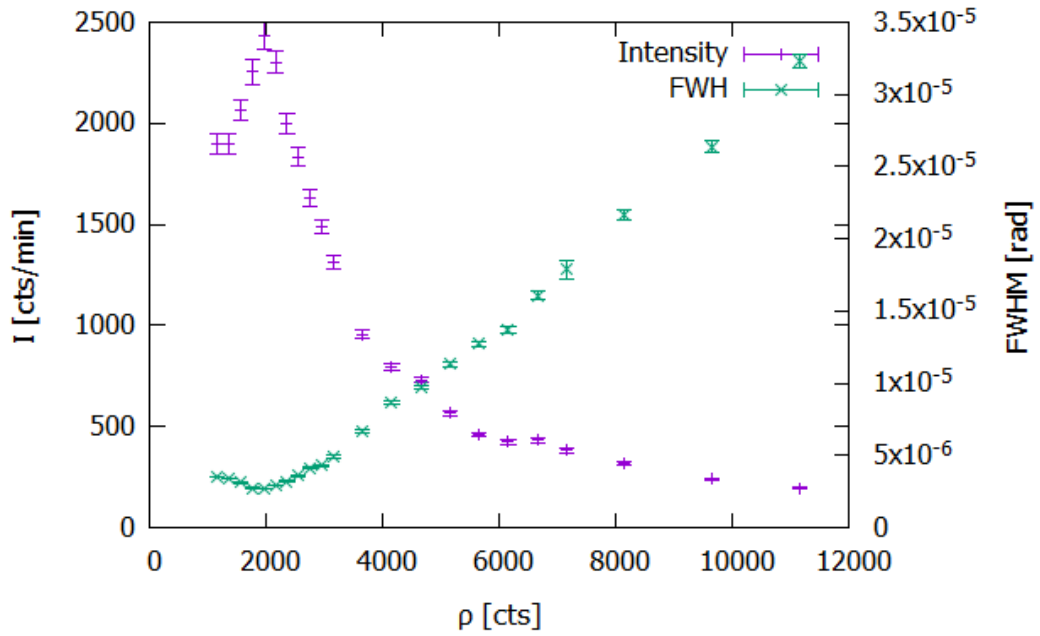


Figure 21: Fitted peak intensity and FWHM for each of the 22 measurements in dependence of the tilt angle ρ .

the first measurements of silicon lattices were conducted. Furthermore, since the tilt angle ρ of the analyser was moved drastically in the previous subsection, a re-calibration of the instrument had to be done. During this a cadmium plate was placed on both sides of the analyser crystal to hopefully decrease the background intensity. After the tilt angle ρ with the highest neutron intensity was found, the first lattice with an unknown lattice constant was placed in the sample holder. It was believed that the lattice constant is $20\text{ }\mu\text{m}$. Several long measurements were made. In figure 22 the rocking curve of the lattice is given. A diffraction pattern is observable and especially the first order maxima are clearly visible. It can also be seen that the maxima on the right side of the central peak is smaller than on the left side. This means that the sample holder is not perfectly aligned perpendicular to the neutron beam. The lattice should be orthogonal to the neutron beam to obtain diffraction maxima of equal intensity for positive and negative q -values [36]. The sample holder was then rotated, via the M-037.DG rotation stage, by 100 000 counts corresponding to 1.32° and the measurement was repeated. The rocking curve of this new position is given in figure 23. Now the peak on the right side of the central one was higher than the left one. So the measurement was repeated at an angle of 50 000 counts. As can be seen in figure 24 both first order maxima now have the same height.

Figure 24 was then fitted with the program IGOR. For this the believed lattice constant of $20\text{ }\mu\text{m}$ was used. The fitted plot is given in figure 25. There the measuring points, the fit of the lattice curve as well as the peak location can be seen. With the fit and the lattice constant the wavelength of the neutron beam was calculated.

The problem with this result was that it differed compared to the wavelength calculated via the Bragg equation (85). This meant that either the lattice had a different lattice constant or the angle measured by RON is too small. Therefore another lattice was measured from which the lattice constant was known to be $20\text{ }\mu\text{m}$ from previous experiment [37]. For better comparison the measurement was done with the same parameters as before. The measuring points as well as the fit of the lattice curve and peak locations are given in figure 26.

For comparison the wavelength λ obtained from both lattice fits as well as the peak distance can be seen in table 10.

The results for the two lattices in table 10 are very similar. From this it can be concluded that the first lattice indeed had the same lattice constant. This

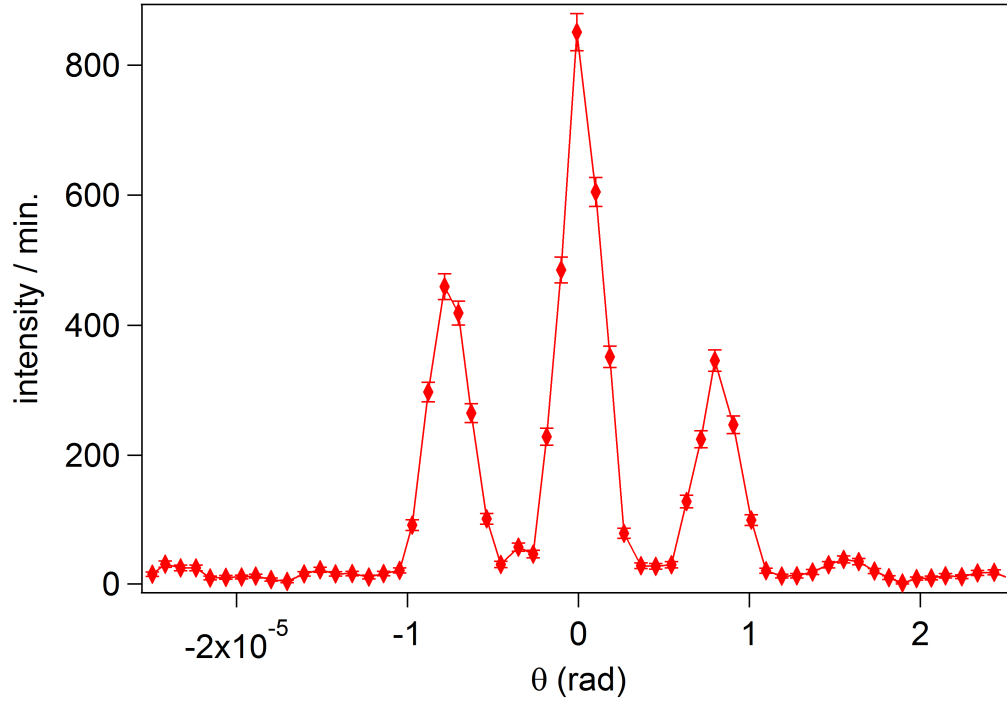


Figure 22: Rocking curve of a 20 μm lattice at M-037.DG= 0 counts.

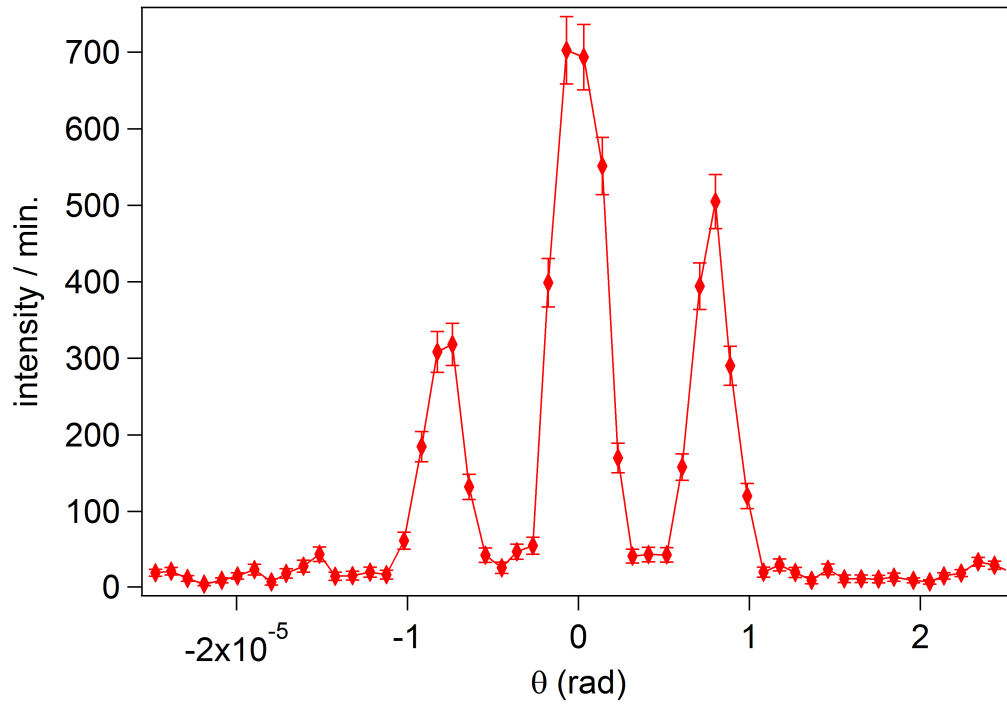


Figure 23: Rocking curve of a 20 μm lattice at M-037.DG= 100000 counts corresponding to 1.32°.

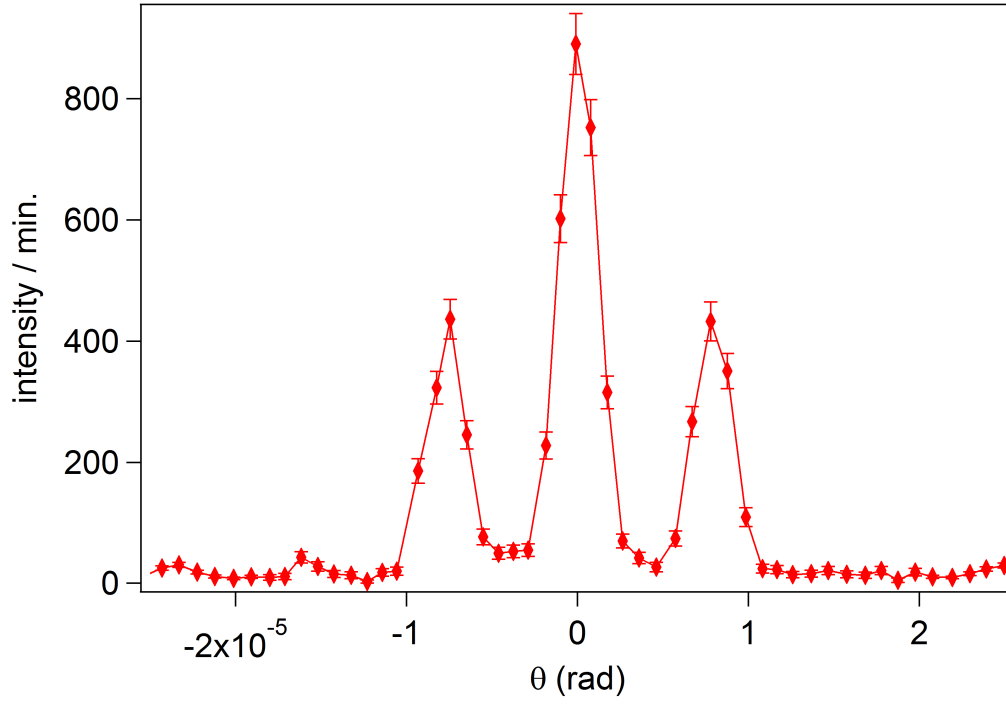


Figure 24: Rocking curve of a 20 μm lattice at M-037.DG= 50000 cts or 0.66° .

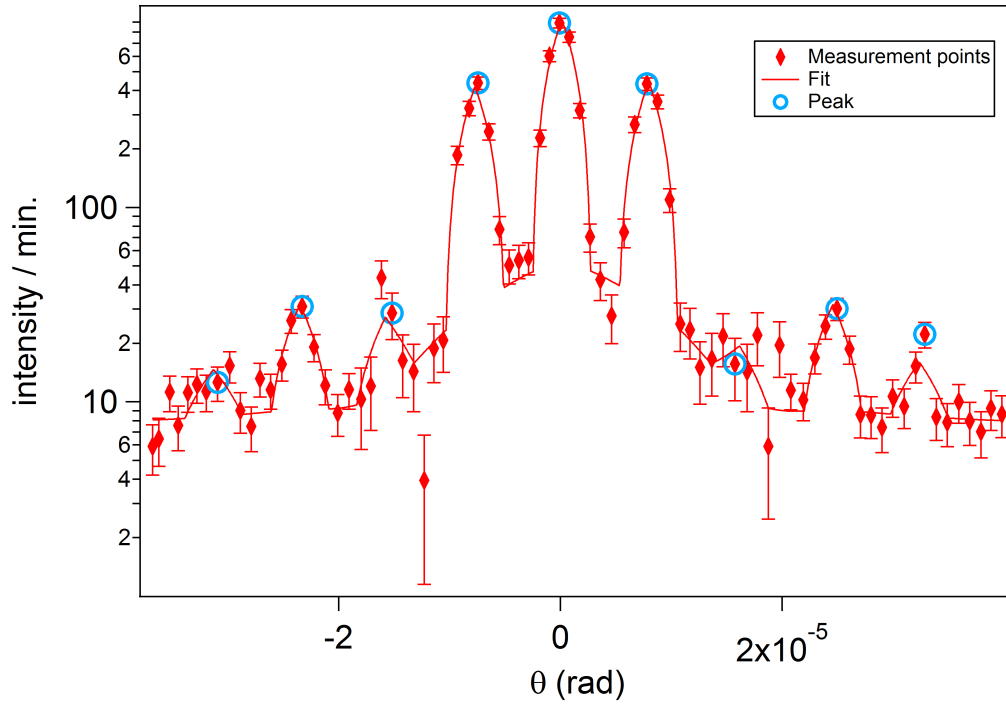


Figure 25: The measuring points as well as the fit and the peak location from the third measurement of the lattice with a presumed lattice constant of 20 μm are plotted. For better visibility of the peaks the counts/min are given in a logarithmic scale. The obtained wavelength λ is given in table 10.

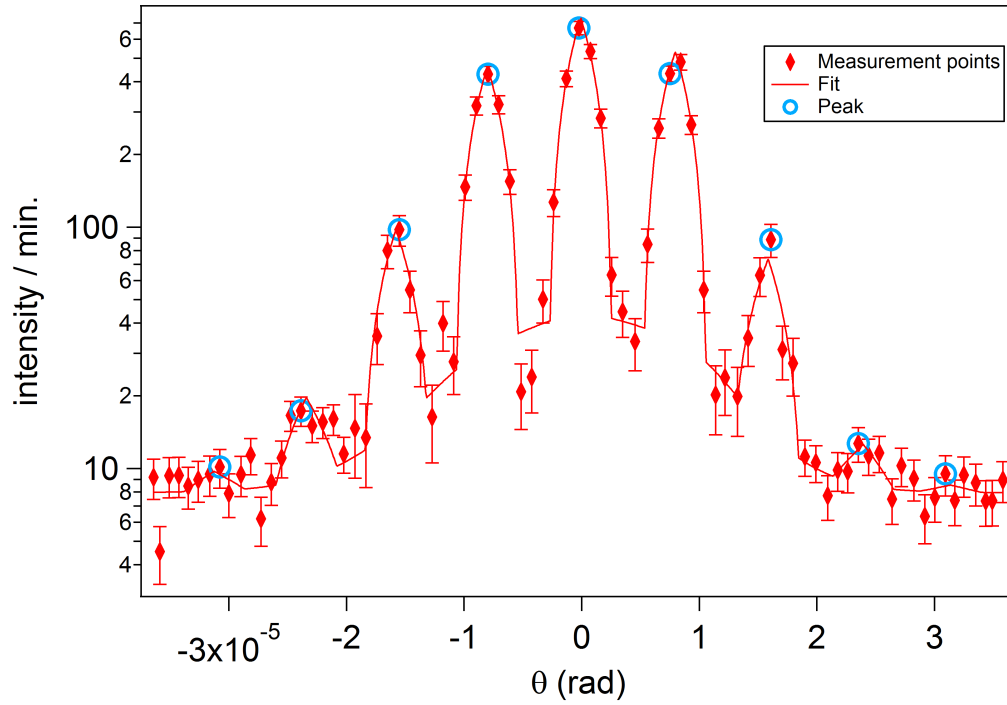


Figure 26: The measuring points as well as the fit and the peak location from the second lattice are plotted. This lattice has a known lattice constant of $20 \mu\text{m}$. For better visibility of the peaks the counts/min are given in a logarithmic scale. The obtained wavelength λ is given in table 10.

probably also meant that the big wavelength discrepancies must come from the angle measurement device. In a later section 5.5.5 further lattices will be discussed to see if this deviation is persistent.

	$\lambda [\text{\AA}]$	Peak distance [μrad]	Ratio of λ_l/λ_B
First lattice	1.590(5)	7.948(24)	0.903(3)
Second lattice	1.589(5)	7.944(24)	0.903(3)

Table 10: Here the fitted wavelength λ of the neutron beam as well as the peak distance is given for both lattices.

5.2.8 Background

As mentioned in the preceding section, cadmium was placed around the crystal analyser to reduce the background. For the background identification measure-

ments were done with an acquisition time of at least 60 seconds per point outside the peak centre of the rocking curve. The background could then be acquired by fitting the resulting data.

In figure 27 the rocking curve before the cadmium was placed as well as after is given. It is important to note that although both measurements were conducted at a different tilt angle ρ the FWHM is about the same and therefore also the peak intensity. This is important for a direct comparison.

The fitted results of both measurements are given in table 11. It can clearly be seen that although the peak intensity decreased slightly, which is probably just a statistical outlier, the ratio of peak intensity to background increased drastically.

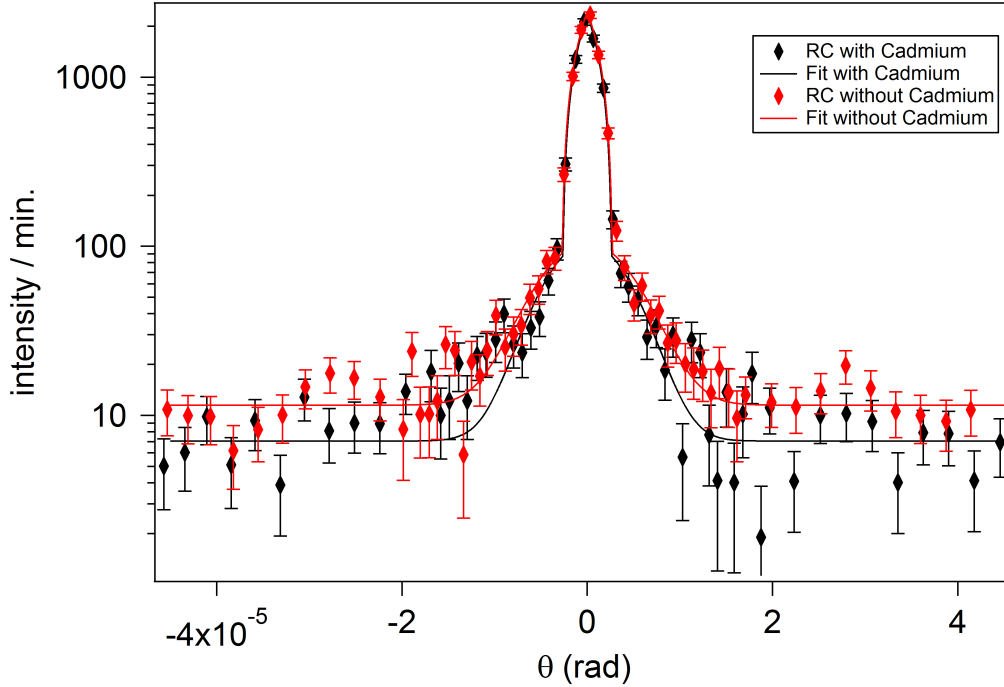


Figure 27: Comparison of rocking curves (RC) before and after cadmium was placed behind the analyser crystal. In red the RC without cadmium is given. This was done at $\rho = 1950$ counts. In black the RC with cadmium is given. This measurement was done at $\rho = 2350$ counts. All other measurement parameters were exactly the same.

It is important to note that the FWHM was slightly lower than the calculated one from equation (78). This was a further indication that the angle

	Peak intensity [cts /min]	FWHM [μ rad]	Background [cts /min]	Ratio of peak to background
With cadmium	2335(69)	2.612(47)	7.1(5)	331(34)
Without cadmium	2430(66)	2.692(32)	11.5(7)	211(18)

Table 11: Here some of the results for the measurement with and without cadmium are given. Especially the ratio of peak to background is of interest.

measurement device RON did not measure correctly. More on this in section 5.5.5 where several lattices were measured to investigate this discrepancy.

The next step was to investigate if the background can be reduced further. For this the 30 mm \times 30 mm screen which was used before, was mounted on the collimator with adhesive pads. The earlier measurements indicated that the neutron beam has about the same area as this screen and therefore the peak intensity near the centre should not change much. But since the collimator is wider then this screen it was hoped that some of the background intensity will be reduced. For the first measurement the screen was fixed as centred as possible. Then it was moved to the top and later to the bottom. Both times it was aligned with the inner edge of the collimator. For further investigation a circular screen with 40 mm diameter was also used and placed centred. In figure 28 the measuring points as well as the fits of these measurements are given. For better comparison we zoom into the centre of the peak. In figure 29 the plot over the whole range can be seen. This time only the fits are plotted because the measuring points would be too cramped. Furthermore the y-axis is set to a logarithmic scale. The results to each of these measurements are given in table 12.

The results indicate that the circular screen had the best peak intensity to background ratio but all the results are within margin of error. Especially the background on the first measurement without any screen was larger than on the day before (table 11) although the measurement parameters did not change. To decrease statistical error for the next measurements, the measurement parameters were adjusted. There are now three sectors to the left and to the right of the peak position compared to the two before. Each one with a greatly increased measuring time. That way the background statistics improved drastically. The total measurement time of the RC with the old parameters was 40 minutes com-

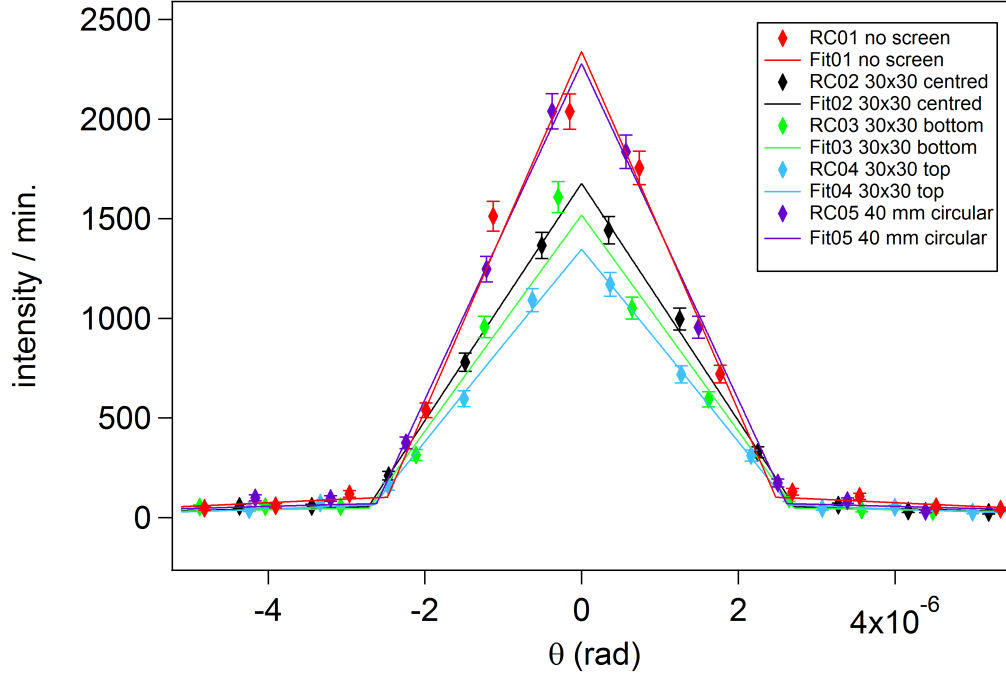


Figure 28: Comparison of the peak intensity of the measurement with different screens in front of the collimator.

Name	Screen	Position on collimator	Peak intensity [cts /min]	Background [cts /min]	Ratio of peak to background
RC01	no screen		2332(73)	8.4(5)	228(25)
RC02	30×30	centred	1673(49)	5.3(4)	316(33)
RC03	30×30	bottom	1514(45)	5.0(4)	303(33)
RC04	30×30	top	1342(44)	5.0(4)	268(30)
RC05	40 mm circular	centred	2274(61)	6.8(5)	334(34)

Table 12: The fitting results of the rocking curves with and without screen are given. Especially the peak to background ratio is of interest. The 30×30 screen are square screens with length of 30 mm in both dimensions. The other screen is a circular one with 40 mm diameter.

pared to 122 minutes with the new parameters. It would also have been possible to just increase the overall measurement time but this would also have meant an even longer total measurement. The old and new parameters are given in table 13.

The first measurement with the new parameter set was a simple rocking

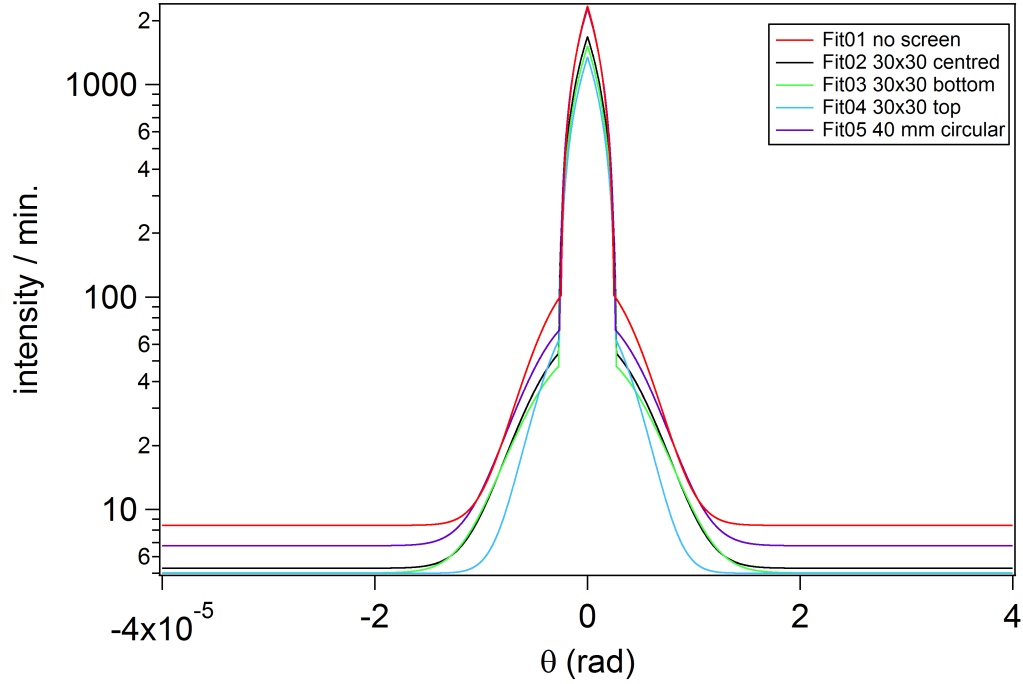


Figure 29: Comparison of the peak intensity as well as the background of the different measurements. For better visibility the measuring points were left out.

	Old parameters		New parameters		
Piezo range [μm]	± 3.4	± 1.4	± 5.35	± 1.15	± 0.35
Step size [μm]	0.2	0.07	0.7	0.2	0.07
Measurement time per point [s]	60	30	480	120	60

Table 13: The old and new measurement parameters for comparison. Especially the measurement time per point as well as the total range of the measurement were increased. The possibility of different parameters for different ranges was already mentioned in section 4.2.3 [38].

curve without any screens attached. Then to see if further improvements of the peak intensity would be possible by changing the detector position normal to the neutron beam, one half of the collimator was covered while a peak measurement took place. Then the other side was covered and the measurement was repeated. If the detector was positioned ideal both measurement should have had about the same intensity and background. In figure 30 the rocking curves of these three measurements can be seen. It is clearly visible that covering the left side

of the collimator (looking towards the neutron beam) the intensity was quite a bit lower than covering the right side. So further improvements were expected by moving the detector slightly orthogonal to the neutron beam. But before that another two measurements were done. On the first one the bottom half of the collimator was covered and on the second one the top half. This can be seen in figure 31. For better comparison the rocking curve without a screen is also given. All the fitted results of these measurements are also in table 14.

Covered side	Peak intensity [cts /min]	Background [cts /min]	Ratio of peak to background
none	2320(43)	8.1(3)	286(16)
left	864(23)	5.7(2)	152(9)
right	1553(38)	5.4(3)	288(23)
bottom	1018(23)	5.6(3)	182(14)
top	1258(29)	6.5(3)	194(13)

Table 14: The fitting results of the rocking curves with and without covered sides.

Since the last measurement indicated that the neutron beam was not perfectly aligned with the collimator and therefore with the detector, the detector was moved. But first several measurements at different tilt angles were done to ensure the best tilt angle with the highest intensity. The barrel with the detector inside can be moved normal to the neutron beam by turning two screws which are under the barrel. On each screw a line was drawn to count the revolutions. To prevent a twist the right screw was only rotated three times following with three turns of the left screws. This was repeated for a total of 18 revolutions which meant approximately 5 mm movement orthogonal to the neutron beam. These turns were done clockwise which made the detector move to the left if one looks towards the neutron beam. While moving the detector a problem occurred with the collimator. It was not attached to the detector and therefore did not move with it. So the next couple of measurements had to be done without it. This should not change the peak intensity near the centre but very well the background. Therefore the range of the peak measurements were adjusted accordingly, that only a small region near the centre was measured. This way the measurements did not take long but provided good statistics for the peak

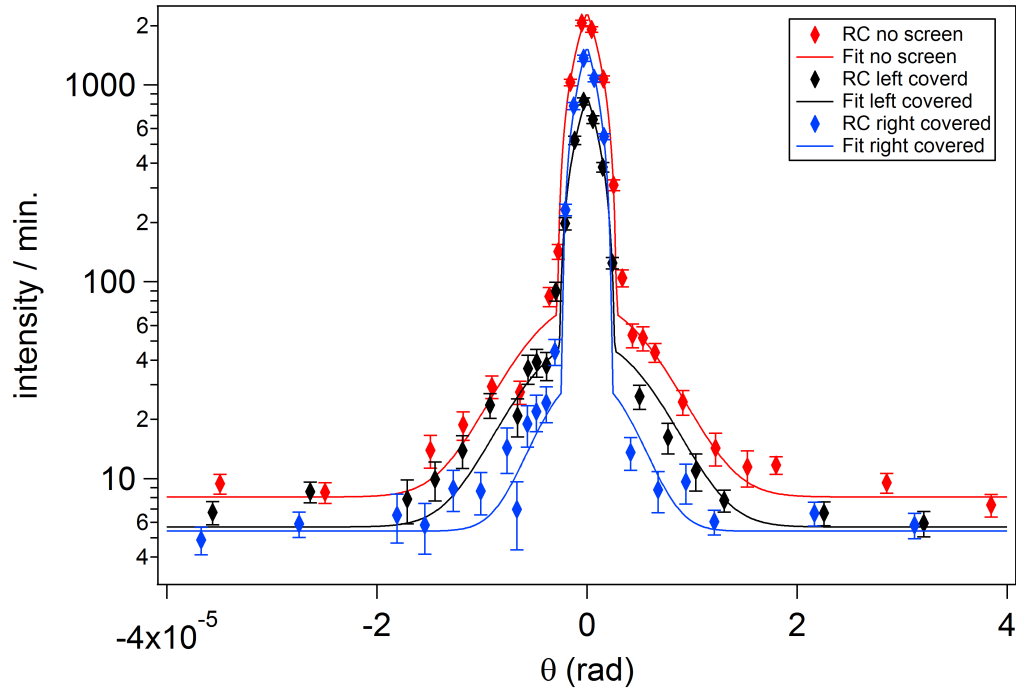


Figure 30: The rocking curve without screen as well the ones with the left\right side of the collimator covered.

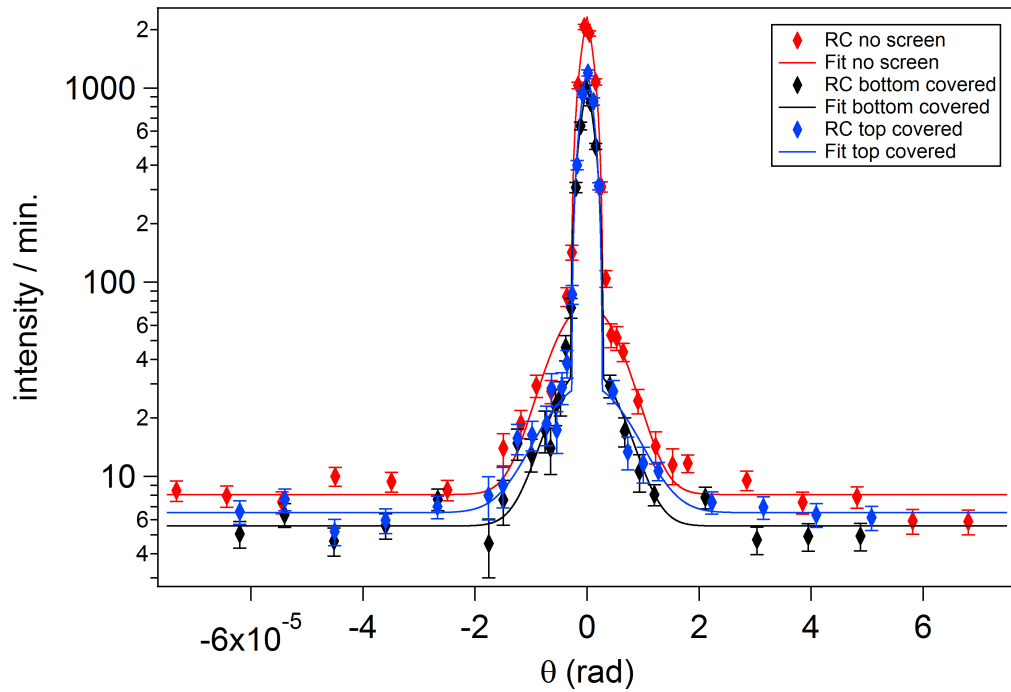


Figure 31: The rocking curve without screen as well the ones with the top\bottom side of the collimator covered.

intensity.

For the next measurements a total of nine revolutions were made, but this time counter clockwise. So the position was midway from the starting point and the last one. The measurement was then repeated and the detector was moved to the starting point. In total measurements at three different detector positions were done. One at 0 revolutions (origin), one at 9 revolutions and another one at 18 revolutions clockwise to the starting position. The rocking curves of these three positions are given in figure 32.

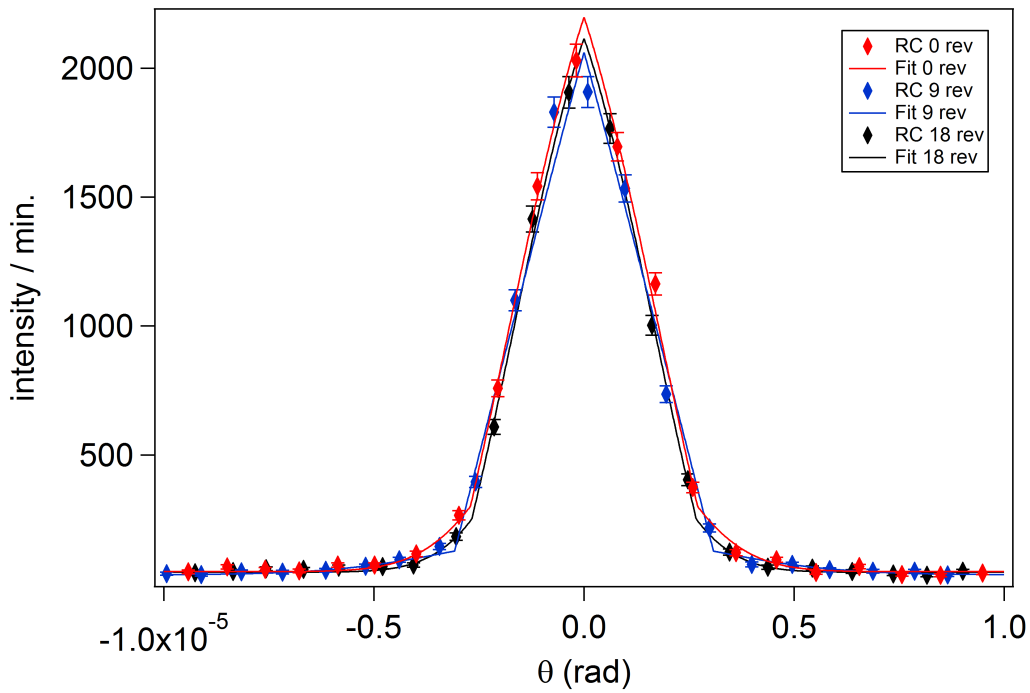


Figure 32: Here the rocking curves measured at three the different detector positions are given. The revolutions are counted clockwise from the origin (0 rev).

5.2.9 Modification of the collimator

The last few measurements indicated that the detector was moved in the wrong direction since the intensity decreased slightly. But before it was moved in the other direction the collimator had to be attached to the barrel so that they would move together. For this the whole detector setup was brought to the mechanical workshop. Furthermore borated polyethylene blocks which were

installed to likewise reduce the background were removed to make space for uninstalling the detector. The detector is placed inside a huge cylindrical borated paraffin barrel which again should shield for unnecessary background radiation. Since the barrel is extremely heavy, two people were needed to move it onto a rolling cart. Last but not least, the mounting mechanism for the barrel was detached as well. After a few days the modification was done and the collimator was now fixed at the barrel mounting mechanism. Therefore when the barrel is moved the collimator moves as well. Furthermore a sample holder was built to attach the screen on the collimator without the use of adhesive pads.

5.3 Improved setup

After the barrel, the detector, the collimator and the mounting device were re-installed, several measurements were performed. The first few measurements were done without additional shielding which can clearly be seen in the resulting background. The idea was to first position the crystal analyser at the best tilt angle which delivers the highest intensity. The rocking curves at the different tilt angles can be seen in figure 33.

It is important to mention that only the measuring points are given and no fit was done. Because of the high background, over an order of magnitude higher than before, the fit is inaccurate at the peak centre. Therefore the peak intensity can not be obtained reliable. So by looking at figure 33 the highest intensity was assumed at $\rho = 1850$ counts. This shows once more the importance of a low background intensity for an USANS measurement.

After that, the collimator was moved slightly and borated polyethylene shielding blocks were installed. After each measurement the shielding or the collimator was positioned slightly different compared to before. One big problem for the best intensity and background positioning is the large number of degrees of freedom for this procedure. The collimator can be moved and even twisted slightly. The shielding blocks can be positioned completely different. The barrel can be moved normal and parallel to the neutron beam. And last but not least the detector inside the barrel can also be moved parallel to the neutron beam. So for the next three measurements the collimator was positioned on the left side, right side and centred on the collimator mount. The results can be seen in figure 34.

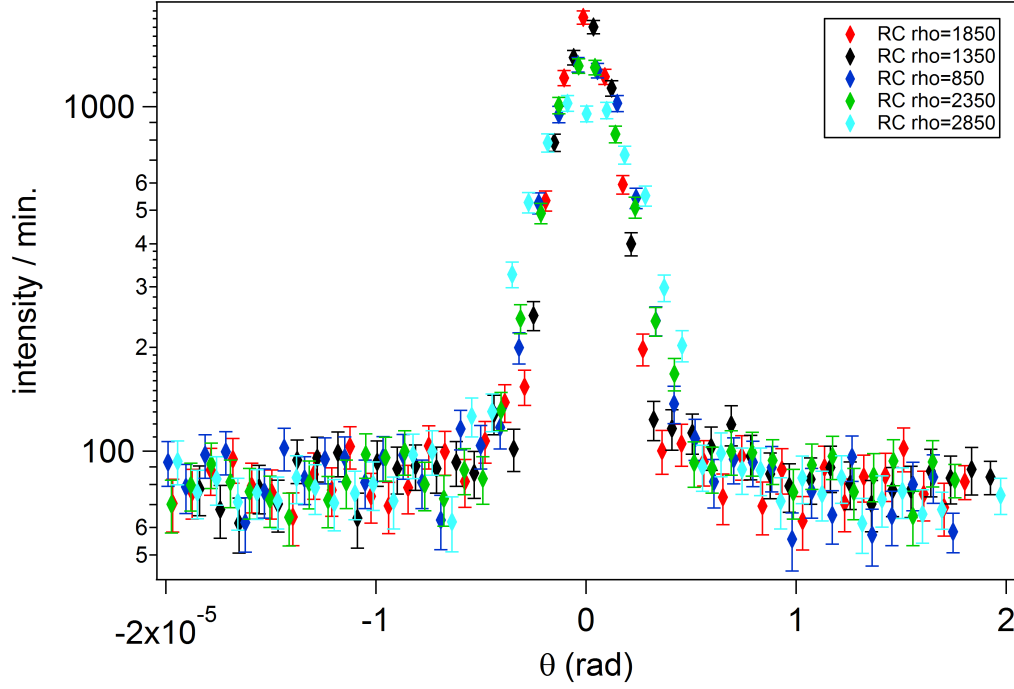


Figure 33: Rocking curves at different tilt angles ρ . Due to the lack of additional shielding the background intensity increased by an order of magnitude and an accurate fit was not possible.

With the shielding blocks the background intensity reduced a lot but the peak intensity was still low compared to the old setup. So now the detector setup was moved.

5.3.1 Barrel position

With the collimator attached to the barrel, the setup was moved slightly by turning the screws. Each time only a couple of revolutions were done. The detector was moved several times to several different positions. Some of these measurements can be seen in figure 35. The results indicate that on both ends of the range (15 revolutions and -45 revolutions) the intensity was at the lowest point. This means that the position with the highest intensity should be somewhere in between. However, the overall peak intensity measured was still lower than the old setup. A possible reason for this was that either the detector was still on a different position than before or the collimator was not positioned correctly. To rule the latter one out it was removed for the next measurements.

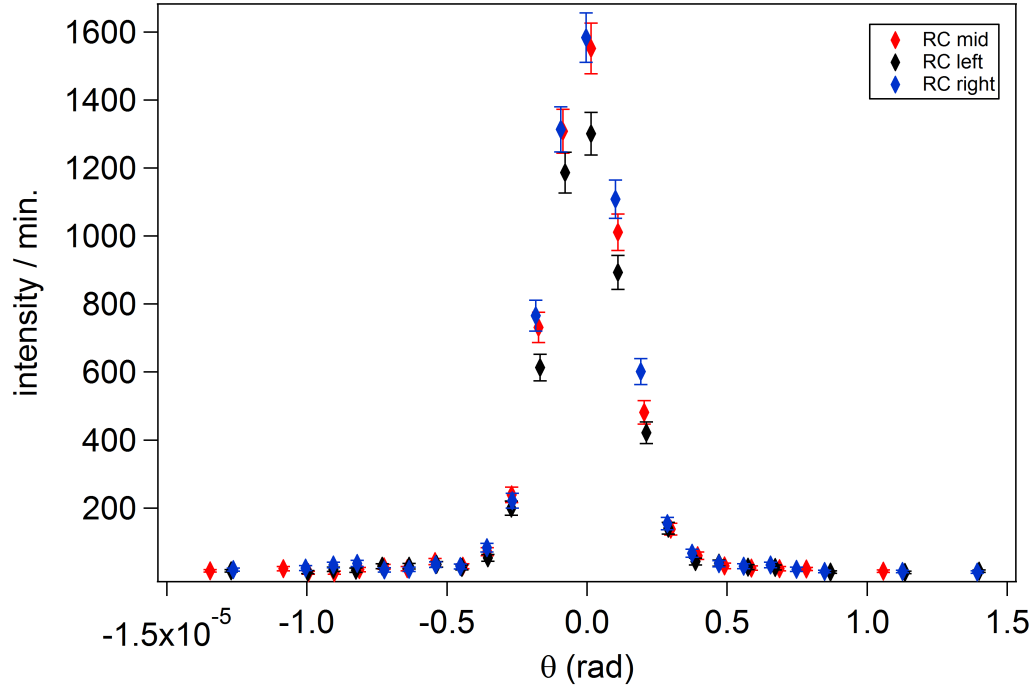


Figure 34: Rocking curves at different collimator positions.

A total of 46 measurements were done with a range of 50 revolutions anti clockwise to the starting position and 60 clock wise. But since the intensity of most of them is pretty similar only 6 measurements were selected and are given in figure 36.

But even without the collimator the intensity was still lower compared to the old setup. Therefore the detector inside the barrel was moved closer to the analyser crystal. Although this improved the peak intensity as can be seen in figure 37, the background was increased drastically. Consequently the detector was moved back to its old position.

Another possible reason for the lower intensity was that with the new setup the detector might also be rotated. Therefore a sole correction of the position orthogonal to the neutron beam would not be enough. But as already mentioned before, the barrel with the detector inside was not fixed but just placed on two different small plates. Each of these can be moved individually by a screw. One was on the front of the barrel while the other one was on the back. For the next few measurements only one of these screw was adjusted while the other one was fixed. Therefore the detector was rotated. At first the rear screw

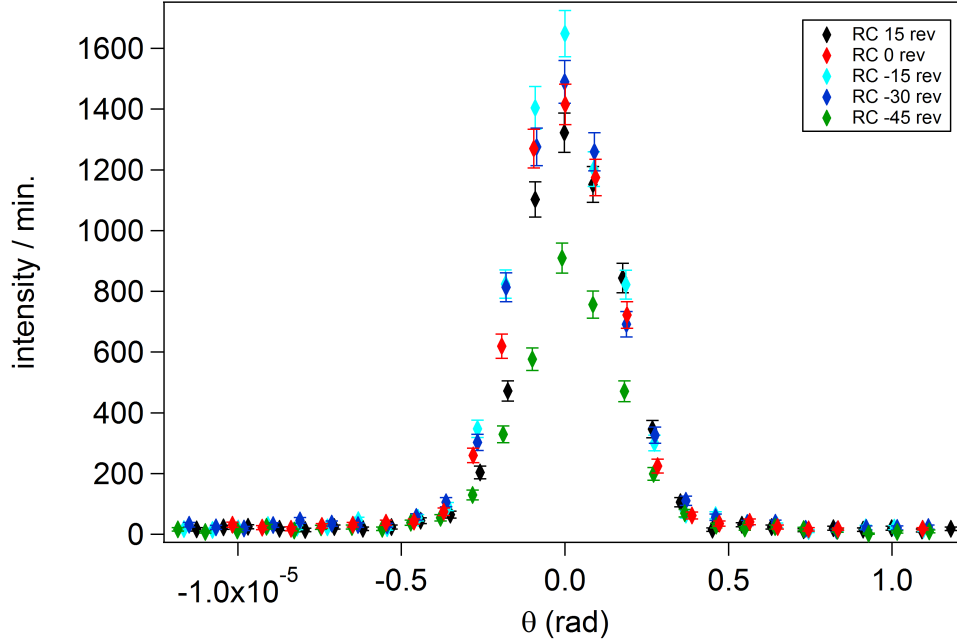


Figure 35: measuring points at different detector positions orthogonal to the neutron beam. The detector was moved via turning two screws. A positive revolution means the screw was turned clock wise, a negative anti clock wise.

was adjusted slightly but again no improvement was in sight. Therefore the number of revolutions was increased. At the end a total of 70 revolutions anti clockwise and 70 clockwise relative to the starting position were done. Some of these, especially the one with the highest intensity, are given in figure 38. The position with the highest intensity was then fixed while the front screw was adjusted. This time only 20 revolution clockwise and 20 anti clockwise were done. The results can be seen in figure 39.

Now the detector inside the barrel was moved again but only a couple centimetres. Although this should have changed the intensity only slightly there were significantly discrepancies between moving it forward and then backwards again.

The problem was that the detector cable was loose in the high voltage connector. While moving it further to the front of the barrel the cable was pushed to the detector which resulted in an improved electrical connection and a better signal. But as soon as it was moved back the cable was loosened again. After tightening the HV connection the intensity discrepancies were gone.

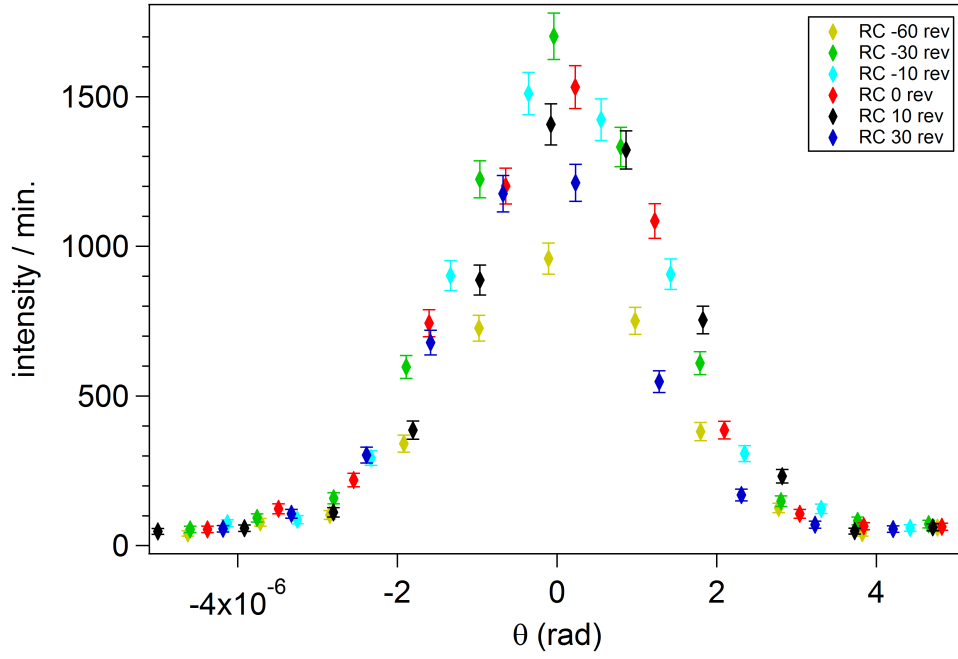


Figure 36: Measuring points at different detector positions orthogonal to the neutron beam with the collimator removed. The detector was moved via turning two screws. A positive revolution means the screw was turned clock wise, a negative anti clock wise.

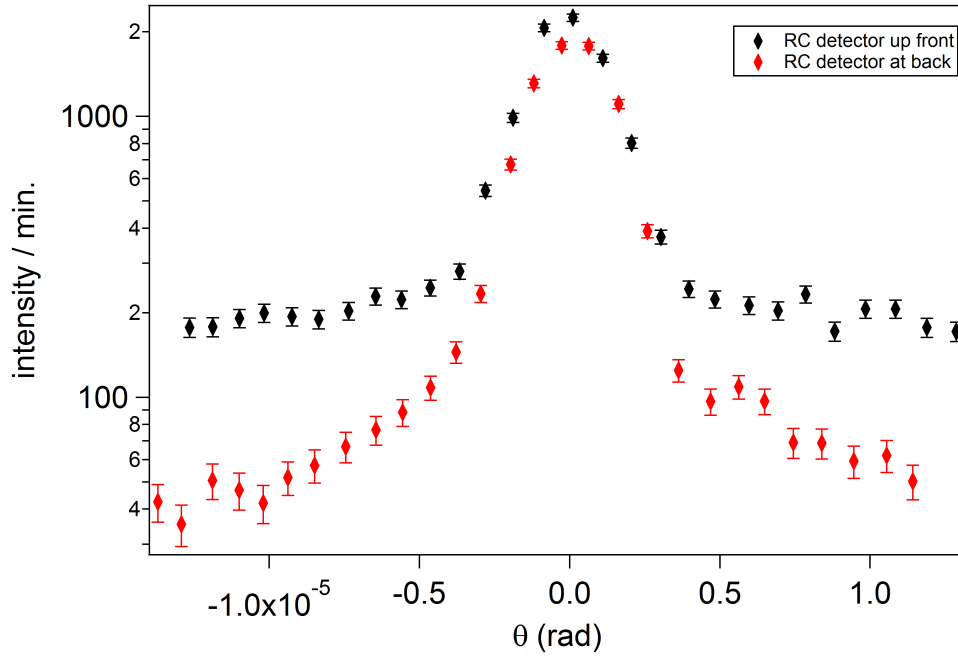


Figure 37: Measuring points at two different detector positions parallel to the neutron beam. The black ones were measured with the detector closer to the analyser and the red ones were measured with the detector at the old position.

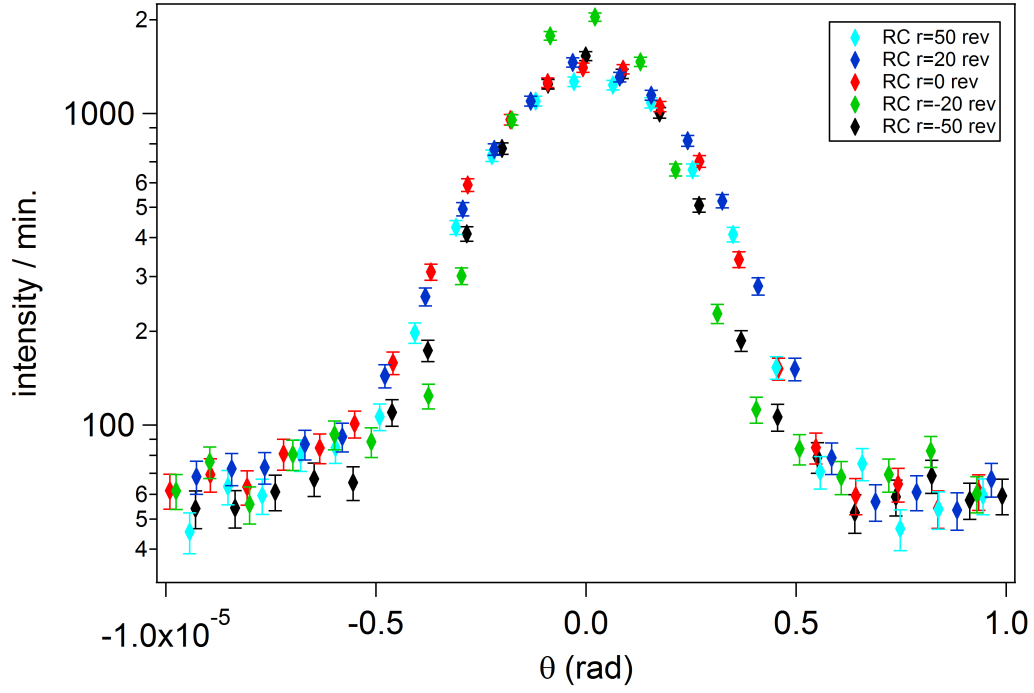


Figure 38: Measuring points at different rotating positions of the detector. For this the rear screw was adjusted.

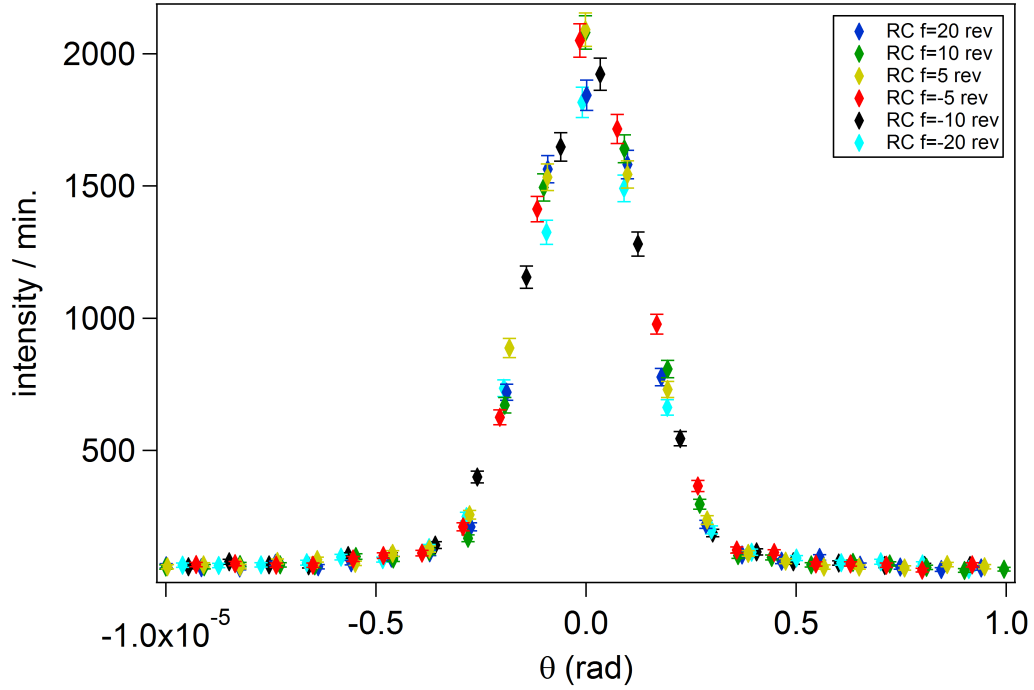


Figure 39: Measuring points at different rotating positions of the detector. For this the front screw was adjusted, the rear one was fixed at $r = -20$ rev.

5.3.2 Collimator mount

Since all the measurements reported in section 5.3.1 were done without a collimator, the background was significantly higher. This had the drawback that the program Igor had problems fitting the data accordingly. Therefore the best intensity was only estimated by comparing the measuring points instead of the fits. The position of the collimator had a high degree of freedom. It was placed rather freely on the frame with quite a bit of play. For sake of repeatable results four holes were drilled in the collimator mount, two on each side. In each of these a knurled-head screw was screwed in which holds the collimator in place. Now for changing the position of the collimator relatively to the detector barrel, the screws on one side were loosened after which the other screws were tightened again. Furthermore a line was drawn on each screw for counting the revolutions. This way it was possible to change the position of the collimator in a controlled way. As a reference point the collimator was placed as centred as possible and then the screws were screwed in at both sides. For the following measurements the collimator was first moved orthogonal to the neutron beam. The changes of the position are again given in revolutions with the step-size of one. The maximum revolutions were five for each screw. Although the use of the collimator is for decreasing the background which can be best seen by measurements over a large rotating angle, only the centre of the peak was measured. The reason for this was that the intensity should be maximised first and the faster each measurement took the more different collimator positions could be examined. In figure 40 the results of the different collimator positions are given. Since the intensity was still rather low and no real difference between the different positions were observable, the tilt angle of the analyser crystal was changed by 0.016° from $\rho = 1750$ counts to $\rho = 500$ counts. Then the collimator was rotated by just adjusting the screws in the front or the back. The intensity of the different positions can be seen in figure 41. As figure 40 and 41 indicate, there was no optimal collimator position found. The results of the different measurements are too similar to say with certainty that one position is better than the other.

5.3.3 Further improvement of the background intensity

For further improvement of the intensity to background ratio the barrel was moved closer to the analyser crystal while the detector inside the barrel was

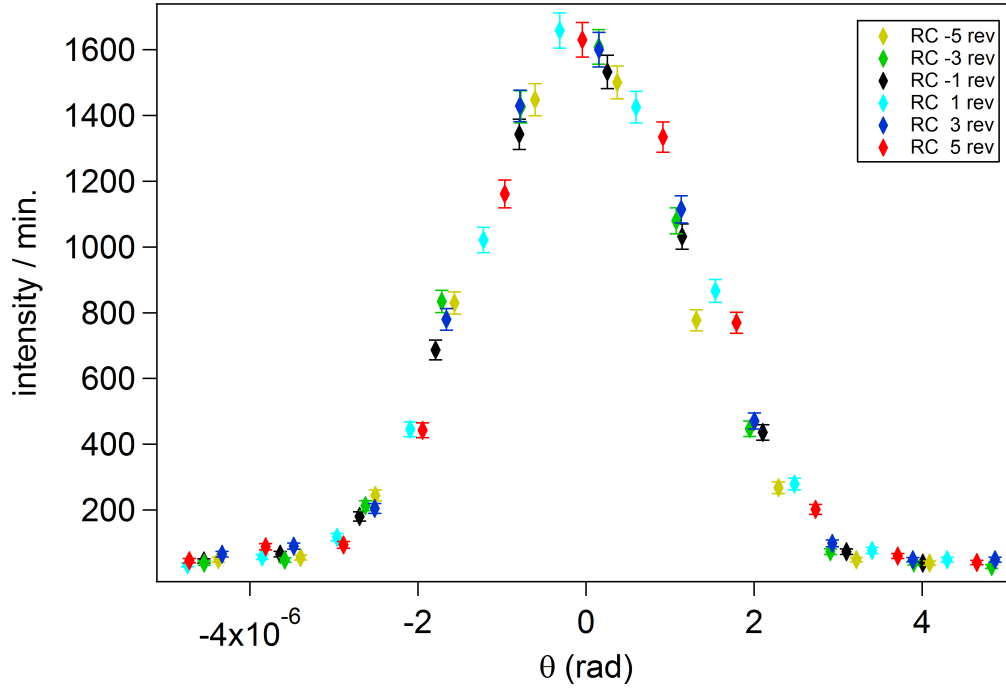


Figure 40: Measuring points taken at different collimator positions. All screws were adjusted by the same amount which lead to an orthogonal movement to the neutron beam. The unit of the movement is given in revolutions of the screws.

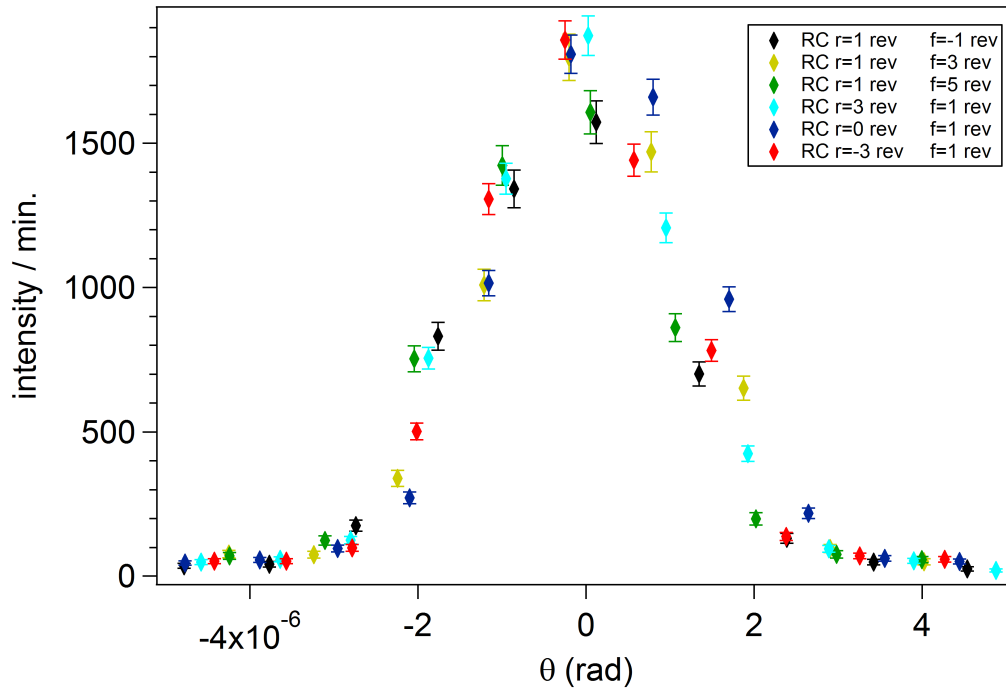


Figure 41: Measuring points taken at different rotation angles of the collimator. This time one screw was adjusted while the other one was fixed. Therefore the collimator rotated.

moved back to the end of the barrel. The overall distance between detector and analyser crystal stayed the same. The idea was that by moving the detector back the neutron beam was collimated more than by just going through the actual collimator. This might yield a lower background while the intensity should stay more or less the same, since the distance between detector and analyser crystal did not change. As the results in figure 42 show, the background intensity did indeed decrease while the peak intensity only changed slightly. The fitted results are also given in table 15. Although the ratio of peak intensity to background did increase, it was still lower compared to table 14.

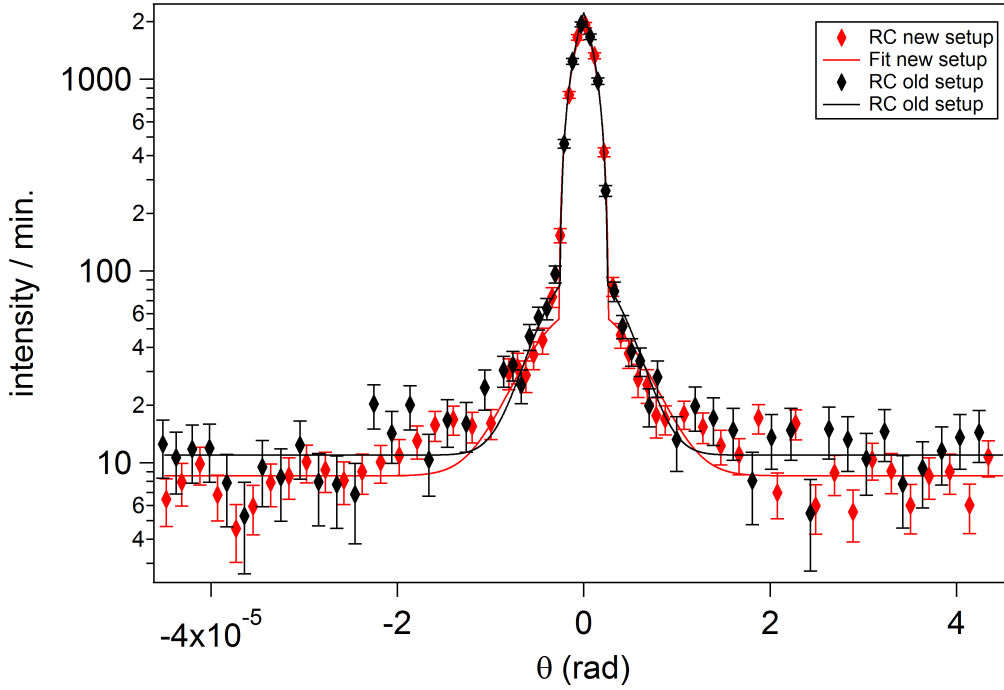


Figure 42: Rocking curve and fit of the new detector position in comparison to the old one. The barrel was moved closer to the analyser crystal while the detector was moved to the back of the barrel. This way the distance between analyser crystal and detector stayed the same but the background decreased.

5.3.4 Analyser adjustment

There is yet another degree of freedom for increasing the neutron intensity, namely changing the position of the analyser crystal. For the maximum neutron intensity the lattice planes of the analyser crystal has to be exactly parallel to

	Peak intensity [cts /min]	Background [cts /min]	Ratio of peak to background
Old setup	2213(43)	11.0(6)	201(15)
New setup	2096(40)	8.6(4)	244(16)

Table 15: Fitted results of the old and new detector position. The new detector position increased the background to peak ratio nicely.

the lattice planes of the monochromator crystal. This was already mentioned in chapter 3. Since the crystals were not adjusted for years there might be room for improvement. The monochromator itself is inside a tank behind a thick concrete wall which purpose is to shield against radiation. This means that the monochromator is not easy accessible. For this reason just the analyser was adjusted. Another reason why moving the analyser crystal could yield to better results was the repositioning of the detector. Due to that the relative position of the analyser and detector might have changed. Therefore, moving the analyser crystal sounds like a promising plan for increasing the measured neutron intensity. Therefore the analyser crystal was moved horizontally and vertically. For horizontal movement the linear translation stage M-403.4DG was responsible. For vertical movement M-403.2DG was used. The parameters for these were already given in table 4.

Now the analyser was moved 5 mm horizontally towards the reactor. The tilt angle seemed to have changed slightly. Therefore a peak search was done with different angles to find the one with the highest intensity. After that the analyser was moved 10 mm back, away from the reactor and another peak search followed. This was repeated two more times but with a step-size of 5 mm. The results can be seen in table 16. There not only the peak intensity is given but also the intensity of the two adjacent points to the peak centre. Because if two adjacent points have a very similar intensity the peak centre is between these two points with an even higher intensity. Normally this would have been considered by fitting the results of the peak measurements at one specific angle. But here quick measurements at many different tilt angles were done.

The change of the tilt angle between the first measurement and the others is probably due to problem with another LabVIEW program. It changed the tilt angle accidentally to its travel limit and although it was moved back again the

whole setup seemed to have been tilted slightly.

Analyser Y position [mm]	Analyser Z position [mm]	Tilt angle ρ [counts]	Peak intensity [cts /s]	Intensity of adjacent point [cts /s]	Intensity of adjacent point [cts /s]
+5	0	1500	28.6	14.3	17.6
-5	0	750	37.5	18.1	19.2
-10	0	750	30.9	15.1	14.6
-15	0	750	24.9	16.0	12.2

Table 16: Highest measured neutron intensity at different analyser positions and tilt angle ρ . The measurement time was 20 seconds for each point and 8 minutes for each measurement.

The highest peak intensity was at analyser position $Y = -5$ mm followed by position $Y = -10$ mm. Therefore the analyser was positioned between these two points at $Y = -7.5$ mm. Furthermore, the vertical z-axis was moved upwards to $Z = -2.5$ mm. After some measurements the z-axis was moved downwards to $Z = 7.5$ mm. As can be seen in table 17 the counts were reduced significantly in this position. Therefore the analyser crystal was moved upwards again. All the different analyser positions as well as the results of each measurement are given in table 17.

Analyser Y position [mm]	Analyser Z position [mm]	Tilt angle ρ [counts]	Peak intensity [cts /s]	Intensity of adjacent point [cts /s]	Intensity of adjacent point [cts /s]
-7.5	-2.5	500	34.2	26.3	14
-7.5	+7.5	500	26.4	23.2	9.5
-7.5	-10	500	35.6	20.5	17.3
-7.5	-15	500	30.8	16.0	15.8
-7.5	-7	1000	35.5	19.5	23.2
-7.5	-5	750	35.3	26.2	14.9

Table 17: Highest measured neutron intensity at different analyser positions and tilt angle ρ . The measurement time was 20 seconds for each point and 8 minutes for each measurement.

At the end of these measurements, the analyser crystal was moved to $Y = -7.5$ mm and $Z = -7$ mm. Although the position with $Y = -5$ mm and $Z = 0$ mm had a slightly higher measured intensity, the adjacent points showed very similar counts. On the contrary the intensity of the adjacent points of the

chosen position differentiated more. This indicates that the centre of the peak is somewhere in between. Though all things considered the difference between these two positions is very low and probably results from statistical errors. This also indicates that there is a small region at which the neutron intensity seems to be independent of the analyser position.

Now a measurement was done with a measuring time of 45 seconds per point to decrease the statistical error somewhat. The results are plotted in figure 43.

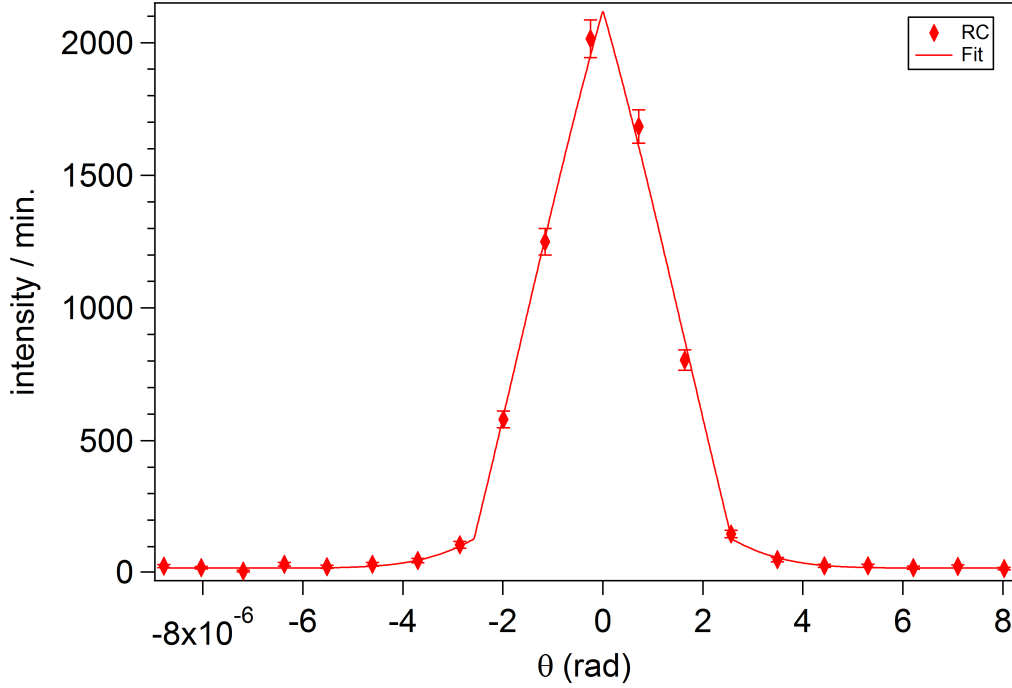


Figure 43: Rocking curve and fit at the new analyser position. The peak intensity is 2291(53) cts/min, FWHM= 2.628(3) μ rad, background intensity is 17.8(23) and the ratio of peak intensity to background is 129(20).

5.3.5 Loose connection

Some of the measurements of the last section had to be repeated because the detector still seemed to have a loose connection. Sometimes the analog ratemeter, which was already mentioned in section 4.2.2, did not measure any counts although the analyser crystal was positioned correctly and the LabVIEW program did receive a signal, though the counts were drastically reduced. The signal height was strikingly decreased and not high enough for the ratemeter.

As soon as the cable of the detector was positioned slightly different everything seemed to work again. Because of routine inspections of the power lines, which has to occur regularly at all institutes of TU Wien, the power had to be shut off at this stage of experiments. Since the reactor was also shut down for a few weeks it was a perfect opportunity to detach the detector cable and let it check by the electrical engineering workshop. It was diagnosed to be perfectly fine and was reinstalled at the detector. At first the detector showed a really noisy signal but after a few days the noise was gone. This was probably due to the fact that all the high voltage was shut off for some time during which humidity adversely affected the connection of the detector. Since then no problem with the detector had occurred and the ratemeter always received a signal.

5.4 A power cut and its consequences

As already mentioned due to a planned power cut the whole experiment had to be shut off. First of all the high voltage of the detector and monitor was turned off. Followed by everything else like motor controllers, piezo controller as well as the instrument PC. After a few days the power was back on again but the reactor was still shut down for maintenance. The DC motor responsible for tilting the analyser was disconnected to see if this would stop the accidental tilting. The voltage of the monitor was set back to 800 V and the detector was applied with 2.6 kV. The energy threshold was then set to $0.9 \text{ V} \leq \Delta E \leq 5.9 \text{ V}$.

It is important to mention that due to the power cut each reference point of the DC motor was reset. This means that although the values of all position counters were reset to zero the analyser crystal as well as the sample holder were still on the same physical position. In table 18 all of the old positions as well as the new reference points can be seen. The tilt angle of the analyser was the only non zero position. This occurrence may have the following explanation. Almost each time one of the LabVIEW programs were executed the counts of the tilt angle changed slightly. This had probably something to do with the disconnection of the motor since it only occurred with the disconnected motor. This issue will be further discussed in section 5.4.3.

Analyser:	Old position	New position	Sample holder:	Old position	New position
Horizontal axis Y	-7.5 mm	0 mm	Horizontal axis Y	-1 385 089 cts	0 cts
Vertical axis Z	-7 mm	0 mm	Vertical axis Z	750 000 cts	0 cts
Tilt angle ρ	1000 cts	438 cts	Tilt angle ρ	0 cts	0 cts

Table 18: The old position was set as the new reference point. However the physical position did not change.

5.4.1 Temperature sensors

As already mentioned in section 5.2.5 a temperature dependence of the measured rotation angle was observed. For further investigations two temperature sensors were bought to analyse a temperature difference between the analyser and monochromator crystal. Since the latter one is installed behind a thick concrete enclosure it was assumed that the temperature varies between these crystals.

The two sensors are PT100 temperature cable sensors of the series TS5289 by IFM. They are connected to a TP9237 evaluation unit with an analogue output signal between 0 V and 10 V. This signal goes to the NI PXI-6251 card installed in the NI PXI-1033 chassis and is monitored with the LabVIEW program "temperatureTest_pt100". For the voltage supply a NIM module with 24 V is used.

The two sensors were first placed side by side close to the experiment to test if everything worked. Their real purpose was to measure the temperature difference between the analyser crystal and the monochromator crystal. Therefore, one of these probes has to be placed near the monochromator crystal for which the concrete shielding blocks has to be moved with a crane. This took some preparation and was done in a later section 5.5. The temperature analysis can be seen in section 5.6.

5.4.2 Reactor back online

In total 39 days lay between the last measurement before the power cut and the first measurement after. During this time the peak position angle Θ seemed to have rotated by $2 \mu\text{m}$ piezo position corresponding to $30 \mu\text{rad}$ or 0.0017° . The fit of this rocking curve seemed to underestimate the peak intensity as can be seen in figure 44. Then the piezo actuator was positioned in the peak of

the rocking curve and a pulsed height spectrum of the detector was recorded to verify the settings of the neutron detection system. This can be seen in figure 45. The energy threshold $0.9 \text{ V} \leq \Delta E \leq 5.9 \text{ V}$ is coloured in cyan.

Over the next couple of days, several measurements were done at different spatial positions of the analyser crystal. This time the the same tilting angle ρ was used for each measurement since the DC-actuator responsible for tilting was still disconnected. Furthermore the piezo-actuator's range for each measurement was also increased. This was necessary to compare not only the peak intensity at each position but also the background intensity. Just like before the horizontal Y position was changed first, followed by the vertical Z position. In table 19 the analyser position as well as the fitted peak intensity, the full width at half maximum (FWHM) and the background intensity is given. Some of these measurements are also plotted in figure 46. It is important to note that some of the changes in the results, especially if the FWHM changes, may have come from an accidental tilting of the analyser crystal. Although the DC-actuator, which is responsible for tilting, was disconnected earlier, the horizontal and vertical movement of the analyser crystal could also have lead to an unwanted tilting. Unfortunately one has no influence on that. In the end the horizontal as well as the vertical position was set to zero $Y = Z = 0 \text{ mm}$ since it had the best results.

5.4.3 Tilt angle motor

To see if the neutron intensity could be increased by tilting the analyser, the motor was reconnected. As already mentioned the original position before the power cut was 1000 counts which was set as a new reference point to zero. Every time the LabVIEW program "Peaksuche_2017", which was used for the measurements, was executed the counts changed slightly. At the time of the reconnection the counts were already at 822, compare table 18. It is unknown if the DC motor changed its position to this value or if it stayed the same after reconnecting it. Nevertheless a peak search with different tilt angles was conducted. The different angles as well as the intensity of the peak and the adjacent points are given in table 20.

The highest intensity of these peak searches was at $\rho = -1750$ counts. But, since the measurement time for each point was only 20 seconds, several longer

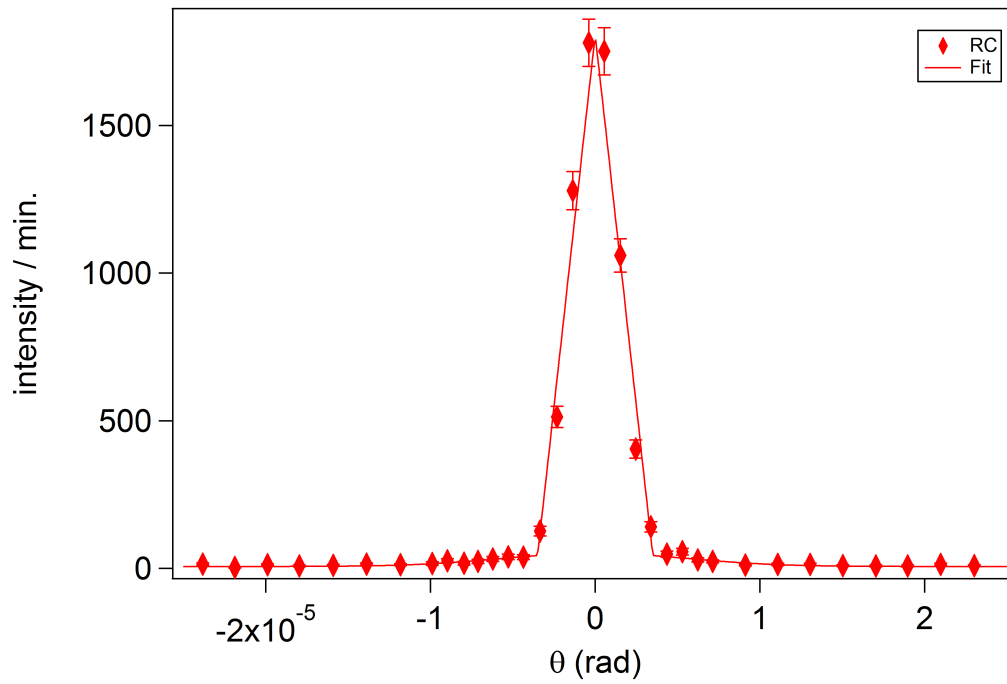


Figure 44: Rocking curve and fit of the first measurement after the reactor was back online.

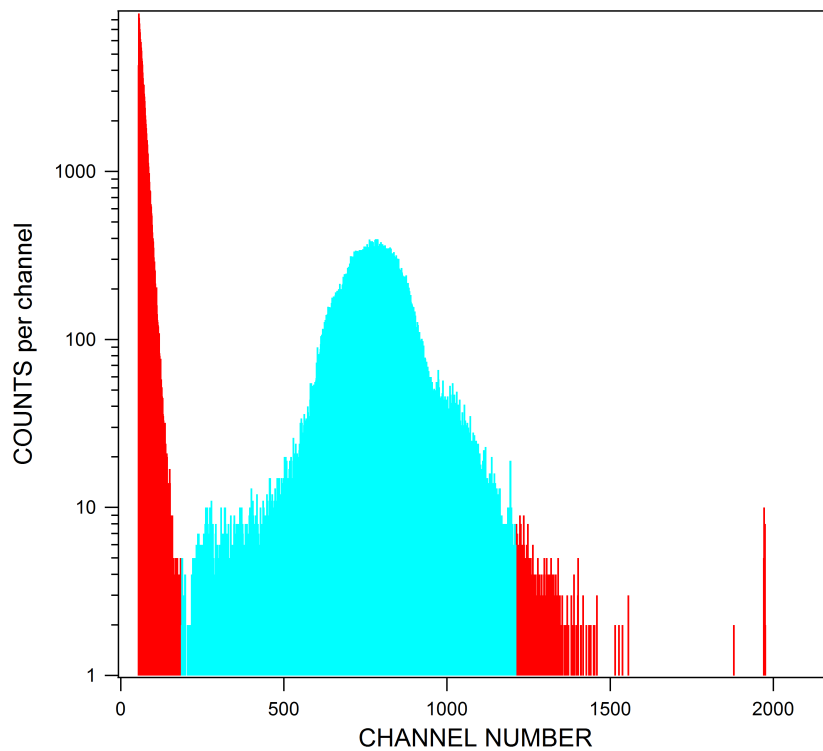


Figure 45: Pulse height spectra of the BF_3 detector. The events which were counted as neutrons are coloured in cyan.

Analyser Y position [mm]	Analyser Z position [mm]	Peak intensity [cts /min]	Background [cts /min]	FWHM [μ rad]
0	0	1562(30)	7.3(5)	3.939(32)
-5	0	1476(31)	7.9(5)	3.724(39)
-10	0	1305(28)	6.6(5)	3.579(30)
-15	0	1088(28)	7.7(5)	3.140(49)
5	0	1586(36)	10.5(6)	3.577(52)
10	0	1038(21)	5.7(6)	5.295(57)
15	0	854(19)	8.2(6)	5.277(74)
0	5	1332(27)	7.3(5)	4.625(53)
0	10	1305(29)	9.3(5)	4.521(70)
0	15	1126(24)	6.9(5)	4.608(52)
0	-5	1182(23)	7.1(6)	4.818(43)
0	-10	965(26)	10.2(6)	4.344(102)
0	-15	710(17)	7.4(6)	5.029(55)

Table 19: Peak intensity, background and FWHM at different analyser positions.

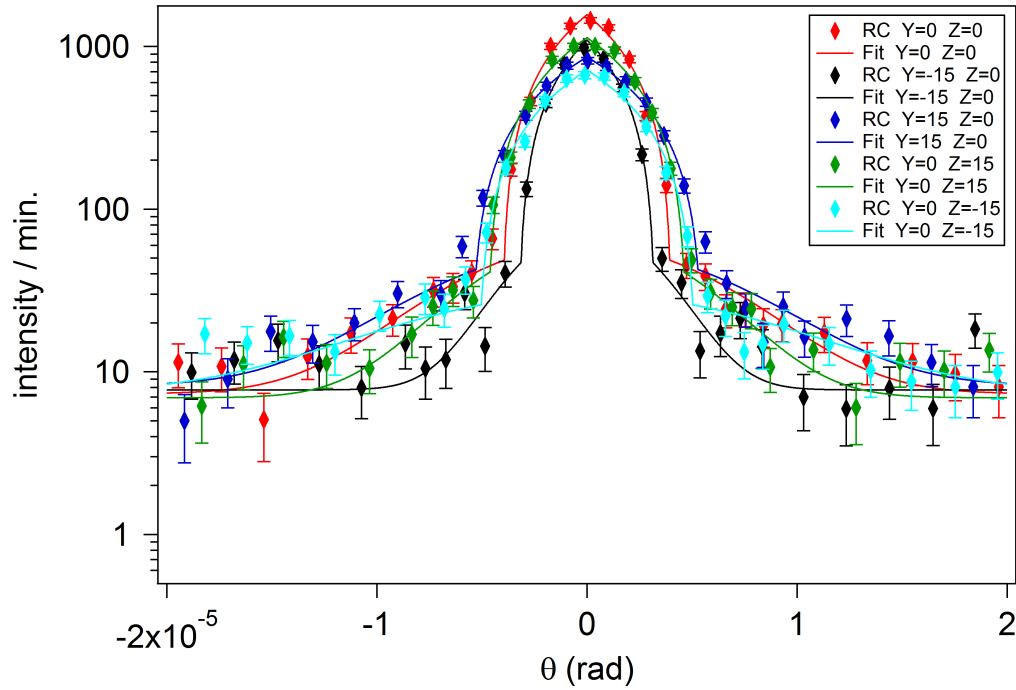


Figure 46: Rocking curves and fits at different analyser positions.

Tilt angle ρ [counts]	Peak intensity [cts/s]	Intensity of adjacent point [cts/s]	Intensity of adjacent point [cts/s]
-1000	25.5	24.3	13.4
-1250	30.6	23.4	14.0
-1500	35.1	21.1	20.3
-1750	36.2	23.7	14.1
-2000	32.5	24.3	12.8

Table 20: Intensity at the peak position and adjacent points at different tilt angles ρ . The measurement time was 20 seconds for each point.

measurements followed. This time only at three different tilt angles close to the position of the highest intensity from before, namely at $\rho = -1600$ cts, $\rho = -1750$ cts and $\rho = -1900$ cts an angular interval of $35 \mu\text{rad}$. The results can be seen in table 21 and figure 47 and they show that $\rho = -1750$ cts was still the best angle.

Tilt angle ρ [cts]	Peak intensity [cts /min]	Background [cts /min]	FWHM [μrad]
-1600	2218(41)	8.3(3)	2.685(24)
-1750	2440(45)	7.4(3)	2.575(14)
-1900	2230(43)	7.3(3)	2.674(23)

Table 21: Peak intensity, background and FWHM at different tilt angles.

5.4.4 Analyser adjustment II

After the peak measurements from before were done and evaluated, the analyser was moved once again, though this time only in a small area with a step size of 2.5 mm. Both the vertical Z-axis and the horizontal Y-axis were moved individually to position -2.5 mm, 0 mm and +2.5 mm. The peak intensity, background and FWHM can be seen in table 22. In figure 48 the fits of the rocking curves of selected analyser positions are given. In figure 49 a zoomed in version of the peak centre is also given. The tilt angle was still on $\rho = -1750$ counts for these measurements. The measurement parameters are given in table 23.

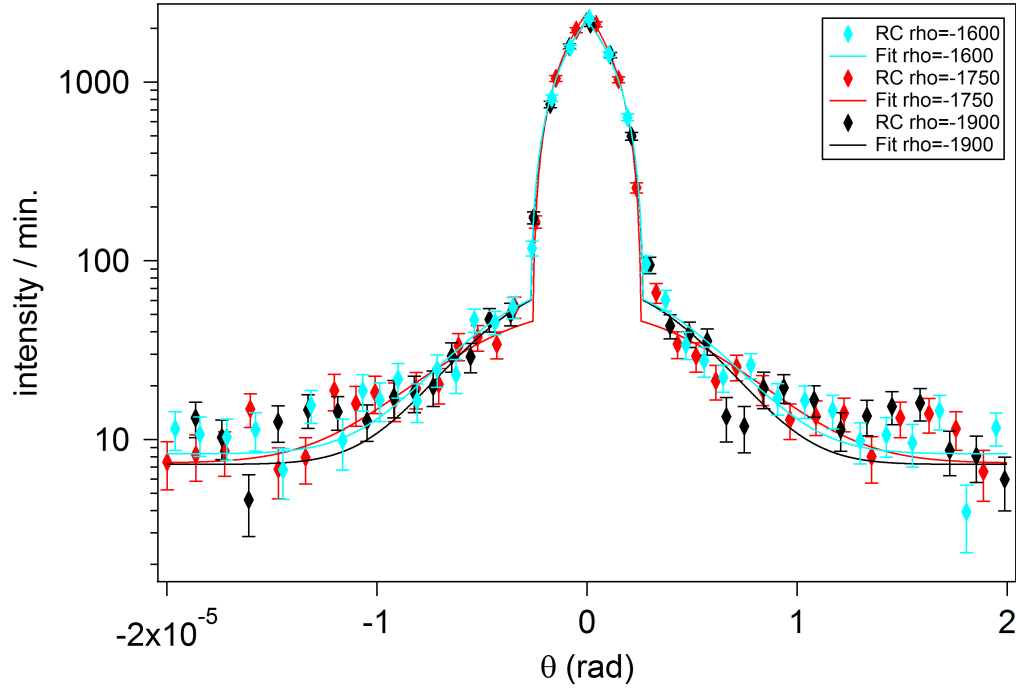


Figure 47: Rocking curve and fits at three different tilt angles ρ

Analyser Y position [mm]	Analyser Z position [mm]	Peak intensity [cts /min]	Background [cts /min]	FWHM [μ rad]
0	0	2355(53)	7.4(4)	2.640(26)
2.5	0	2225(44)	9.0(5)	2.855(16)
-2.5	0	2263(50)	8.1(4)	2.650(24)
0	2.5	2333(51)	7.5(4)	2.764(29)
0	-2.5	2385(52)	8.7(5)	2.648(23)
-2.5	2.5	2472(53)	8.0(4)	2.505(23)
-2.5	-2.5	2294(50)	8.4(4)	2.559(21)
2.5	2.5	2197(48)	8.8(4)	2.752(32)
2.5	-2.5	2192(48)	8.3(6)	2.697(24)

Table 22: Peak intensity, background and FWHM at different analyser positions.

It can clearly be seen that the best analyser position was at $Y = -2.5$ mm and $Z = 2.5$ mm. So for the next measurements the analyser was moved back to this position.

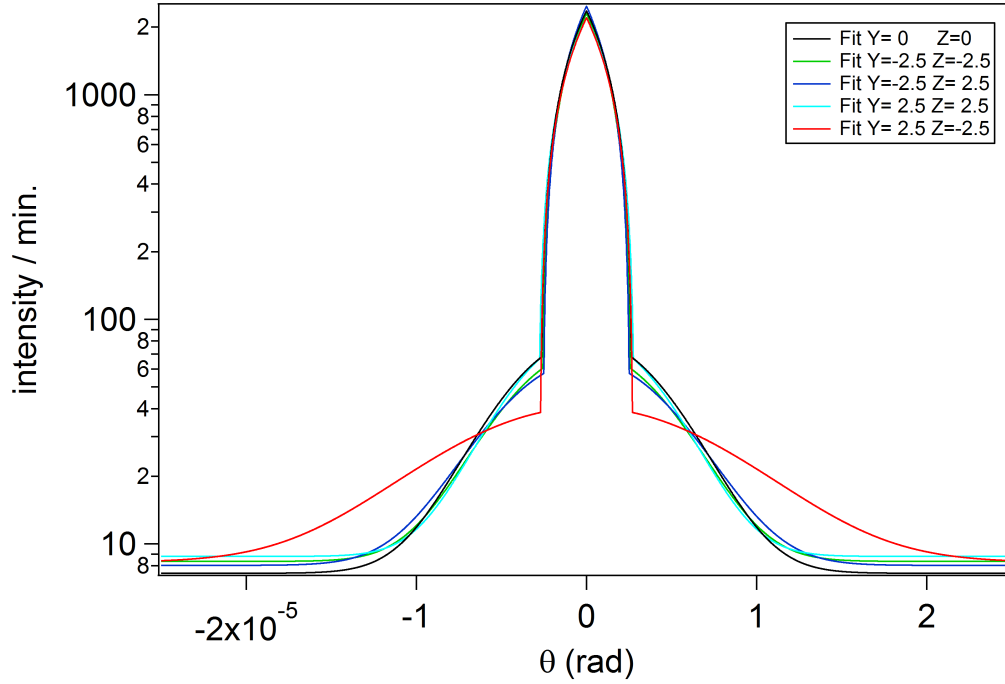


Figure 48: Fits of the rocking curves at different analyser positions. For better visibility the measuring points were removed.

5.4.5 Detector position II

The next step was moving the detector inside the barrel closer to the analyser crystal. This was already before but the results may have varied with the new analyser position. To begin with a long measurement was conducted for a good comparison. The parameters for this measurement is given in table 23.

	Old parameters		New parameters		
Piezo range [μm]	± 3.7	± 0.7	± 4.25	± 1.7	± 0.7
Step size [μm]	0.15	0.07	0.15	0.1	0.07
Measurement time per point [s]	90	45	120	90	60

Table 23: The old measurement parameters were used at the different analyser positions. The new parameters were used for different detector positions.

Then the detector was moved approximately 7 cm closer to the the analyser crystal. After another measurement was done it was moved forwards by another 7 cm. The results of these three measurements are given in table 24 and can

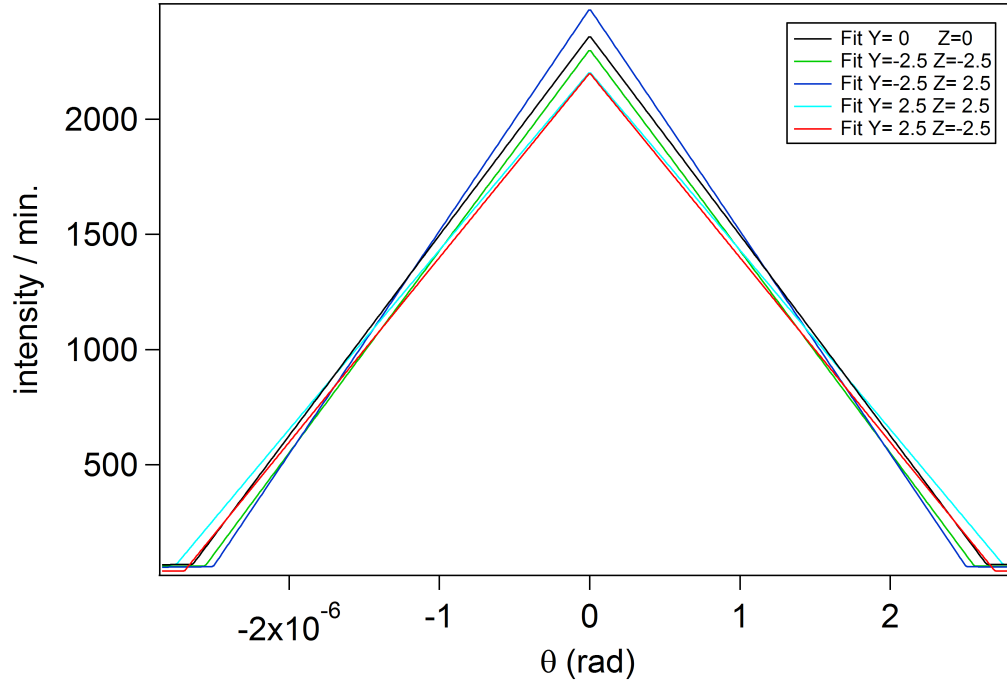


Figure 49: Fits of the rocking curves at different analyser positions. For better visibility the measuring points were removed. Here it was zoomed in at the peak centre.

also be seen in figure 50.

Detector position [cm]	Peak intensity [cts /min]	Background [cts /min]	FWHM [μ rad]	Ratio of peak to background
0	2349(47)	8.1(3)	2.432(28)	290(17)
7	2445(53)	9.3(5)	2.489(44)	263(20)
14	2455(53)	11.7(3)	2.505(42)	210(10)

Table 24: Peak intensity, background, FWHM and ratio of peak to background at different detector positions. The position is given as the distance between the back of the barrel and the back of the detector. The bigger the difference is the closer the detector is to the analyser crystal.

As expected the peak intensity did increase as well as the background. But the peak intensity increased only slightly which resulted in a better ratio of peak intensity to background the closer the detector was to the analyser crystal.

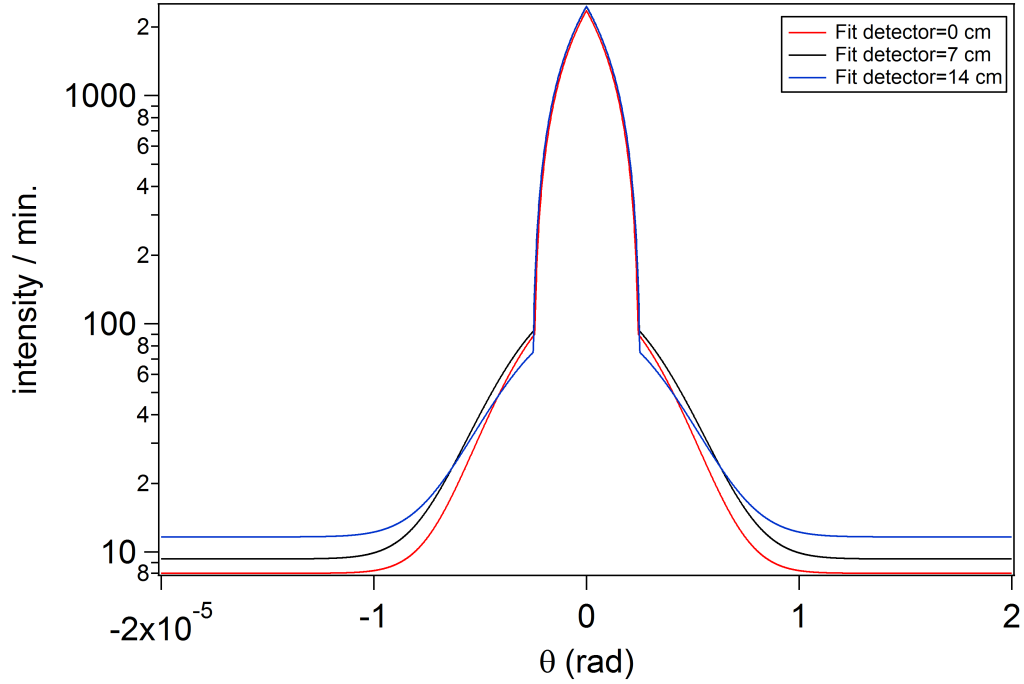


Figure 50: Fits of the rocking curves at different detector positions. The position is given as the distance between the back of the barrel and the back of the detector. The bigger the difference is the closer the detector is to the analyser crystal.

To increase this ratio the background intensity had to be reduced. This was already tried with the old setup by placing a screen in front of the collimator. This time a screen holder was newly manufactured and it was installed first without any screen. Furthermore the detector was moved at detector position 7 cm. After measurement was done a $40 \text{ mm} \times 40 \text{ mm}$ screen was placed in front of the collimator. The changes of the results with this screen should have been negligible since the neutron beam is smaller than $40 \text{ mm} \times 40 \text{ mm}$. But as can be seen in table 25 the intensity reduced quite drastically. The reason for this was probably bad positioning of the screen. Therefore the screen was positioned slightly different for each measurement until the intensity was about the same as with no screen. The results are also plotted in figure 51. For better visibility the measuring points were removed and only the fits were plotted.

Name	Screen	Peak intensity [cts /min]	Background [cts /min]	FWHM [μ rad]	Ratio of peak to background
RC01	no screen	2384(43)	8.7(3)	2.472(15)	274(14)
RC02	40x40	1908(37)	8.0(3)	2.549(18)	239(14)
RC03	40x40	2026(40)	8.4(3)	2.679(20)	241(13)
RC04	40x40	2193(50)	8.5(3)	2.419(42)	258(15)
RC05	40x40	2312(43)	8.5(3)	2.518(17)	272(15)

Table 25: Peak intensity, background, FWHM and ratio of peak to background with a 40x40 screen in front of the collimator. Each time the screen was positioned slightly different than before.

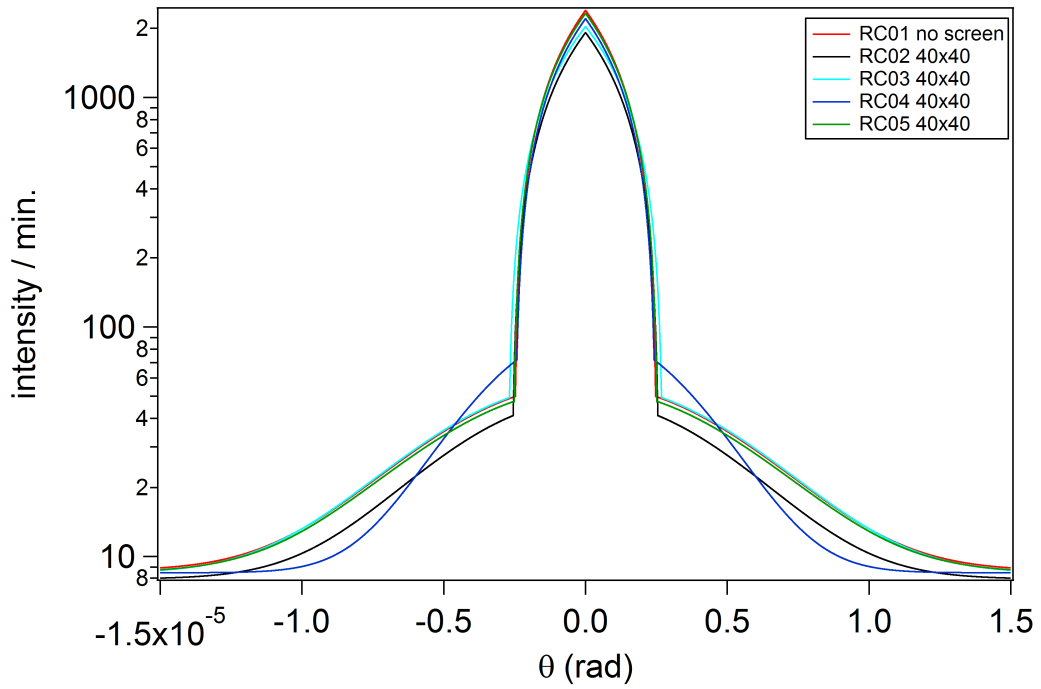


Figure 51: Fits of the different measurements with the 40x40 screen. For better visibility the measuring points were removed and only the fits were plotted.

5.4.6 Accidental tilting of the analyser crystal

With the last measurement the screen seemed to have been positioned correctly and the whole neutron beam went through. So the next step would have been using a different screen to reduce the background. But this was not done because of a problem with the LabVIEW program "Joystick", which was written by Markus Demel [35] a student who was doing his Project-thesis. It changed the tilt angle by accident to its limit. Although it was moved back to its original position the peak intensity changed, probably because the whole setup is very sensitive. Normally the angle is only changed in the range of μrad though the limit is in the range of several degrees. So the next step was to conduct several peak measurements. All with different tilt angles to find the one with the highest intensity. But a new problem occurred. The piezo actuator which is responsible for rotating the analyser crystal in each measurement can only expand itself in a range from 0 to 45 μm as already mentioned in section 4. The neutron peak position was almost at the upper limit of this range. This meant that only peak measurements with a rather small range could have been done. The solution was to rotate the analyser crystal with the additional DC-actuator. In section 4.2.4 more details about the movement of the analyser can be found. The DC-motor was disconnected the whole time since it was not needed.

But as soon as the DC motor was reconnected the neutron peak disappeared again. Several peak searches were done which covered the whole piezo actuator's range but the neutron beam was nowhere to be found. It is unclear if the DC motor moved as soon as it was reconnected or if the mechanical vibration resulting from the physical re-connection were the reason but the neutron peak seemed to be completely out of the piezo actuator's range.

With the LabVIEW program "dcmotor_piezo_iter" it is possible to set the current physical position of the analyser crystal to a different piezo actuator position. This is done with the help of the angle measuring device "RON 905" by Heidenhein. The piezo actuator is moved to its desired location. This movement is then countered by the DC motor which gets its information from the RON. Therefore the rotation angle stays the same but the piezo actuator is now at the new position.

First the piezo was moved from 40 μm to 30 μm . Then from 45 μm to 10 μm . Since still no neutron peak was found a different approach was necessary. The

analyser crystal was now continuously rotated by only the DC motor since it has a wider range than the piezo actuator. During that the intensity was measured every few seconds. The starting position of the motor was +12 533 counts and the peak was found at -18 200 counts an angular difference of 1.6 mrad. This angular range corresponds to 108 μm of piezo translation. This position was then set to 22.5 μm of the piezo actuator. A peak search where the analyser was moved via the piezo did indeed find the neutron peak at 22.8 μm .

5.5 Monochromator

Before any other measurements were done, the reactor was shut off due to maintenance. This was quite convenient since one of the temperature sensors should have been installed near the monochromator crystal. But for this the shielding around it had to be removed first. This can only be done if the reactor is shut off due to the corresponding radiation levels. Furthermore the concrete blocks on top of the tank in which the monochromator is installed had to be removed with a crane. In total, two heavy concrete blocks and the tank were removed to reveal the crystal. The first thing that was noticed is that a cadmium plate was on one side of the monochromator crystal similar to that of the analyser crystal. The difference was that the cadmium was not placed centred but only covered one half of the crystal. This was probably due to the fact that part of the neutron beam which goes through the crystal is used for the neighbouring neutron interferometer facility and if the complete crystal was covered with cadmium then no or too little of the neutron beam would go through. But the problem was not the half covered crystal but that the other half of the cadmium was inside the neutron beam leaving the monochromator towards the analyser crystal. This could have potentially decreased the measured neutron intensity of the USANS experiment. To prevent this the cadmium was cut in half and placed back behind the crystal. This time without covering the outgoing neutron beam. The next step was placing the temperature sensor near the monochromator crystal. The closer it is the better since the temperature difference between the analyser and monochromator is of interest. Therefore the other temperature sensor was placed closely to the analyser crystal. As soon as this was done the tank as well as the concrete blocks were moved back in place. Just a couple of days later the reactor was back online.

5.5.1 Intensity change because of cadmium reposition

A quick measurement was done over the whole piezo actuator's range followed by one at different tilt angles ρ . Interestingly the maximum neutron intensity was still at the same tilt angle $\rho = 600$ cts like before but the rotation angle θ changed by $7 \mu\text{m}$ piezo translation or $105 \mu\text{rad}$. However, this was not the only noticeable difference. During this measurement a big change of the intensity measured by the monitor was also observed. Since the installing of the monitor the detected neutron intensity was around 40 counts per second. After cutting the cadmium plate in half this intensity increased by over 50% between 60 and 70 counts per second. It was hoped that the neutron intensity measured by the detector had also increased greatly. Therefore, a long measurement was done to see if the intensity also improved for the BF_3 detector. The results of this can be seen in figure 52 and table 26. For better comparison the last rocking curve from section 5.4.5 is also given.

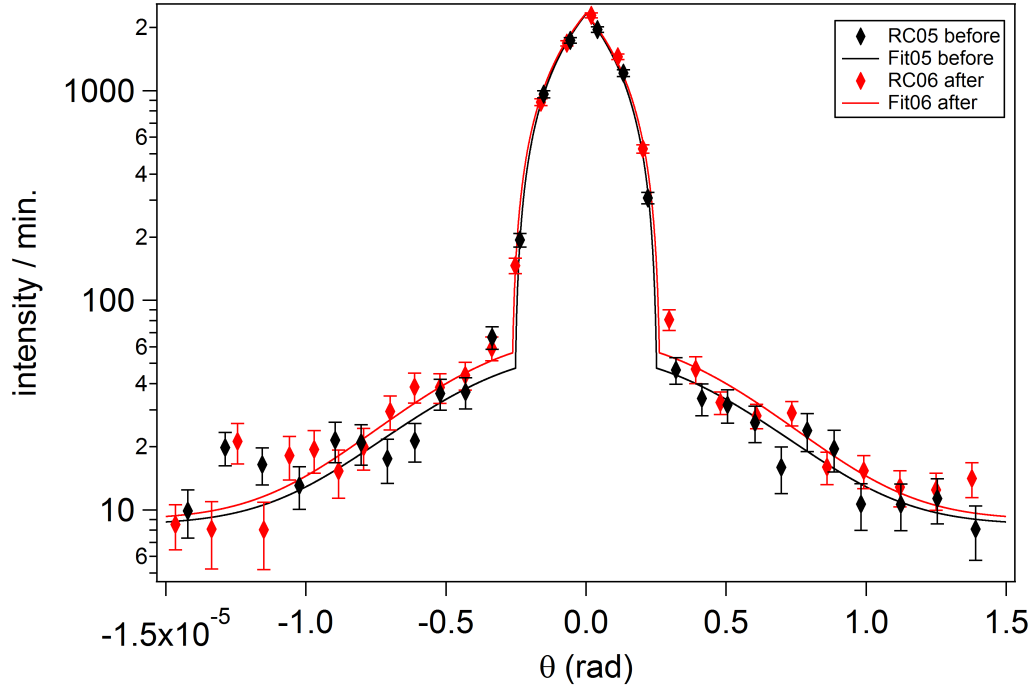


Figure 52: Rocking curves and fits from before and after the cadmium of the monochromator crystal was changed.

The results indicate that peak intensity did not change at all while the background intensity increased slightly. Further adjusting of the analyser crystal

Name	Tilt angle ρ [cts]	Peak intensity [cts /min]	Background [cts /min]	FWHM [μ rad]	Ratio of peak to background
RC05	-1750	2312(43)	8.5(3)	2.518(17)	272(15)
RC06	-600	2332(39)	9.0(2)	2.619(20)	259(10)

Table 26: Peak intensity, background, FWHM and ratio of peak to background for two measurements. Measurement RC05 was performed before the cadmium of the monochromator was cut in half, measurement RC06 after that.

position might have lead to better results. The analyser was therefore moved again and even some of the positions which were already done, were repeated.

5.5.2 Analyser adjustment III

The next couple of measurements were again conducted at different analyser positions. The first part of the results can be seen in table 27. All these measurements were done at $\rho = -600$ counts. We realised immediately that the intensity was quite a bit lower compared to table 26. This probably meant that the setup tilted especially since several days lay between these measurement. But since the relative intensity between the different analyser positions were of interest, these results were still of use.

Analyser Y position [mm]	Analyser Z position [mm]	Peak intensity [cts /min]	Background [cts /min]	FWHM [μ rad]
-2.5	2.5	1957(36)	9.0(5)	3.033(22)
-2.5	7.5	1988(38)	9.0(5)	3.005(25)
-7.5	7.5	1367(30)	8.4(5)	3.696(61)
2.5	7.5	1870(32)	10.0(6)	3.978(29)
7.5	7.5	1887(32)	9.3(6)	3.892(25)
7.5	2.5	2015(35)	11.7(7)	3.700(31)

Table 27: Peak intensity, background and FWHM at different analyser positions with $\rho = -600$ counts.

After these measurements were done the reactor was shut off again, this time for almost two weeks. Before the analyser position was changed again, a peak

search with different tilt angles was conducted. This indicated $\rho = 0$ counts as the best angle. Then a peak measurement was done at the same analyser position as before. Afterwards the analyser was moved again and the results can be seen in table 28.

The analyser positions in table 28 are in chronological order. It can be clearly seen that sometimes even a small change of the position yielded a big difference of the intensity. In order to be on the safe side that this does not arise from statistical fluctuations, one should repeat such measurements as often as possible. Unfortunately because of a tight schedule only some of these measurements were repeated with the same parameters. They are given in table 29.

Analyser Y position [mm]	Analyser Z position [mm]	Peak intensity [cts /min]	Background [cts /min]	FWHM [μ rad]
7.5	2.5	2536(49)	9.1(4)	2.834(31)
10	2.5	2299(41)	9.4(4)	3.051(21)
10	5	2485(49)	9.7(4)	2.869(32)
10	7.5	2564(49)	8.6(4)	2.743(26)
10	10	2454(47)	9.1(4)	2.848(28)
10	-2.5	2242(41)	10.0(5)	3.107(23)
10	-5	2291(46)	10.8(5)	2.887(34)
10	12.5	2314(46)	8.5(4)	2.761(33)
7.5	10	2633(56)	9.8(4)	2.586(42)
7.5	0	2769(61)	9.4(4)	2.581(46)
7.5	-5	2558(49)	10.6(5)	2.607(21)

Table 28: Peak intensity, background and FWHM at different analyser positions with $\rho = 0$ counts.

The results indicate that sometimes the intensity as well as other fitted parameters changed drastically although the same measurement parameters were used. It is unknown what exactly causes these discrepancies. But since the USANS setup is very sensitive even small vibrations from another experiment or people being in close proximity of this setup can already influence the results. To see if the setup tilted a peak search with different tilt angles was conducted at the last analyser position ($Y = 7.5$ mm $Z = -5$ mm). This measurement

indicated that the highest intensity was still at $\rho = 0$ counts. This means that the whole setup did not tilt any further or at least only slightly. Over the next three days three peak measurements with a very long measurement time per point were done to see if an increasing measurement time helps for the stability of the results. They can be seen in table 30. The measurement parameters are given in table 31.

As the results indicate, the increased measurement time only helped so much. It can clearly be seen that each of the fitted parameters differ by several standard deviations. Unfortunately it was no time to check more analyser positions since a laboratory course in neutron physics took place just a few weeks later. For this some preparations had to be done before.

Analyser Y position [mm]	Analyser Z position [mm]	Peak intensity [cts /min]	Background [cts /min]	FWHM [μ rad]
10	7.5	2564(49)	8.6(4)	2.743(26)
10	7.5	2668(51)	10.0(4)	2.710(29)
10	0	2534(49)	9.7(4)	2.908(34)
10	0	2575(50)	10.5(4)	2.774(32)
10	-5	2142(40)	10.0(4)	3.132(29)
10	-5	2291(46)	10.8(5)	2.887(34)
10	5	2485(49)	9.7(4)	2.869(32)
10	5	2294(41)	9.2(5)	3.100(21)
10	5	2623(50)	9.7(4)	2.730(29)
10	5	2605(49)	8.6(4)	2.731(27)
7.5	-5	2558(49)	10.6(5)	2.607(21)
7.5	-5	2273(40)	9.6(5)	3.029(17)

Table 29: Peak intensity, background and FWHM of measurements which were repeated with the same measurement parameters for sake of comparison.

5.5.3 Sample positioning

In the laboratory course several lattices were measured just like in section 5.2.7. But for this the sample holder had to be positioned centred in the neutron

Name	Peak intensity [cts /min]	Background [cts /min]	FWHM [μ rad]
RC01	2524(30)	10.8(2)	2.576(15)
RC02	2616(33)	11.5(2)	2.600(23)
RC03	2450(30)	10.5(2)	2.732(18)

Table 30: Peak intensity, background and FWHM of three long measurements with the same measurement parameters which are given in table 31.

Piezo range [μ m]	± 4.7	± 1.7	± 0.7
Step size [μ m]	0.15	0.1	0.07
Measurement time per point [s]	240	180	120

Table 31: Measurement parameters of the three peak measurements from table 30.

beam. Although this was already done before it had to be repeated since the analyser position was changed. First the mounting device without any screen was mounted and moved to several different positions until the intensity was about the same as without the device. The results as well as the positions can be seen in table 32.

Sample holder Y position [mm]	Sample holder Z position [mm]	Peak intensity [cts /min]	Background [cts /min]	FWHM [μ rad]
0	0	2428(48)	9.8(6)	2.770(27)
0	-10	2217(40)	9.5(6)	2.882(20)
5	-10	2457(48)	10.7(6)	2.620(25)
10	-10	2115(39)	11.5(7)	2.998(19)
10	-15	2325(46)	11.4(7)	2.691(27)

Table 32: Peak intensity, background and FWHM at different sample holder position with the mounting device installed.

After that the 40 mm \times 40 mm screen was attached and the sample holder was moved again. The step size for the vertical axis as well as the horizontal one was 5 mm. This resulted in a lot of different measurements. For better visibility only the peak intensity as well as the screen position is given in table 33.

Y [mm] Z [mm]	-20	-15	-10	-5	0
-15	1123(32)	1413(34)	1474(39)	1405(33)	
-10	1675(43)	1975(43)	2045(41)	2004(45)	
-5	2074(42)	2405(53)	2463(47)	2331(53)	2107(42)
0	2036(42)	2221(44)	2531(49)	2299(46)	1983(36)
5	1855(41)	2093(39)	2182(39)	1937(36)	1954(46)

Table 33: Peak intensity and error of the 40×40 screen at different position. In the first row the different horizontal positions (Y) and in the first column the different vertical positions (Z) are given.

The highest measured intensity was at position $Y = -10$ mm, $Z = 0$ mm but it is also important to consider the intensity of the adjacent points. In this case $Y = -5$ mm, $Z = 0$ mm and $Y = -15$ mm, $Z = 0$ mm. Although the difference of the horizontal position was only 5 mm the intensity was quite a bit lower. In comparison, the intensity of the adjacent points at $Z = -5$ mm were pretty similar. This probably meant that the result at $Y = -10$ mm, $Z = 0$ mm was just an outlier. Therefore the centre position of the sample holder was set at $Y = -10$ mm, $Z = -5$ mm since it had the second highest intensity and the adjacent points showed similar results.

5.5.4 Monitor defect

A week later it was noticed that the monitor showed between 0 and 8 counts per second, only. At first it was thought that the beam shutter of the beamline was closed but the BF_3 detector did register a peak. Even the intensity of the measured neutron beam was similar to the week before. This meant that only the monitor did not measure any neutrons. As soon as the cable between the monitor and the preamplifier was touched the signal increased drastically for a second. So it was thought that maybe the cable or the connectors were to blame. Therefore the high voltage of the monitor was turned off and the cables were disconnected and reconnected. Since this did not seem to resolve the problem a pulse height spectrum of the monitor was conducted. This is given in figure 53.

Compared to the original spectrum which is given in figure 15 there was no

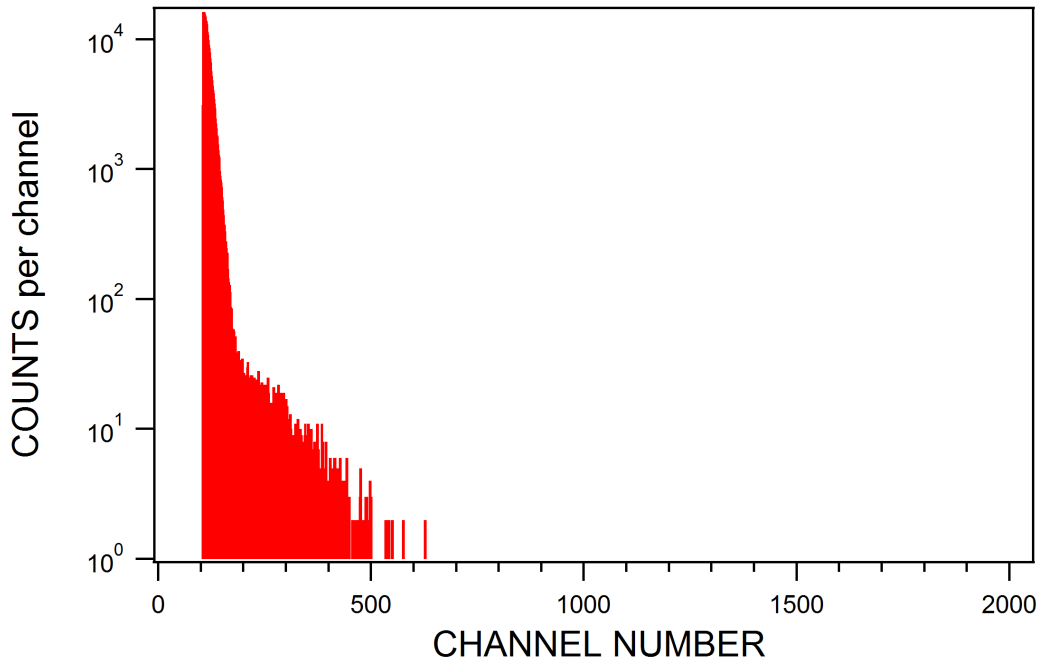


Figure 53: Pulse height spectra of the monitor. No usable signal was detected.

real signal but only noise. Replacing the cable between preamplifier and monitor did not work either so the preamplifier was swapped. But again there was no change of the signal. Before swapping the monitor it was hoped that maybe the problem would go away just like it came. The next day the problem still remained and therefore the monitor was replaced with an equivalent one. It was placed at the same position the old one was and once again a pulse height spectrum was measured which can be seen in figure 54.

It shows almost the same characteristics as in figure 15. One difference is that the first minimum of the old monitor is not visible at the new monitor due to the noise. But it should be kept in mind that the pulse height spectrum of the old monitor was done several months ago. This was before the cadmium of the monochromator was cut in half and the intensity of the monitor increased. Since then no pulse height spectrum was recorded and the old monitor would probably have showed the same signal as the new one. Also the noise is not that big of a problem since the threshold is set at 0.205 V which corresponds to channel 420 in the spectrum. This means that only events which deliver a larger signal than that (coloured in cyan) are counted as neutrons and the noise is very low energetic.

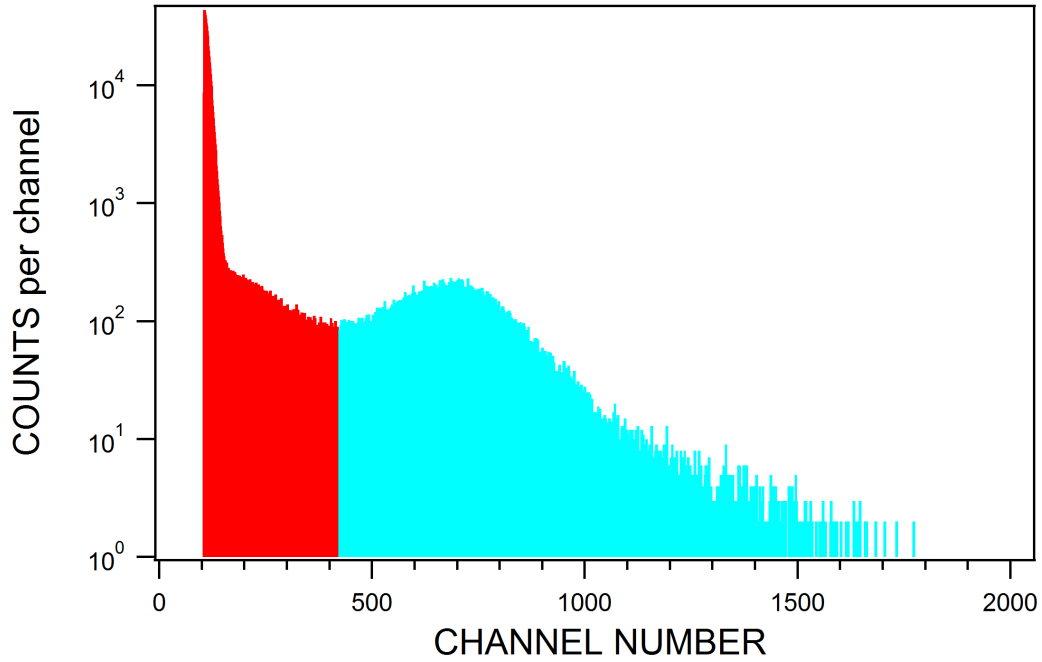


Figure 54: Pulse height spectra of the new monitor. The events which are counted as neutrons are coloured in cyan.

5.5.5 Lattice measurement II

Now that the monitor worked again several lattices were examined together with the participants of the laboratory course in neutron physics. On the one hand they lead to a nice observable diffraction pattern and on the other hand the angle measurement device RON could be tested. Since the lattice constants of the used samples were known the corresponding wavelength of the neutron beam can be calculated and compared to the one obtained in equation (85). All of this was already done in section 5.2.7 but this time more lattices were observed and quite a lot of changes were done with the whole USANS setup in the meantime. In total six different measurements were performed with three different lattices. Although two of those had the same lattice constant. The fitted results of each measurement can be seen in table 34. The ratio of the fitted wavelength of the lattice λ_l to the one calculated via the Bragg equation λ_B is also given. As can clearly be seen in table 34, the ratio of λ_l/λ_B is almost the same for each measurement. It differs slightly from lattice to lattice but the cause for this might be differences in the lattices and not because of the setup.

Name	Number of measurement	lattice constant [μm]	Wavelength λ_l [\AA]	Peak distance [μrad]	Ratio of λ_l/λ_B
Lattice I	1	28	1.607(7)	5.741(26)	0.913(4)
Lattice I	2	28	1.602(8)	5.721(28)	0.910(4)
Lattice II	3	20	1.585(5)	7.923(23)	0.900(3)
Lattice III	4	20	1.613(5)	8.064(24)	0.916(3)
Lattice III	5	20	1.576(5)	7.882(23)	0.896(3)
Lattice III	6	20	1.566(5)	7.831(23)	0.890(3)

Table 34: Fitted results of the different lattices.

The only bigger discrepancy was the fourth measurement of lattice III. But this can be explained with a change of the rotation angle of the sample holder. For the first four measurements the neutron beam was not perfectly orthogonal to the lattices, which resulted in different peak height of the first order maxima as can be seen in figure 55. This was already the case in section 5.2.7 but since then the setup changed a lot. Therefore it was rotated again before the fifth measurement was done. Now the first order maxima were about the same height as can be seen in figure 56.

Under the assumption that the discrepancies of the angles measured by RON are linear and indeed resulted in the lower fitted wavelength, dividing the measured angle with the mean value of λ_l/λ_B should yield the correct one. The mean value is as followed

$$\langle \lambda_l/\lambda_B \rangle = 0.904 \pm 0.003. \quad (87)$$

As already mentioned in the sections before, the FWHM was sometimes lower than the calculated one of equation (78). Dividing these by the value obtained in (87) should increase them to yield a more reasonable result. For testing purpose some of the old FWHM values, especially these which were lower than the theoretical minimum of $2.685 \mu\text{rad}$, were modified and are given in table 35.

Fortunately almost all of the modified FWHM were larger than the theoretical minimum and the one which was still lower was within the margin of error. This indicates that the discrepancies came indeed from a wrongly measured angle which can be compensated with the help of equation (87).

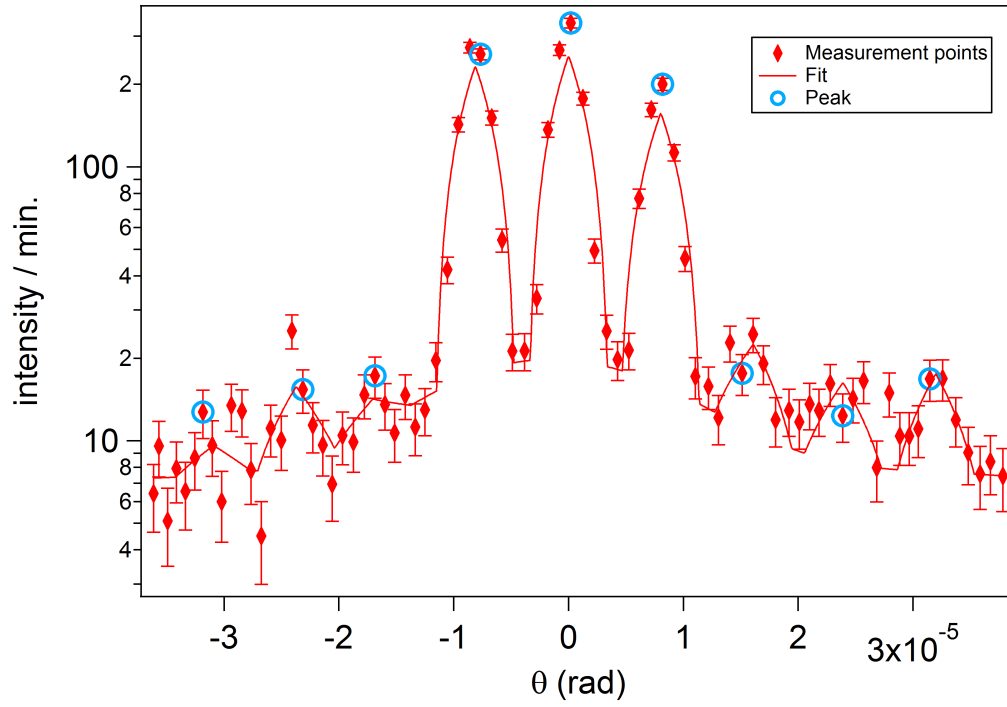


Figure 55: Measurement points, fit and peak location of lattice III. The neutron beam was not orthogonal to the lattice.

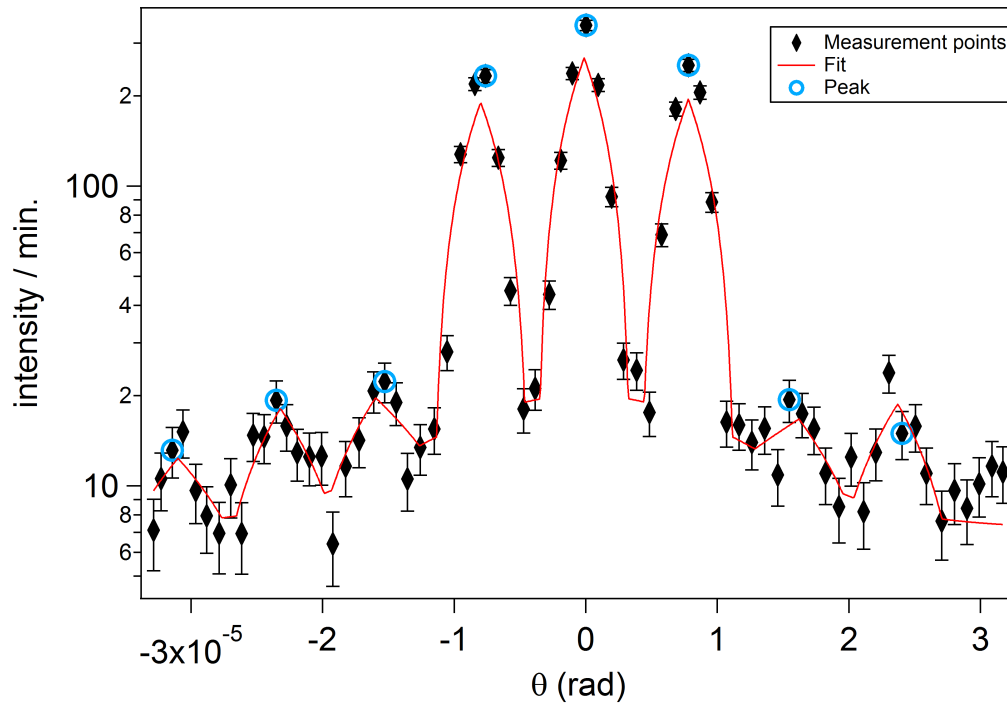


Figure 56: Measurement points, fit and peak location of lattice III. The neutron beam was orthogonal to the lattice.

Source of table	Old FWHM [μrad]	Modified FWHM [μrad]
11	2.612(47)	2.888(62)
11	2.692(32)	2.978(46)
24	2.432(28)	2.689(41)
24	2.489(44)	2.752(58)
24	2.505(42)	2.770(56)
25	2.472(15)	2.734(26)
25	2.549(18)	2.819(30)
25	2.679(20)	2.963(33)
25	2.419(42)	2.675(56)
25	2.518(17)	2.784(29)

Table 35: Old and modified FWHM of different measurements as well as the table from which the results were taken.

5.6 Temperature analysis

In this last section the temperature difference of the analyser and monochromator crystals was analysed. As already mentioned before, the peak positions of the neutron beam changes ever so slightly after most measurements. Sometimes even bigger difference were observed if the break between the measurements were several days. To see if this resulted from a temperature difference, two PT100 thermocouples were installed as described in section 5.4.1. Furthermore the angle measurement which was already done in section 5.2.5 was repeated. In figure 57 the measured angle as well as the temperature difference between analyser and monochromator crystal are plotted as a function of Δt .

The results clearly show a temperature dependence of the RON position similar to figure 18 and figure 19. The difference this time is that not the room temperature was plotted but the temperature difference between the analyser crystal and monochromator crystal. Though since the monochromator crystal is behind thick concrete blocks its temperature varies only little. Therefore plotting the RON position over just the analyser temperature yields even better results as can be seen in figure 58.

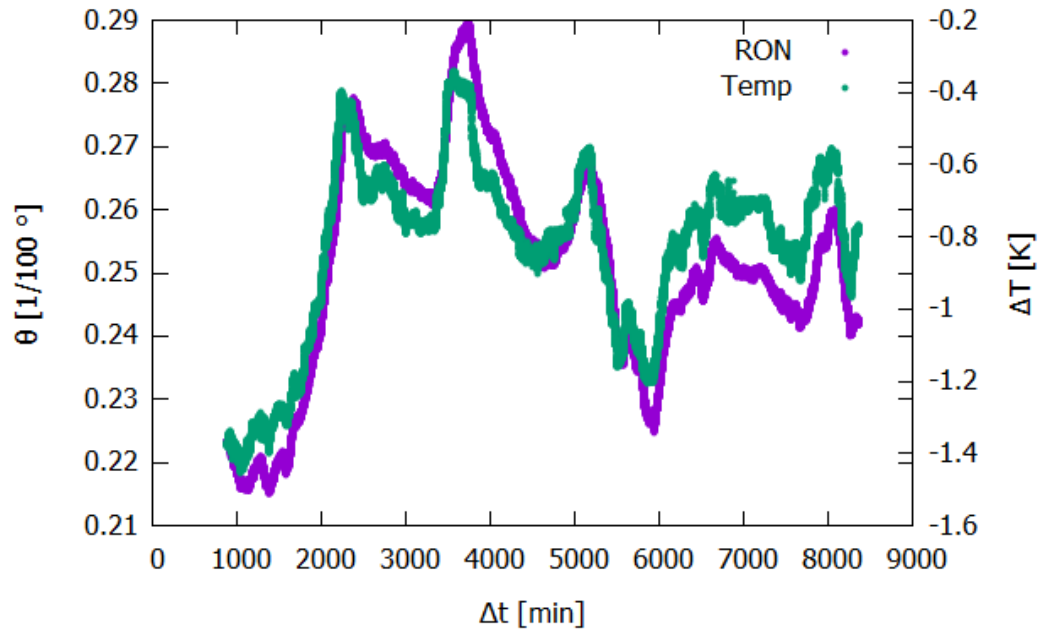


Figure 57: In this figure the temperature difference of the analyser and monochromator crystal together with the RON position are plotted over time.

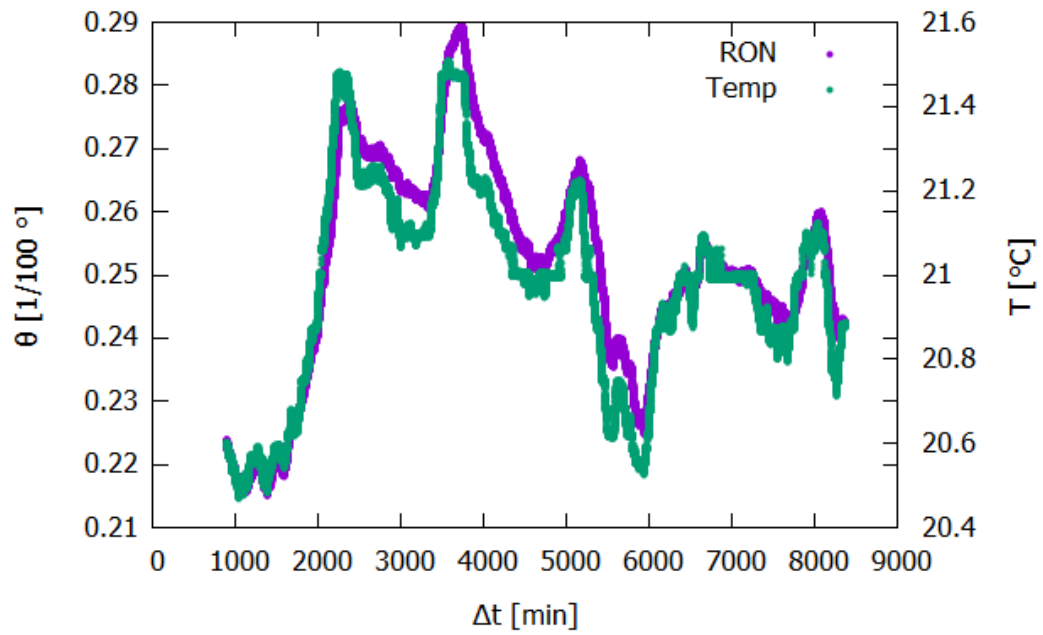


Figure 58: Here the temperature of the analyser crystal together with the RON position are plotted over time.

This probably means that the changing of the peak position did not result from a temperature difference between the analyser and monochromator crystal but on the temperature fluctuations of the analyser crystal. Being more precise the mechanical rotation system at which the analyser is positioned, probably rotates slightly with the changing temperature. This is more than plausible since the fluctuations of the angle is in the order of μrad .

6 Conclusion

In conclusion it can be said that a lot of different improvements as well as modifications to the USANS facility were done during this master's thesis. First the PC was migrated to a newer model with a more recent operating system and better hardware.

A neutron monitor, which is very crucial for this type of experiment, was installed and calibrated. Therefore, fluctuations of the neutron intensity can be compensated. Which also means that if the reactor has to decrease its power output, for whatever reason, the measurement does not have to be repeated. This is especially important if each measurement takes several hours.

A rocking curve at different tilt angles was also conducted. Subsequently, the dependence between the intensity and the tilt angle can be seen which can be used to compensate an accidental tilting.

Furthermore, the neutron beam itself was characterised. The area of the beam was approximated to be 9 cm^2 . Additionally the measurements with different screens indicated that the neutron beam is inhomogeneous and more dense in the centre of the beam.

The stability of the USANS instrument was also examined. In conclusion it can be said that a change of the setup, like installing new hardware on the optical bench, will most likely result in tilting of the analyser crystal. However, accidental tilting without performing any change of the setup is uncommon and results only in a small change of ρ . This was also proven by the last two measurements. The intensity as well as the FWHM stayed about the same although one was done mid December 2018 and the other one mid January 2019. This indicates that the USANS instrument is reliable and a small change of ρ can be compensated by conducting a measurement at different tilt angle at the first day of each week or month.

Another big modification was done with the mounting for the detector collimator. It was attached to the paraffin wax barrel. This way if the barrel is moved the collimator moves along and is not separated anymore. This is especially useful for further improvements of the detector position in the future.

An intensity increase was achieved by changing the analyser crystal position. This way the analyser is now better aligned with the monochromator and the detector.

A loose connection of the BF_3 detector which randomly resulted in a wrong reading of the neutron counts, was fixed.

The shielding of the monochromator crystal was opened the first time for years and a temperature sensor was placed inside it. Furthermore a cadmium plate which blocked part of the neutron beam was cut in half. Discrepancies of the angle measurement device were observed and investigated. This was done by analysing several different lattices and their measured lattice constant. They indicated that the measured angle was by a factor of 0.904 ± 0.003 smaller than expected.

A lot of enhancements and corrections were done, however, there is still room for improvements. The analyser crystal position can still be investigated further and the same is true for the detector position. Although the background intensity did decrease it is still not ideal and further improvements are possible.

7 References

- [1] U. Bonse and M. Hart. Tailless X-ray single-crystal reflection curves obtained by multiple reflection. *Appl. Phys. Lett.* **7** (1965) 238–240.
- [2] E. Jericha, G. Badurek, and R. Grössinger. Characterisation of novel magnetic materials using the USANSPOL technique *Physics B* **406** (2011) 2401–2404.
- [3] E. Jericha, G. Badurek, C. Gösselsberger, and D. Süss. Experimental and methodic progress in ultra-small-angle polarised neutron scattering on novel magnetic materials. *J. Phys.: Conf. Ser.* **340** (2012) 012007.
- [4] E. Rutherford. Bakerian Lecture: Nuclear constitution of atoms. *Proc Roy. Soc. A* **97** (1920) 374–400.
- [5] J. Chadwick. The existence of a neutron. *Proc. Roy. Soc A* **136** (1932) 692–708.
- [6] W. G. Williams. Polarized neutrons. Oxford series on neutron scattering in condensed matter. Oxford University Press, Oxford, 1988.
- [7] CODATA Recommended Values of the Fundamental Physical Constants. <http://dlmf.nist.gov/>, Release 1.0.20 of 2018-09-15. F. W. J. Olver, A. B. Olde Daalhuis, D. W. Lozier, B. I. Schneider, R. F. Boisvert, C. W. Clark, B. R. Miller and B. V. Saunders, eds.
- [8] A. I. Frank. Fundamental properties of the neutron: Fifty years of research. *Soviet Physics Uspekhi* **25** (1982) 280.
- [9] M. Tanabashi, et al. Review of particle physics. *Phys. Rev. D* **98** (2018) 030001.
- [10] D. Griffiths. *Introduction to Elementary Particles*. Wiley VCH, Weinheim, 2008.
- [11] G. F. Knoll. *Radiation detection and measurement*. Wiley, New York, 3. edition, 2000.
- [12] M. Villa. *Optimiertes Kristalldesign für ein Doppelkristall-Diffraktometer*. Doctoral Thesis, TU Wien, 2001.

- [13] O. Glatter and O. Kratky. Small-angle X-ray scattering. Academic Press, London, 1982.
- [14] L. A. Feigin and D. I. Svergun. Structure analysis by small-angle X-ray and neutron scattering. Plenum Press, New York, 1987.
- [15] V. F. Sears. Neutron optics. Oxford series on neutron scattering in condensed matter. Oxford University Press, Oxford & New York, 1989.
- [16] R.J. Weiss. Small-angle scattering of neutrons. Phys. Rev. **83** (1951) 379–389.
- [17] B. A. Lippmann and J. Schwinger. Variational principles for scattering processes. Phys. Rev. **79** (1950) 469–480.
- [18] M. Born. Quantenmechanik der Stoßvorgänge. Z. Phys. **38** (1926) 803–827.
- [19] E. Fermi. Sul moto dei neutroni nelle sostanze idrogenate. Ric. Sci. **7** (1936) 13–52.
- [20] M. Hainbuchner. Ultra-Kleinwinkelstreuung von Neutronen an strukturierten Materialien. Doctoral Thesis, TU Wien, 2000.
- [21] L. Rayleigh. On the diffraction of light by spheres of small relative index. Proc. Roy. Soc. A **90** (1914) 219–225.
- [22] O. Kratky and G. Porod. Diffuse small-angle scattering of X-rays in colloid systems. J. Colloid Sci. **4** (1949) 35–70.
- [23] A. Guinier and G. Fournet. Small-angle scattering of X-rays. Structure of matter series. Wiley, New York, 1955.
- [24] G. E. Bacon. Neutron diffraction. Monographs on the physics and chemistry of materials. Clarendon Press, Oxford, 3. edition, 1975.
- [25] A. Guinier. Théorie et technique de la radiocristallographie. Series of books in physics. W.H. Freeman, 1963.
- [26] G. Porod. Die Röntgenkleinwinkelstreuung von dichtgepackten kolloiden Systemen. Kolloid-Zeitschrift, **124** (1951) 83–114.

- [27] H. Rauch and D. Petrascheck. Dynamical neutron diffraction and its application. In *Neutron Diffraction*, volume **6** of *Topics in current physics*, H. Dachs ed., pp. 303–351. Springer, 1978.
- [28] W. H. Bragg and W. L. Bragg. The reflection of X-rays by crystals. *Proc. Roy Soc. A* **88** (1913) 428–438.
- [29] H. Rauch and W. Waschkowski. *Neutron Scattering Lengths*. Landolt-Boernstein, Vol. I/16A, H. Schopper ed., Chapter 6, Springer, Berlin, 2000.
- [30] J. W. M. DuMond. Theory of the use of more than two successive X-ray crystal reflections to obtain increased resolving power. *Phys. Rev.* **52** (1937) 872–883.
- [31] Atominstitut der TU Wien. ati.tuwien.ac.at/reactor. Accessed on: 2018-09-01.
- [32] E. Jericha. private communication, 2019.
- [33] M. Agamalian, G. D. Wignall, and R. Triolo. Optimization of a Bonse–Hart Ultra-Small-Angle Neutron Scattering Facility by Elimination of the Rocking-Curve Wings. *J. App. Cryst.* **30** (1997) 345–352.
- [34] T. Reichel. Inbetriebnahme und Kalibrierung der neuen "Bonse-Hart-Kamera" für Neutronen-Ultrakleinwinkelstreuung am TRIGA Reaktor des Atom Instituts. Diploma Thesis, TU Wien, 2011.
- [35] D. Markus. Verbesserung der Handhabbarkeit und Erstellen einer Steuerung am USANS-Experiment. Project Thesis, TU Wien, 2019.
- [36] Kirsten Lux. Diffraktion thermischer Neutronen an periodischen Phasengittern aus Silizium-Einkristall. Diploma Thesis, TU Wien, 2008.
- [37] M. Trinker, E. Jericha, W. Bouwman, R. Loidl, and H. Rauch. Analysis of artificial silicon microstructures by ultra-small-angle and spin-echo small-angle neutron scattering. *Nucl. Instrum. Methods A* **579** (2007) 1081–1089.
- [38] D. Seppi and A. Wastl. Experimentelle Hadronenphysik. Project Thesis, TU Wien, 2010.